Upscaling from Atomistic Models
to Higher Order Gradient Continuum Models
for Crystalline Solids

Dissertation

zur

Erlangung des Doktorgrades (Dr. rer. nat.)

der

Mathematisch-Naturwissenschaftlichen Fakultät

der

Rheinischen Friedrich-Wilhelms-Universität Bonn

vorgelegt von

Marcel Arndt

aus

Münster

Bonn 2004

Angefertigt mit Genehmigung der Mathematisch-Naturwissenschaftlichen Fakultät
der Rheinischen Friedrich-Wilhelms-Universität Bonn

Contents

Chapter 1

Introduction

In our technologically highly sophisticated society, it is crucial to understand the processes in nature up to the furthest possible extent, since these insights form the basis for all kinds of technological developments. Beyond the two classical ways of investigating nature, namely by experiments and by theoretical considerations, a third way has emerged within the last few decades. The rapid development of computers now allows to tackle this challenge by means of numerical simulation. The goal of scientific computing and numerical simulation is to describe a certain part of nature in terms of a mathematical model and to solve this model using computers.

Compared to the classical methods, this approach offers the advantage to numerically perform experiments which cannot be carried out in reality because they are too large, too small, too hazardous, too costly, proceed too rapidly or too slowly, because the results cannot be measured or due to other restrictions. Numerical simulation can often provide a flexible and economical alternative. For example the properties of new materials can be predicted this way even before they are fabricated, which reduces time and costs for development.

The range of processes and properties in nature to be investigated is very broad. We mention a few areas here:

Process or property	Length scale
Chemical bonding and other quantum mechanical interactions of nuclear particles	$10^{-12}\text{m} - 10^{-9}\text{m}$
Structural phase transformations, formation of microstructure, atomic dislocations in crystals and other atomic interactions	$10^{-9}\text{m} - 10^{-6}\text{m}$
Elasticity and plasticity of solids	$10^{-6}\text{m} - 10^{-3}\text{m}$
Mechanical material properties	$10^{-3}\text{m} - 10^{0}\text{m}$
Statics and other structural properties of buildings	$10^{0}\text{m} - 10^{3}\text{m}$
Weather development in the atmosphere	$10^{3}\text{m} - 10^{7}\text{m}$
Formation of galaxies in astrophysics	$10^{18}\text{m} - 10^{21}\text{m}$

One can clearly realize that not only the processes are manifold, but also that the

involved length scales vary considerably. For all these processes on their particular length scale, a large variety of different models has been developed. The class of molecular dynamics methods for example has proven successful to model the interaction of atoms, and continuum mechanical models are widely used to describe effects on larger length scales like elasticity of solids or fluid dynamics.

Classically, these models are set up by observing the effects in nature and then defining the model such that it fits well with these observations. This approach is called *phenomenological*. Because such kind of modeling can only be accomplished for a limited number of effects on a single length scale, a set of independent models is obtained on each level this way.

However, the effects on the respective length scales are not independent of each other. In fact, the interaction of atoms can in principle be described by the interaction of a much larger number of nuclear particles of which each atom consists. Similarly, elasticity effects can be described by a large system of atoms instead of an averaging continuum function. Generally speaking, a system on a coarse length scale can be described by a larger system on a finer length scale.

Consequently the respective models should be related to each other as well. Instead of defining the models empirically and independently on each length scale, it is favorable to strictly derive the models on coarse length scales from the models on fine length scales. This procedure is called *upscaling*. The advantage of this "first principles" based method over the phenomenological approach is that the description of the effects on the finer length scale can be carried forward to the coarser length scale which then allows for a more accurate coarse scale model. Furthermore, the relationship of the scales is explicitly known in this case. This way, a complete hierarchy of scales is set up.

In this thesis we develop an upscaling technique in order to derive a continuum mechanical model from a given atomistic model for crystalline solids. It is capable of transferring many microscopic properties to the continuum level which are lost in classical continuum models. We furthermore employ the resulting model to numerically simulate the behavior of crystalline silicon and shape memory alloys.

On the atomic level, the solid is described by a system of interacting atoms. Here the positions of the atoms are denoted by $y(x) \in \mathbb{R}^d$ for all x from a finite index set, where $d \in \mathbb{N}$ is the spatial dimension. The specific behavior of the material is then determined by a potential energy function

$$\Phi^{(A)}(\{y(x)\}) \tag{1.1}$$

which depends on the atom positions.

On the continuum mechanical level, the deformation of the solid is described by a function $y : \Omega \to \mathbb{R}^d$, where $\Omega \subset \mathbb{R}^d$ denotes the reference configuration. The potential energy $\Phi^{(C)}(y)$ then depends on this deformation function. Often $\Phi^{(C)}(y)$ has the form

$$\Phi^{(C)}(y) = \int_\Omega \Phi^{(C),x}(\nabla y(x)) \, \mathrm{d}x. \tag{1.2}$$

Here the potential energy density $\Phi^{(C),x}$ at some point $x \in \Omega$ depends on the deformation gradient $F = \nabla y(x)$ only. However, we will see in this thesis that more general continuum models are useful in which the energy density additionally depends on higher order derivatives of y.

The classical way to derive a continuum mechanical model from an atomistic model is to consider the thermodynamic limit. This technique has been studied by Blanc, Le Bris and Lions [17], E and Huang [31] and others and will be described in Section 3.4.1. In this approach, the original atoms from the atomistic model are replaced by a larger number of smaller atoms, and then the number N of smaller atoms is driven to infinity. The atomistic potential $\Phi^{(A)}(\cdot)$ which depends on the atom positions is accordingly scaled as

$$\varepsilon^d \Phi^{(A)}(\varepsilon^{-1} \cdot), \tag{1.3}$$

where $\varepsilon > 0$ gives the characteristic length. Therefore, this technique is also called the scaling technique. The limit $\varepsilon \to 0$ then leads to a continuum mechanical energy $\Phi^{(C)}$ of the form (1.2) which serves as the continuum mechanical model.

The time evolution of this continuum mechanical system is governed by the nonlinear wave equation

$$\rho \frac{\partial^2 y}{\partial t^2} = \operatorname{div} \Phi^{(C),x'}(\nabla y), \tag{1.4}$$

where ρ is the mass density and $\Phi^{(C),x'}$ denotes the first derivative of the potential energy density of the system. From the viewpoint of continuum mechanics, $\Phi^{(C),x'}$ describes the stress. It is well known that the solutions of such nonlinear hyperbolic equations typically exhibit shocks after finite time, see e.g. [25]. These equations then possess no classical solutions, even for smooth initial data. Only solutions in a weaker sense exist. This breakdown of solution theory is in contrast to the discrete system which admits a solution for an infinite time horizon. The reason for this is the discreteness of the atomistic system. It leads to a certain dispersion which has a regularizing effect. This dispersion is not contained in the continuum model, because the scaling technique describes the full continuum limit. It drives the number N of atoms to infinity and therefore destroys all discreteness effects. This fact is reflected in the continuum potential (1.2) by the sole dependence of the energy density $\Phi^{(C),x}$ on the deformation gradient ∇y which is a dimensionless quantity.

On the macroscale, further terms are added to the continuum model every now and then, mostly higher order contributions to the potential energy such as $|\nabla^2 y|^2$. This leads to a regularization of the problem as well. Also, further physical effects such as surface contributions or the determination of the length scale can be captured phenomenologically in this way, see e.g. [7] for an example in the context of shape memory alloys. But these additional terms are somewhat artificial. They are mostly chosen phenomenologically and are not deduced from the atomistic model.

To retain the microscopic discreteness effects in the continuum mechanical model, one has to consider the atomistic system for a large, but fixed and finite number N of atoms without passing to the limit $N \to \infty$. This is called the quasi-continuum regime and serves as the starting point of this thesis. The subject of this work is to develop and analyze an upscaling scheme for the derivation of a continuum model from an atomistic model for crystalline solids within the quasi-continuum regime which carries over the microscopic properties and the discreteness effects from the atomic level to the continuum mechanical level. To this end, we develop the so-called inner expansion technique which we first proposed in [6, 5]. It is based on a Taylor series expansion of the deformation function y

up to some order $K \in \mathbb{N}$ and leads to a continuum mechanical potential of the form

$$\Phi^{(\mathrm{C})}(y) = \int_{\Omega} \Phi^{(\mathrm{C}),x}\big(y, \nabla y(x), \nabla^2 y(x), \ldots, \nabla^K y(x)\big) \, \mathrm{d}x. \qquad (1.5)$$

This potential is similar to (1.2), but the energy density $\Phi^{(\mathrm{C}),x}$ additionally depends on the higher order derivatives of y up to the order K.

   We show that the incorporation of the higher order terms allows to properly capture the microscopic properties and the discreteness effects of the underlying atomistic system. Here, the parameter K can be chosen to adjust the quality of approximation. Furthermore, we prove that certain properties such as convexity and atomic invariances of the atomistic model are carried over to the continuum model, which cannot be taken for granted for any upscaling scheme. As a consequence, the resulting macroscopic evolution equations are well-posed.

   At first glance it seems useless to describe the discreteness effects by a continuum model, since the discrete atomistic model could be used directly instead. But this is not true. An advantage of the continuum model is that it is accessible to analytical techniques which allows to further investigate its properties. For the numerical treatment, the continuum mechanical model will be discretized again. This way, i.e. via the continuum model and its successive discretization, the original discrete atomistic model is transformed into another discrete model. The key point here is that the mesh size can be arbitrarily chosen, in contrast to the fixed number of atoms in the original atomistic system. Thus, the discretization error can be controlled. Moreover, it can be balanced with the model error which depends on the degree of approximation used in the derivation of the respective continuum mechanical system. Altogether, the computational accuracy can thus be adjusted to the desired accuracy of the solution. This permits an efficient implementation and makes it possible to simulate larger systems. It even allows for adaptive techniques, if necessary. In this respect the continuum model serves as an averaging tool to pass from the atomic discretization size to an arbitrary discretization size.

   Higher order contributions in continuum mechanics have been used already in 1893 by Van der Waals (see [79] and [68] for the English translation) to describe capillarity effects of fluids. In the context of elasticity theory of solids, they have been studied e.g. by Bardenhagen and Triantafyllidis [77, 11, 78]. A systematic way to derive higher order terms is given by the so-called direct expansion technique. This upscaling technique has first been proposed by Kruskal and Zabusky [53, 85] and was further developed by Rosenau [64] and Collins [22]. Numerical investigations have been performed by Kevrekidis et al. [51]. The technique is based on a Taylor series expansion of the discrete evolution equation. However, the resulting evolution equations are often ill-posed.

   Another upscaling technique for crystalline solids is given by the quasi-continuum method [72, 73, 52]. It is based on regarding each continuum point to be surrounded by a small deformed crystal of representative atoms. The macroscopic constitutive law is then obtained from the atomistic potential of the representative crystal. In the local form, the connection between the macroscopic deformation and the microscopic deformation is given by the Cauchy-Born rule. This results in a first order approximation which does not determine the length scale. In the nonlocal form of the quasi-continuum method, the microscopic atoms are required to precisely follow the finite element approximation of the macroscopic deformation function in a complete neighborhood of each continuum

point. This way discreteness effects can be captured. The adaptive refinement of the finite element mesh allows to control the accuracy of the method. However, the finite element mesh has to be refined up to the atomic lattice to resolve the full microscale behavior. The designation as quasi-continuum method emerges from limiting the mesh size from below to the atomic lattice size.

Besides upscaling schemes which derive a macroscopic model from a microscopic model, but then solely use the macroscopic model for the numerical solution, there also exist coupling schemes which make use of two models at the same time for the numerical calculation. Without claiming completeness, we mention the bridging scales method and the heterogeneous multiscale method. Generally, the macroscopic model is used whenever its accuracy is sufficient, while the microscopic model comes into place otherwise. Let us note that coupling methods cannot be viewed as a replacement for upscaling methods. In fact, the macroscopic models for coupling methods still have to be defined, and this is best done by upscaling. However, let us note that macroscopic models with lower accuracy such as phenomenological models may be sufficient here, since the high accuracy is obtained from the coupling.

The bridging scales method [83] of Liu et al. is based on a projection operator P for the additive decomposition of the full deformation function y into a coarse scale part $\overline{y} = Py$ and a fine scale part $\tilde{y} = (I - P)y$. The projection P is chosen such that the fine scale part $\tilde{y}$ vanishes when the solution y is smooth. This way, the full domain is subdivided into two overlapping subdomains for each scale. The resulting coupled system of governing equations for $\overline{y}$ and $\tilde{y}$ is then solved by an iterative Newton method. Here the equation for the coarse scale $\overline{y}$ is solved on the entire coarse scale domain, while it suffices to solve the equation for the fine scale only in a localized region due to the special choice of the projection operator. However, multiscale boundary conditions and the interscale dependence are complicated. Special attention, for example, has to be paid to prevent non-physical reflections at the interface between the different scales [82].

The heterogeneous multiscale method (HMM) [29, 30] of E et al. provides a general framework for coupling microscopic and macroscopic models numerically. It is based on setting up a coarse grid for the macroscopic model. In regions of this grid where the macroscopic model gives a sufficiently accurate description of the physical process, the macroscopic model is solely used for the numerical computation. In the other regions the microscopic model is used to supply the missing data for the macroscopic model. To this end, the macroscopic state is transferred to the microscale by means of a suitable reconstruction operator, then the solution of the microscopic problem is computed locally on a reduced computational domain, and finally the results are transferred back to the macroscale with a compression operator. This way the macroscale behavior is resolved in the whole domain with an accuracy comparable to the microscopic model.

Beyond the above mentioned methods, many other techniques have been developed. Without targeting completeness, let us note the work of Dreyer et al. [28] and Friesecke et al. [38, 39, 40, 41]. Γ-Limit techniques are studied by Braides et al. [18]. An overview of upscaling techniques and other multiple-scale approaches can be found in [55].

This thesis is organized as follows. Chapter 2 is devoted to the atomic level. First, the atomistic model is described in Section 2.1. Some simple model potentials for an atomic chain in the spirit of the celebrated work of Fermi, Pasta and Ulam [36] are introduced. Then the physically more realistic model of Stillinger-Weber for crystalline silicon and the

Embedded-Atom Method (EAM) for shape memory alloys are defined in Sections 2.2 and 2.3, respectively. We also discuss their efficient numerical implementation and present sample calculations for both models.

In Chapter 3, we discuss the upscaling procedure. First, the inner expansion technique is developed in Section 3.1.1 in order to derive the quasi-continuum model from the atomistic model. In Section 3.2, the technique is applied to the model problems defined in Section 2.1.2. A numerical comparison of the resulting evolution equations allows to judge the outcome of the inner expansion technique. Next, we analytically show in Section 3.3 that important characteristics such as convexity of the atomistic potential are transferred to the continuum level by the inner expansion technique, which leads to well-posed evolution equations. After this, we review the scaling technique and the direct expansion technique and discuss the differences to our technique in Section 3.4. Finally, in Section 3.5 we apply our approach to the model of crystalline silicon to demonstrate that the above mentioned advantages of our technique hold for this realistic and more complex model as well. In Section 3.5.1, the quality of the approximation of the continuum energy is analyzed in the stationary setting. This is done for a system of moderate size, which allows a direct comparison with the atomistic system. From this, the optimal order of approximation can be obtained for a reasonable error tolerance. The results are then used in Section 3.5.2 to simulate the elastic behavior of the crystal for the corresponding evolution equation. The associated continuum system corresponds to an atomistic system of 12 billion atoms, which is impossible to treat directly on the microscale with molecular dynamics techniques up to now.

The inner expansion technique leads to a continuum mechanical potential which is very precise but sometimes rather complex. Therefore we perform a next step in Chapter 4 and approximate it by another continuum mechanical potential which retains the important properties of the original potential but is easier to handle. In doing so, we advance the techniques we proposed in [4]. To this end it is useful to study how certain invariances such as frame indifference and lattice symmetry transfer to the continuum mechanical level. The results are important tools for the subsequent steps and are derived in Section 4.1. Then the principal part which represents the dependence of the potential on the deformation gradient ∇y is decoupled from the higher order contributions in Section 4.2. In Section 4.3, the principal part is approximated for the example of the EAM potential for shape memory alloys. Here the handling of the displaced martensitic strain tensor is worked out in detail which goes beyond the established concept of the austenitic strain tensor. As the principal part constitutes the fundamental material behavior, this is an essential topic, although independent of the higher order contributions which make up the key aspect of this thesis. We then employ the obtained model to numerically simulate the operating of micro-actuators made of the $Ni_{64}Al_{36}$ shape memory alloy in Section 4.4. Finally, we address the higher order part and deduce an improved model with higher order contributions for the simulation of shape memory alloys in Section 4.5.

Altogether, these three chapters describe the upscaling process from the atomistic model via the full continuum model up to the approximated continuum model in the natural order. This structure is depicted in Figure 1.1.

Chapter 5 provides the numerical techniques which are necessary to solve the continuum mechanical evolution equations which arise in Chapter 3. Here a finite difference scheme of high consistency order for the hyperbolic evolution equations is developed. The
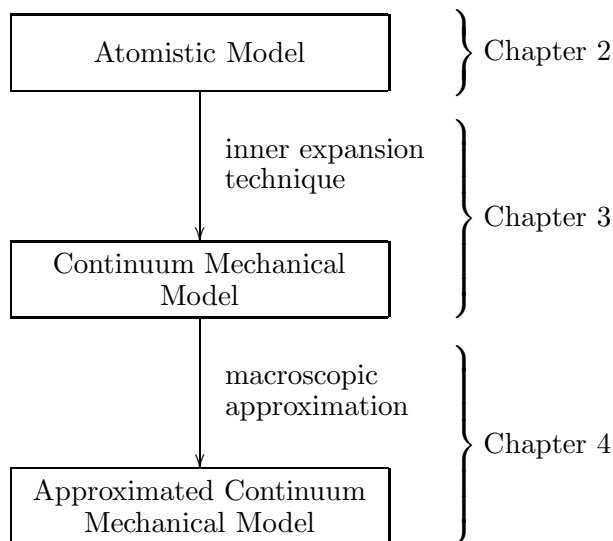
Figure 1.1: Structure of the upscaling process.

high consistency order is crucial for the comparison of the different models, since the consistency error would otherwise interfere with the higher order derivative terms of the different PDEs and thus falsify the comparison. Chapter 5 is therefore not part of the strictly linear arrangement of the preceding three chapters. The numerical techniques developed here are separated from the above in order to avoid an interruption of the upscaling procedure.

Chapter 2

Atomic Level

The basis of this work is the physical model on the atomic length scale. Here, the behavior of the crystalline solid under consideration is described by means of a system of interacting atoms. From this atomistic model, a continuum mechanical model will be derived in the next chapter. Thus we naturally begin with the definition of the atomistic model.

Here we confine ourselves to the fundamentals which are necessary for the subsequent upscaling technique. More information about molecular dynamics, its applications and the related numerical techniques can be found in any of the well-known textbooks on this topic, e.g. [2], [37], [42], [43] and [45].

First, we introduce the basic notation of the atom positions and the reference configuration in Section 2.1.1. In Section 2.1.2, we define the potential energy, which constitutes the behavior of the specific material. Furthermore, three simple model problems are defined here. In Section 2.1.3, we derive the equations of motion. The basic thermodynamic quantities are defined in Section 2.1.4. Then, the introduced techniques are applied to the physically relevant models of crystalline silicon and of shape memory alloys in Sections 2.2 and 2.3, respectively. Both the model problems and the realistic models will be subject to the upscaling procedure in the next chapters, such that it is important to describe them in detail here. Moreover, we perform molecular dynamics simulations of these applications for illustration.

2.1 Molecular Dynamics

2.1.1 Atom Positions

On the atomic length scale, the specimen under consideration is described by a system of N interacting atoms, sometimes also called particles. For crystals we are concerned with here, the positions of these atoms in the natural unstressed state are arranged in form of a lattice $\mathcal{L}$. The regular structure of the lattice will be exploited in the next chapter when we come to the upscaling procedure.

The lattice $\mathcal{L}$ is the periodic infinite discrete set of atom positions

$$\mathcal{L} := \{x + Az \mid x \in \mathcal{L}_{\text{cell}}, z \in \mathbb{Z}^d\}, \tag{2.1}$$

where $A \in \text{GL}(d, \mathbb{R})$ is a regular matrix and where $d \in \mathbb{N}$ denotes the spatial dimension.[1]

---

[1]For notational simplicity we assume here that the lattice of the crystal in the reference configuration
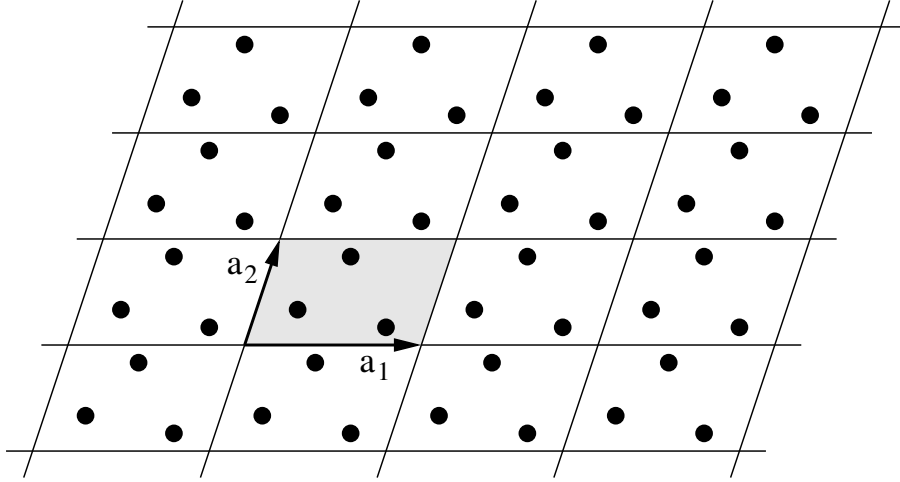
Figure 2.1: Two-dimensional example of a lattice $\mathcal{L}$ with its base cell and its spanning vectors.

The base cell $\mathcal{L}_{\text{cell}} \subset \mathbb{R}^d$ is assumed to be non-empty and to consist of a small, finite number of atoms. In other words, $\mathcal{L}$ is the periodic continuation of $\mathcal{L}_{\text{cell}}$ along the parallelepiped which is spanned by the column vectors $a_1, a_2, \ldots, a_d \in \mathbb{R}^d$ of the matrix A. Figure 2.1 gives a two-dimensional example.

Now we choose this natural state as the reference configuration. This means that the atom positions in the reference configuration of the crystal are given by

$$\mathcal{L} \cap \Omega, \tag{2.2}$$

where the domain $\Omega \subset \mathbb{R}^d$ describes the form of the crystal.

A deformation in space of the crystal can be described by a function

$$y : \mathcal{L} \cap \Omega \to \mathbb{R}^d, \tag{2.3}$$

which maps the reference configuration to the deformed state. A point $x \in \mathcal{L} \cap \Omega$ from the reference configuration is thus moved to $y(x)$ under deformation. Note that the positions of the atoms $\mathcal{L} \cap \Omega$ of the reference configuration now only act as an index set. The set of atom positions $y(\mathcal{L} \cap \Omega)$ describes the shape of the deformed crystal.

Later we will also consider time dependent deformations, that means functions $y = y(x,t)$ which additionally depend on the time t. Then the velocity of the atom at x in the reference configuration is given by the time derivative $y_t(x,t)$.

2.1.2   Potential Energy

The behavior of the atomistic system is determined by the potential energy function $\Phi^{(A)}$. This can in principle be any function which depends on the atom positions. Thus, the potential energy of the deformed crystal can be written as

$$\Phi^{(A)}(\{y(x)\}_{x \in \mathcal{L} \cap \Omega}). \tag{2.4}$$

---

is homogeneous. This means that the orientation and the structure of the lattice cannot change for different regions of the crystal. Consequently, the notation does not include polycrystals here, although the mathematics later would work for this case, too.
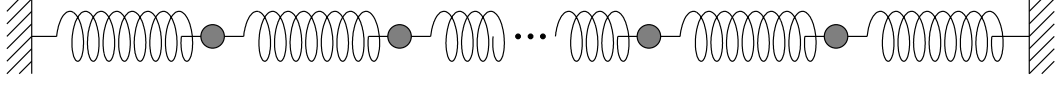
Figure 2.2: Atomic chain with springs and fixed boundary.

Some first specific examples for $\Phi^{(A)}$ will be given below.

We assume that the potential can be split into a sum of local interactions $\Phi^{(A),\overline{x}}$ around some points $\overline{x}$:

$$\Phi^{(A)}(\{y(x)\}_{x\in\mathcal{L}\cap\Omega}) = \sum_{\overline{x}\in\overline{\mathcal{L}}\cap\Omega} \Phi^{(A),\overline{x}}(\{y(x)\}_{x\in\mathcal{L}\cap\Omega}). \qquad (2.5)$$

Almost all physically meaningful potentials allow such a localization. The points $\overline{x}$ can be interpreted as the center points of the local interactions. For example, $\overline{x}$ can be chosen as $\frac{1}{2}(x + \tilde{x})$ if $\Phi^{(A),\overline{x}}$ denotes the pair interaction of two atoms $y(x)$ and $y(\tilde{x})$. The precise location of the points $\overline{x}$ will only be relevant for the inner expansion technique later. Thus, we postpone their exact choice to Section 3.1.3. For now it suffices to treat the positions of the points $\overline{x}$ just as an index set.

Since the atom positions are arranged in form of a lattice $\mathcal{L}\cap\Omega$, it makes sense to assume that this holds for the points $\overline{x}$ as well. The set of center points $\{\overline{x}\}$ then forms the associated lattice $\overline{\mathcal{L}}\cap\Omega$, where

$$\overline{\mathcal{L}} := \{\overline{x} + \overline{A}z \mid \overline{x}\in\overline{\mathcal{L}}_{\text{cell}}, z\in\mathbb{Z}^d\} \qquad (2.6)$$

for some matrix $\overline{A}\in\text{GL}(d,\mathbb{R})$ and some nonempty and finite set $\overline{\mathcal{L}}_{\text{cell}}\subset\mathbb{R}^d$. Note that the lattice $\overline{\mathcal{L}}$ may, but need not coincide with the original lattice $\mathcal{L}$.

Example 1. The most simple example is the atomic chain in one dimension. Despite of its simplicity, it serves quite well as a model problem. Many effects from physically more complex situations can already be observed and studied with this model. We consider the domain $\Omega = (0, L)$ for some integer $L > 0$ and place the atoms at the points $1, 2, 3, \ldots, L-2, L-1$. The lattice is then given by $\mathcal{L} = \mathbb{Z}$.

We assume that adjacent particles are connected by a spring of length one in the undeformed state. Furthermore, the chain is fixed at both ends, see Figure 2.2. The springs are assumed to obey Hooke's law with the spring constant normalized to 1. This gives rise to the potential

$$\Phi^{(A)}(\{y(x)\}_{x\in\mathcal{L}\cap\Omega}) = \sum_{x=0}^{L-1} \varphi\big(y(x+1) - y(x)\big) \qquad (2.7)$$

where

$$\varphi(r) = \frac{1}{2}(r-1)^2 \qquad (2.8)$$

for a deformation y. Here we assume $y(x) = x$ for all lattice points outside Ω, that is for all $x\in\mathcal{L}\setminus\Omega$. This implements Dirichlet-like boundary conditions, i.e. the specimen is subject to the identity deformation at its boundary. Note that these points outside Ω only denote "fixed particles" without any degree of freedom. They help to express the potential in a short form, but do not constitute particles of the system.
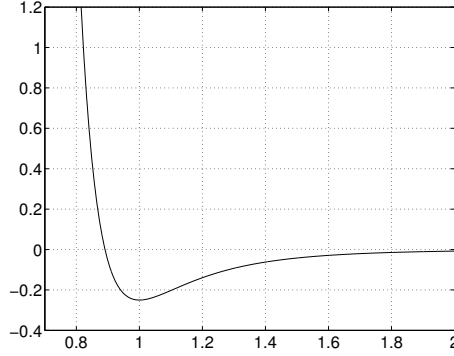
Figure 2.3: Function φ with $\sigma = 2^{-1/6}$ for the Lennard-Jones potential.

We localize the potential by splitting it into the pair interactions. This leads to

$$\Phi^{(A)}(\{y(x)\}_{x \in \mathcal{L} \cap \Omega}) = \sum_{\overline{x} \in \overline{\mathcal{L}} \cap \Omega} \Phi^{(A),\overline{x}}(\{y(x)\}_{x \in \mathcal{L} \cap \Omega}) \qquad (2.9)$$

where

$$\Phi^{(A),\overline{x}}(\{y(x)\}_{x \in \mathcal{L} \cap \Omega}) = \varphi\left(y\left(\overline{x} + \tfrac{1}{2}\right) - y\left(\overline{x} - \tfrac{1}{2}\right)\right) \qquad (2.10)$$

with the associated lattice $\overline{\mathcal{L}} = \mathbb{Z} + \tfrac{1}{2}$.

Example 2. We now consider the well-known Lennard-Jones potential

$$\Phi^{(A)}(\{y(x)\}_{x \in \mathcal{L} \cap \Omega}) = \sum_{\substack{x,\tilde{x} \in \mathcal{L},\, x < \tilde{x} \\ x \in \Omega \text{ or } \tilde{x} \in \Omega}} \varphi(y(x) - y(\tilde{x})) \qquad (2.11)$$

where

$$\varphi(r) = \left(\frac{\sigma}{r}\right)^{12} - \left(\frac{\sigma}{r}\right)^{6}. \qquad (2.12)$$

As in Example 1, the domain is given by $\Omega = (0, L)$ and let the lattice be $\mathcal{L} = \mathbb{Z}$. Once more, we assume $y(x) = x$ for all $x \in \mathcal{L} \setminus \Omega$ to prescribe Dirichlet-like boundary conditions. Again, this leads to a description of a finite chain which is embedded into an infinite undeformed chain. The side condition in the sum guarantees that each pair of particles from the infinite lattice is accounted for exactly once if it contributes to $\Omega \cap \mathcal{L}$ at all. The localization of the Lennard-Jones potential will be given in Section 3.2.2.

The parameter $\sigma \in \mathbb{R}^+$ determines the lattice constant. The function φ possesses a sole minimum at $r = 2^{1/6}\sigma$ for positive arguments r. For the choice $\sigma = 2^{-1/6}$ this minimum would be located at the lattice distance $r = 1$, see Figure 2.3. Note however that this choice does not make the identity deformation $y(x) = x$ a minimizer of the potential energy of the system, since only adjacent particles are in the minimum of φ, whereas all other particle pairs (with larger distances) contribute to the potential energy by an attracting part. Therefore the minimum distance is slightly smaller. We compensate for this by choosing σ slightly larger such that the minimum of the potential energy of the overall system is attained at $r = 1$. The corresponding parameter σ can be computed as follows: The potential energy of a particle in an infinite chain with lattice distance one is

s	$\zeta(s)$		
6	$\displaystyle\sum_{z=1}^{\infty}\frac{1}{z^6}$	$=\dfrac{\pi^6}{945}$	$= 1.01734306198444913971451792979\ldots$
12	$\displaystyle\sum_{z=1}^{\infty}\frac{1}{z^{12}}$	$=\dfrac{691\pi^{12}}{638512875}$	$= 1.00024608655330804829863799805\ldots$

Table 2.1: Values of the Riemann ζ-function.

given by

$$\frac{1}{2}\sum_{z\in\mathbb{Z}\backslash\{0\}}\varphi(z) = \sum_{z=1}^{\infty}\left[\left(\frac{\sigma}{z}\right)^{12} - \left(\frac{\sigma}{z}\right)^{6}\right] = \zeta(12)\sigma^{12} - \zeta(6)\sigma^{6}, \qquad (2.13)$$

where ζ denotes the Riemann ζ-function

$$\zeta(s) = \sum_{z=1}^{\infty}\frac{1}{z^s}. \qquad (2.14)$$

We require the first derivative of (2.13) with respect to σ to vanish, hence we choose

$$\sigma = \left(\frac{\zeta(6)}{2\zeta(12)}\right)^{\frac{1}{6}}. \qquad (2.15)$$

The values $\zeta(6)$ and $\zeta(12)$ are given in Table 2.1. Since they are close to one, the use of σ as in (2.15) is only a small modification to the previous choice $\sigma = 2^{-\frac{1}{6}}$.

All in all, the choice (2.15) for σ makes the lattice a minimizer of the potential energy among all atom configurations with constant particle spacing. A further argumentation reveals that this configuration is indeed a minimizer among all possible particle configurations, including those without constant particle spacing.

Both, the spring potential and the Lennard-Jones potential, are pair potentials, i.e. they can be written as a sum of terms, each of which depends only on the positions of two atoms. This restriction however prevents the modeling of many physical properties. It can be shown, for example, that each pair potential exhibits the symmetry relation $\mathbb{C}_{12} = \mathbb{C}_{44}$ for the resulting elastic moduli, the so-called Cauchy relation [27]. Physical measurements of the elastic moduli of real solids however show that this symmetry is often not valid. Thus, pair potentials are not sufficient to model solids. Physically more meaningful potentials for different materials have been developed by Brenner [19], Stillinger and Weber [70], Abell and Tersoff [1, 74], Daw and Baskes [26, 27] (Embedded-Atom Method, see Section 2.3.1) and many others. They all involve many-body interactions. Note that these potentials can also be localized as in (2.5) and are thus suitable for the inner expansion technique described in Chapter 3.

As a simple model problem for many-body interactions, we use the following example.

Example 3. Again, we consider the atomic chain. Both the lattice and the associated lattice are given by $\mathcal{L} = \overline{\mathcal{L}} = \mathbb{Z}$. Analogously to the two-body spring potential of Example 1, we define the following three-body interaction potential

$$\Phi^{(A)}(\{y(x)\}_{x\in\mathcal{L}\cap\Omega}) = \sum_{x=1}^{L-1}\varphi\big(y(x+1) - 2y(x) + y(x-1)\big) \qquad (2.16)$$

where

$$\varphi(r) = \frac{1}{2}r^2. \tag{2.17}$$

In localized form, it reads as

$$\Phi^{(A)}(\{y(x)\}_{x \in \mathcal{L} \cap \Omega}) = \sum_{\overline{x} \in \overline{\mathcal{L}} \cap \Omega} \Phi^{(A),\overline{x}}(\{y(x)\}_{x \in \mathcal{L} \cap \Omega}) \tag{2.18}$$

where

$$\Phi^{(A),\overline{x}}(\{y(x)\}_{x \in \mathcal{L} \cap \Omega}) = \frac{1}{2}\big(y(\overline{x}+1) - 2y(\overline{x}) + y(\overline{x}-1)\big)^2. \tag{2.19}$$

Clearly the reference configuration is a minimizer of the potential energy.

2.1.3   Equations of Motion

The potential energy can be used in several ways. First of all, stationary or quasi-stationary configurations of the atomistic system can be sought. They are characterized by the fact that they minimize the potential energy, either globally or locally. To compute such stationary or quasi-stationary configurations of the atomistic system, minimization algorithms are developed to find a set of atom positions which minimizes the potential energy.

However, it is quite often more interesting to track the evolution of the system over time, away from the stationary setting. The time evolution is governed by Newton's second law of motion. It states that the acceleration $a = y_{tt}(x,t)$ of an atom $y(x,t)$ at time t equals the force acting on it divided by its mass $m(x)$, i.e. $a = F/m$. The force is given by the negative gradient of the potential energy with respect to the atom position $y(x,t)$. This means that the force points towards the direction of steepest descent of the potential energy. Thus Newton's law in our notation reads as

$$m(x)y_{tt}(x,t) = -\nabla_{y(x,t)}\Phi^{(A)}(\{y(\tilde{x},t)\}_{\tilde{x} \in \mathcal{L} \cap \Omega}) \tag{2.20}$$

for all $x \in \mathcal{L} \cap \Omega$. This gives a system of ordinary differential equations (ODE) for all atom positions.

In this instationary setting, the system also tends to minimize the potential energy. But each descent of the potential energy results in an acceleration of the atoms and therefore in an increase of the kinetic energy

$$E_{\mathrm{kin}}(t) = \frac{1}{2}\sum_{x \in \mathcal{L} \cap \Omega} m(x)|y_t(x,t)|^2. \tag{2.21}$$

Vice versa, the mass inertia of the system allows the system to move in direction of increasing potential energy, which slows down the atoms and therefore decreases the kinetic energy. Altogether, the potential and the kinetic energy cancel each other out, which is known as the law of energy conservation.

Two more alternative descriptions of the law of evolution are given by means of the Lagrange function and the Hamilton equations. It is easy to verify that they are both equivalent to Newton's second law. The Lagrange function $\mathscr{L}$ is defined by

$$\mathscr{L}(y,v) := \frac{1}{2}\sum_{x \in \mathcal{L} \cap \Omega} m|v(x)|^2 - \Phi^{(A)}(\{y(\tilde{x})\}_{\tilde{x} \in \mathcal{L} \cap \Omega}). \tag{2.22}$$

where $v = y_t$ denotes the velocity of the atoms. The evolution is now governed by the requirement that y is a stationary point of the action integral

$$\mathscr{I}(y) := \int_0^T \mathscr{L}(y(t), \dot{y}(t)) \, \mathrm{d}t \tag{2.23}$$

for the considered time interval $(0, T)$. This means that the first variation

$$\delta\mathscr{I}(y; z) := \lim_{s \searrow 0} \frac{\mathscr{I}(y + sz) - \mathscr{I}(y)}{s} = \int_0^T \mathscr{L}_{,y}(y, y_t)z + \mathscr{L}_{,v}(y, y_t)z_t \, \mathrm{d}t \tag{2.24}$$

vanishes for all directions $z \in C_c^\infty((0, T))$. By means of the Legendre transformation one obtains the Hamilton function

$$\mathscr{H}(y, p) := \sum_{x \in \mathcal{L} \cap \Omega} \frac{|p(x)|^2}{m} - \mathscr{L}\left(y, \frac{p}{m}\right) = \frac{1}{2} \sum_{x \in \mathcal{L} \cap \Omega} \frac{|p(x)|^2}{m} + \Phi^{(A)}(y). \tag{2.25}$$

Here $p = my_t$ plays the role of the momentum. Then the third description of the evolution is given by the Hamilton equations

$$y_t = \mathscr{H}_p(y, p), \qquad p_t = -\mathscr{H}_y(y, p). \tag{2.26}$$

Because of

$$\frac{\mathrm{d}}{\mathrm{d}t}\mathscr{H}(y, p) = \mathscr{H}_y(y, p)y_t + \mathscr{H}_p(y, p)p_t \overset{(2.26)}{=} \mathscr{H}_y(y, p)\mathscr{H}_p(y, p) - \mathscr{H}_p(y, p)\mathscr{H}_y(y, p) = 0 \tag{2.27}$$

and because $\mathscr{H}$ equals the total energy $E_{\mathrm{kin}} + \Phi^{(A)}$, each such system is energy conserving.

2.1.4 Thermodynamic Quantities

Now, we will derive two important macroscopic quantities from the atomistic system, namely the temperature and the pressure. They serve as important observables for an atomistic system.

The *instantaneous temperature* $\vartheta(t)$ of the system at time t is defined by

$$\vartheta_{\mathrm{inst}}(t) = \frac{2E_{\mathrm{kin}}(t)}{N_f k_{\mathrm{B}}} = \frac{1}{N_f k_{\mathrm{B}}} \sum_{x \in \mathcal{L} \cap \Omega} m|y_t(x, t)|^2, \tag{2.28}$$

where $k_{\mathrm{B}} = 1.3806503$ J/K denotes the Boltzmann constant and $N_f = d|\mathcal{L} \cap \Omega|$ depicts the number of degrees of freedom.[2] Because the instantaneous temperature is a rapidly oscillating quantity, it makes sense to define the *temperature* ϑ as the time average

$$\vartheta := \langle \vartheta_{\mathrm{inst}} \rangle = \frac{1}{t_2 - t_1} \int_{t_1}^{t_2} \vartheta_{\mathrm{inst}}(t) \, \mathrm{d}t \tag{2.29}$$

over some time interval (t_1, t_2).

---

[2]Sometimes N_f is reduced by d to compensate for the translational invariance of the potential. Moreover, rotational invariance or other invariances can be taken into account.

The *pressure* describes the tendency of the system to undergo macroscopic deformations. Since the system is invariant with respect to translations, such a deformation is best approximated in first order by a linear mapping $y \mapsto Ay$ for some matrix $A \in \mathbb{R}^{d \times d}$. This comprises expansion, compression and shearing deformations. From the thermodynamical point of view, the pressure tensor is the negative derivative of the free energy $F = U - TS$ with respect to A. Here it is sufficient to equate the inner energy U with the potential energy $\Phi^{(A)}$ and the product TS of the temperature T and the entropy S with the kinetic energy E_{kin}. Thus the two respective parts of the derivative compute as

$$
\begin{aligned}
\Pi_{\text{kin}} &= \frac{\partial}{\partial A} E_{\text{kin}}(Ay_t)\Big|_{A=\text{Id}} = \frac{\partial}{\partial A} \frac{1}{2} \sum_{x \in \mathcal{L} \cap \Omega} m(x) y_t(x)^T A^T A y_t(x)\Big|_{A=\text{Id}} \\
&= \sum_{x \in \mathcal{L} \cap \Omega} m(x) A y_t(x) y_t(x)^T\Big|_{A=\text{Id}} = \sum_{x \in \mathcal{L} \cap \Omega} m(x) y_t(x) y_t(x)^T
\end{aligned}
\tag{2.30}
$$

and

$$
\Pi_{\text{pot}} = \frac{\partial}{\partial A} \Phi^{(A)}(Ay)\Big|_{A=\text{Id}} = \sum_{x \in \mathcal{L} \cap \Omega} \Phi^{(A)}_{,y(x)}(Ay) y(x)^T\Big|_{A=\text{Id}} = \sum_{x \in \mathcal{L} \cap \Omega} \Phi^{(A)}_{,y(x)}(y) y(x)^T.
\tag{2.31}
$$

The *instantaneous pressure tensor* Π_{inst} is then given by the normalization over the volume V of these expressions:

$$
\Pi_{\text{inst}} = \frac{1}{V} \sum_{x \in \mathcal{L} \cap \Omega} \left(m y_t(x) y_t(x)^T - \Phi^{(A)}_{,y(x)}(y) y(x)^T \right).
\tag{2.32}
$$

Similar to the temperature before, the *pressure tensor* is then defined as the time average

$$
\Pi = \langle \Pi_{\text{inst}} \rangle = \int_{t_1}^{t_2} \Pi_{\text{inst}}(t) \, \mathrm{d}t
\tag{2.33}
$$

of the instantaneous pressure tensor.

For many atomistic systems, the particular components of the velocity are uncorrelated, i.e. $\langle y_t^\alpha(x) y_t^\beta(x) \rangle = 0$ for $\alpha \neq \beta$, $\alpha, \beta = 1, \ldots, d$. As a consequence, the kinetic part of the pressure tensor is diagonal. Furthermore, if $\Phi^{(A)}$ is a pair potential like the spring potential in Example 1 or the Lennard-Jones potential in Example 2, the potential part of the pressure tensor can be written as

$$
\frac{1}{2dV} \left\langle \sum_{x, \tilde{x} \in \mathcal{L} \cap \Omega} F_{x, \tilde{x}}(y(x) - y(\tilde{x})) \right\rangle,
\tag{2.34}
$$

where $F_{x, \tilde{x}}$ denotes the force between the atoms $y(x)$ and $y(\tilde{x})$. This is the most frequently found form of the pressure tensor in literature.

Now, the *pressure* as a scalar quantity measures the tendency of the system to change its volume. It can be derived from the pressure tensor as follows. As already discussed before, the system tends to macroscopically change from the current configuration $\{y(x)\}_{x \in \mathcal{L} \cap \Omega}$ in direction $\{(\text{Id} + \Pi) y(x)\}_{x \in \mathcal{L} \cap \Omega}$, or precisely it tends to follow the path of the affine deformation described by the matrix $\text{Id} + s\Pi$ for small $s \in \mathbb{R}^+$. The normalized

volume of this transformation is given by its determinant. Thus the change of volume computes as

$$\frac{\partial}{\partial s} \det(\mathrm{Id} + s\Pi)\Big|_{s=0} = \frac{\partial}{\partial s}\Big(1 + s\,\mathrm{tr}(\Pi) + \mathcal{O}(s^2)\Big)\Big|_{s=0} = \mathrm{tr}(\Pi), \qquad (2.35)$$

where $\mathrm{tr}(\Pi)$ denotes the trace of the matrix Π. The pressure P is now defined as this quantity divided by the spatial dimension d:

$$P = \frac{1}{d}\,\mathrm{tr}(\Pi). \qquad (2.36)$$

In other words, the pressure is the arithmetic average of the diagonal elements of the pressure tensor. Similarly, the instantaneous pressure is defined as this quantity without the time average.

These thermodynamical quantities can be used as observables to characterize an atomistic system. Additionally, it is possible to perform molecular dynamics simulations within other ensembles which preserve one or more of these quantities. Up to now, we dealt with the so-called NVE ensemble which preserves the number of atoms (N), the volume (V) and the total energy (E). Other popular ensembles are the NVT ensemble which preserves the temperature (T), but in general not the total energy, and the NPT ensemble which preserves the temperature and the pressure instead of the volume and the total energy.

To this end, a number of different techniques have been developed. In order to control the temperature, the Berendsen thermostat [15] can be used which scales the atom velocities with a uniform factor in each time step to achieve the desired value. Another common method has been proposed by Andersen [3] and is based on enriching the Lagrangian by additional variables for the temperature, the pressure or other quantities. From this extended Lagrangian, the modified equations of evolution are then derived. This principle has been employed within the so-called Nosé-Hoover thermostat [47, 48, 57, 58] to perform molecular dynamics simulations within the NVT ensemble. Similarly, the Parrinello-Rahman method [59, 60] controls the shape of the simulation box to prescribe the stress this way. Quite often, both techniques are combined for simulations within the NPT ensemble.

2.2 Application to Crystalline Silicon

Up to now, we only considered one-dimensional model problems. Next, we come to the simulation of crystalline silicon as the first realistic three-dimensional example.

A widely used potential for the atomistic simulation of silicon has been given by Stillinger and Weber [70, 71]. Since the upscaling technique will be applied to this potential in the next chapter, it is necessary to precisely define it here. This will be done in Section 2.2.1. Then, in Section 2.2.2 we will make some short remarks how the locality of this potential it exploited for an efficient implementation. Finally, the results of the numerical simulation of silicon on the atomic level are presented in Section 2.2.3.

2.2.1   Stillinger-Weber Potential

The potential of Stillinger and Weber for silicon consists of two- and three-body interactions and reads as

$$\Phi^{(A)}(\{y(x)\}_{x \in \mathcal{L} \cap \Omega}) = \frac{1}{2} \sum_{x_1, x_2} \varphi_2(|y(x_2) - y(x_1)|) \tag{2.37}$$

$$+\frac{1}{2} \sum_{x_1, x_2, x_3} \varphi_3\left(|y(x_2) - y(x_1)|, |y(x_3) - y(x_1)|, \frac{(y(x_2) - y(x_1)) \cdot (y(x_3) - y(x_1))}{|y(x_2) - y(x_1)||y(x_3) - y(x_1)|}\right).$$

Here the summation is over all $x_1, x_2, x_3 \in \mathcal{L} \cap \Omega$ with $x_1 \neq x_2 \neq x_3 \neq x_1$. The two- and three-body terms are given by

$$\varphi_2(r) = \begin{cases} \varepsilon A \left(B \dfrac{\sigma^4}{r^4} - 1\right) \exp \dfrac{\sigma}{r - \sigma b} & \text{if } r < \sigma b, \\ 0 & \text{otherwise,} \end{cases} \tag{2.38}$$

$$\varphi_3(r_{12}, r_{13}, \Theta) = \begin{cases} \varepsilon \lambda \exp \left(\dfrac{\gamma \sigma}{r_{12} - \sigma b} + \dfrac{\gamma \sigma}{r_{13} - \sigma b}\right) \left(\Theta + \dfrac{1}{3}\right)^2 & \text{if } r_{12} < \sigma b \text{ and } r_{13} < \sigma b, \\ 0 & \text{otherwise.} \end{cases}$$
$$\tag{2.39}$$

For both types of interactions, the exponential terms serve as smooth cutoff functions, which make the potential local. The pair interaction φ_2 attains its minimum for the nearest neighbor distance in the lattice and therefore stabilizes the equilibrium distance of two adjacent atoms in the lattice. The variable Θ denotes the cosine of the angle between $y(x_2) - y(x_1)$ and $y(x_3) - y(x_1)$. The triple term attains its minimum for the angle $\arccos\left(-\frac{1}{3}\right) \approx 109.47°$. The involved constants are

$$A = 7.049556277, \quad \lambda = 21.0, \quad \sigma = 0.20951\,\text{nm}, \quad b = 1.8,$$
$$B = 0.6022245584, \quad \gamma = 1.2, \quad \varepsilon = 50\,\text{kcal/mol}. \tag{2.40}$$

Together, the pair and triple interactions result in an overall potential which is minimal just if the atoms are arranged in the so-called diamond structure. This is the natural lattice structure of silicon. It consists of two nested fcc lattices. With the notation of (2.1), the lattice can be written as

$$\mathcal{L}_{\text{cell}} = \frac{a_0}{4} \left\{ \begin{pmatrix} 0 \\ 0 \\ 0 \end{pmatrix}, \begin{pmatrix} 2 \\ 2 \\ 0 \end{pmatrix}, \begin{pmatrix} 0 \\ 2 \\ 1 \end{pmatrix}, \begin{pmatrix} 2 \\ 0 \\ 1 \end{pmatrix}, \begin{pmatrix} 1 \\ 1 \\ 2 \end{pmatrix}, \begin{pmatrix} 3 \\ 3 \\ 2 \end{pmatrix}, \begin{pmatrix} 1 \\ 3 \\ 3 \end{pmatrix}, \begin{pmatrix} 3 \\ 1 \\ 3 \end{pmatrix} \right\} \tag{2.41}$$

and $A = a_0 I$, where I denotes the 3×3 unit matrix and $a_0 = 0.54309$ nm denotes the lattice constant. Figure 2.4 shows a part of the lattice. Here, pairs of nearest neighbor atoms are connected by bonds.

2.2.2   Linked-Cell Technique

We now come to the implementation of the Stillinger-Weber potential. A molecular dynamics program numerically computes the trajectories of the atoms. To this end, the
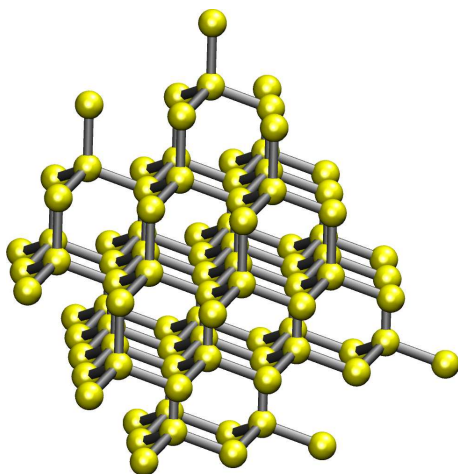
Figure 2.4: Diamond structure of a silicon crystal.

evolution equations (2.20) are discretized in time and solved afterwards. There are a number of common techniques available; it does not lie within the scope of this thesis to study them. A detailed description of them can be found in any of the above-mentioned textbooks about molecular dynamics. Let us just state that the potential energy and its spatial derivatives have to be evaluated in each time step. This evaluation is the crucial point for the efficiency of an implementation, hence it is necessary to discuss this point.

The straightforward evaluation of the sum (2.38) for the two-body terms requires $\mathcal{O}(N^2)$ operations in each time step, where $N = |\mathcal{L} \cap \Omega|$ denotes the number of atoms. If N is large, this becomes computationally very time-consuming. For the three-body terms, $\mathcal{O}(N^3)$ operations are necessary, which is even worse. However, the locality of the potential can be exploited to reduce the computational complexity.

A pair potential $\varphi_2(r)$ is called local if there is a constant $r_0 > 0$ such that $\varphi_2(r) = 0$ for all $r \geq r_0$. This is fulfilled for (2.38) with $r_0 = \sigma b$. Quite often, rapidly decaying potentials such as the Lennard-Jones potential are also considered local by setting them to zero for $r \geq r_0$. In this case, the constant r_0 is called the cutoff radius. It has to be chosen carefully not to falsify the potential too much.

For a local pair potential, it is sufficient to take only the interactions between those atoms into account whose distance it at most r_0. This way, the computational costs can be reduced considerably. To this end, a number of algorithms have been developed such as Verlet lists [80] and the linked-cell technique. The latter has been proposed by Hockney and Eastwood [45] and will be used here. Note that these techniques are purely algorithmic, in contrast to other methods such as tree methods and grid based methods for long range potentials like the electrostatic or the gravitational potential, in which the potential itself is approximated to obtain a better computational efficiency. Since the linked-cell technique is rather standard for pair potentials, we only sketch it briefly. An extensive description and detailed implementation hints are given in [45] and [42]. Nevertheless, the extension to a three-body potential exhibits certain peculiarities, hence we discuss this point in more detail below.

For the linked-cell technique, all atoms are assumed to stay within a cubic simulation
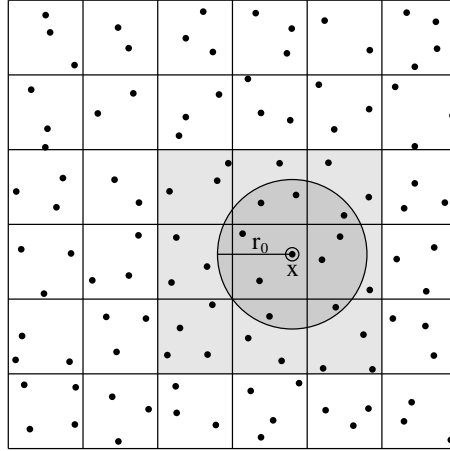
Figure 2.5: Linked-cell method: The region of influence (dark gray circle) around the
marked atom lies within the neighboring cells (light gray).

box.[3] This box is now divided into M^d smaller cubes by dividing each edge of the sim-
ulation box into M parts of equal length. Each such smaller cube is called a cell. The
parameter M is chosen such that the edge length of each cell is at least r_0, but does not
exceed it by far. Then, all atoms within the simulation box are assigned to the respective
cell in which they are contained. This is usually done by maintaining a list of atoms for
each cell.

Now observe that the locality property implies that only interactions of atoms within
the same or within the $3^d - 1$ neighboring cells have to be considered, see Figure 2.5. From
the figure one can clearly realize that the so-called region of influence, given by the ball
$\{\tilde{y} \in \mathbb{R}^d : |\tilde{y} - y(x)| < r_0\}$ around each atom $y(x)$, is a subset of these 3^d cells. For a
uniformly distributed set of atoms, this reduces the number of operations from $\mathcal{O}(N^2)$ to
$\mathcal{O}(N^2/M^d)$. Since the number N/M^d of atoms in a cell is usually a bounded number (r_0
is a fixed multiple of the equilibrium distance), this in fact yields the complexity $\mathcal{O}(N)$.

Additionally, we employ Newtons third law to further restrict the search for interacting
atom pairs. Since the pairs $(y(x_1), y(x_2))$ and $(y(x_2), y(x_1))$ have the same potential
energy, it is sufficient to take only one of these pairs into account. To this end, we
introduce an arbitrary numbering of the atoms. We then restrict the search to all pairs
$(y(x_1), y(x_2))$ with $y(x_1) < y(x_2)$ according to this numbering. Trivially, we have

$$\frac{1}{2} \sum_{x_1, x_2} \varphi_2(|y(x_2) - y(x_1)|) = \sum_{x_1, x_2: \, y(x_1) < y(x_2)} \varphi_2(|y(x_2) - y(x_1)|). \qquad (2.42)$$

This way, the set of pairs to be handled is halved. In most implementations, a natural
numbering is already given by the numbering of the cells and subsequently the numbering
of the atoms within each cell from the atom list.

A three-body potential such as (2.39) can in principle be handled by the linked-cell
technique similarly to a two-body potential. However, we then have to deal with three

---

[3]Sometimes rectangular boxes or more general shapes such as parallelepipeds are used. Here we stick
to a cubic box for a simple description.

distances $|y(x_1) - y(x_2)|$, $|y(x_1) - y(x_3)|$ and $|y(x_2) - y(x_3)|$, each of which may be subject to a different cutoff radius. Thus there are several different ways to define locality in case of triple interactions $(y(x_1), y(x_2), y(x_3))$. For an efficient implementation, it is crucial to pay attention to the precise locality condition for the respective potential.

If the cutoff radius is the same for all three distances, it is best to introduce a numbering as above and restrict the search to all triples $(y(x_1), y(x_2), y(x_3))$ which fulfill $y(x_1) < y(x_2) < y(x_3)$. Then the potential energy can be most efficiently evaluated by

$$\sum_{\substack{x_1, x_2, x_3: \\ y(x_1) < y(x_2) < y(x_3)}} \varphi_3\big(y(x_1), y(x_2), y(x_3)\big) + \varphi_3\big(y(x_1), y(x_3), y(x_2)\big)$$
$$+ \varphi_3\big(y(x_2), y(x_1), y(x_3)\big) + \varphi_3\big(y(x_2), y(x_3), y(x_1)\big)$$
$$+ \varphi_3\big(y(x_3), y(x_1), y(x_2)\big) + \varphi_3\big(y(x_3), y(x_2), y(x_1)\big). \tag{2.43}$$

This way, only one sixth of all triples have to be considered by the algorithm. Depending on the concrete potential, symmetries might be used to further reduce the number of evaluations of φ_3, similar to (2.42).

For the Stillinger-Weber potential however, the three-body terms $\varphi_3(y(x_1), y(x_2), y(x_3))$ vanish if $|y(x_1) - y(x_2)| \geq r_0$ or $|y(x_3) - y(x_2)| \geq r_0$. By the triangle inequality, we therefore know that φ_3 vanishes if $|y(x_1) - y(x_3)| \geq 2r_0$, but note that this need not hold for $|y(x_1) - y(x_3)| > r_0$ only. This behavior is typical for potentials which depend on the angle between $y(x_1) - y(x_2)$ and $y(x_3) - y(x_2)$. The technique described above to reduce the search for triples could be used for this type of potential as well, but the minimal cell size has to be doubled from r_0 to $2r_0$ to guarantee that all interactions are captured. This reduces the efficiency considerably.

However, there is a way to avoid this problem. The crucial point is not to restrict the search for triples $(y(x_1), y(x_2), y(x_3))$ to those with $y(x_1) < y(x_2) < y(x_3)$, but only to those with $y(x_1) < y(x_3)$. Using the symmetry $\varphi_3(y(x_1), y(x_2), y(x_3)) = \varphi_3(y(x_3), y(x_2), y(x_1))$, we obtain that the potential equals

$$2 \sum_{\substack{x_1, x_2, x_3: \\ y(x_1) < y(x_3)}} \varphi_3\big(y(x_1), y(x_2), y(x_3)\big). \tag{2.44}$$

This doubles the number of triples compared to (2.43). But in contrast to the technique above, it is now sufficient to consider only atoms $y(x_2)$ and $y(x_3)$ with $|y(x_2) - y(x_1)| \leq r_0$ and $|y(x_3) - y(x_2)| \leq r_0$. Hence the cutoff radius can be halved. Altogether, the number of triples to be handled is reduced by the factor $2^d \cdot 2^d / 2 = 2^{2d-1}$ then. For the physically relevant spatial dimension $d = 3$ we obtain a speedup factor of 32.

2.2.3 Numerical Analysis of Eigenmodes

As an example for the molecular dynamics simulation with the Stillinger-Weber potential, we investigate the dynamical behavior of a silicon bar. Because the main application in this thesis are shape memory alloys and because the Stillinger-Weber potential rather works as a prototype to measure the approximation properties of the inner expansion technique, we keep this application quite simple here.

For the simulation we have developed a molecular dynamics program. It is based on the linked-cell technique as described in Section 2.2.2 and can handle many different potentials.

$t = 0$ps

$t = 1.4$ps

$t = 2.2$ps

$t = 3.2$ps
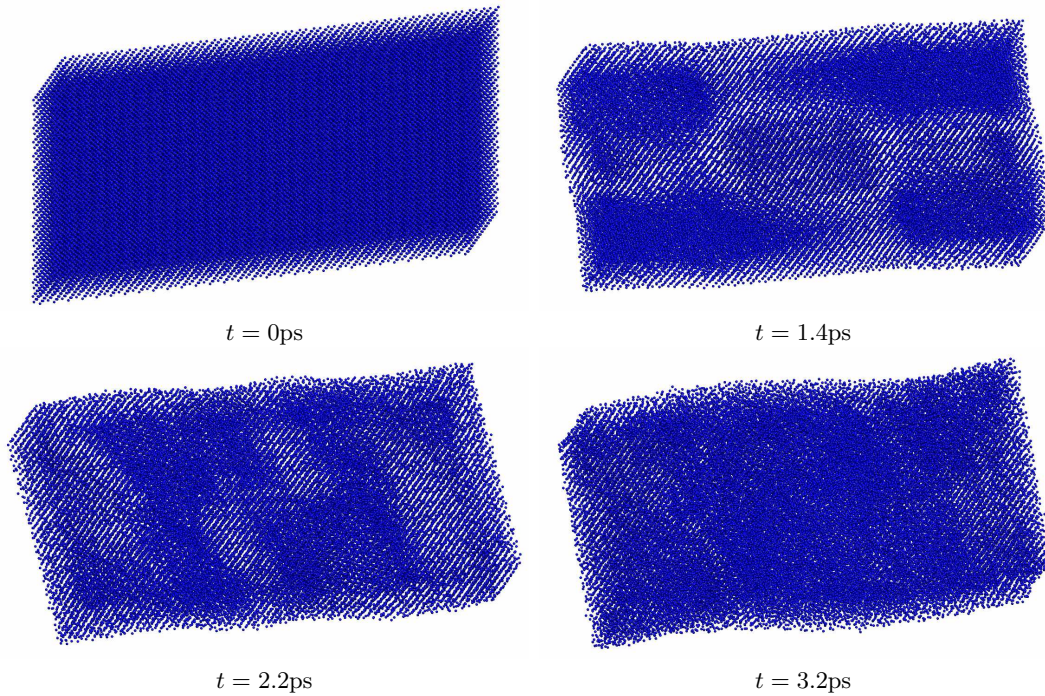
Figure 2.6: Snapshots of the molecular dynamics simulation of a silicon crystal with a sheared initial configuration.

In case of the Stillinger-Weber potential here, it exploits the special locality condition as described in Section 2.3.2 for an efficient computation. The evolution equations (2.20) are discretized in time by means of the leap-frog scheme. For the application here, the time-step is chosen as 1fs.

The initial condition is given by a bar of 55,800 silicon atoms arranged in form of the diamond lattice structure. The bar is additionally sheared by 15%. The molecular dynamics program is now used to calculate the behavior of this system. In Figure 2.6, snapshots of the solution are plotted for the time steps $t = 0$ps, $t = 1.4$ps, $t = 2.2$ps and $t = 3.2$ps. One can clearly see how the system relaxes from the stressed initial configuration and observe its eigenmodes.

2.3   Application to Shape Memory Alloys

As a second physically realistic example, we now come to the molecular dynamics simulation of shape memory alloys (SMA). Such alloys are characterized by their ability to undergo austenitic-martensitic phase transformations, which induce a change of their macroscopic shape. These transformations can be driven by temperature or external forces. Shape memory alloys belong to the class of so-called smart materials. They have a wide range of applications in engineering, nanotechnology and medicine.

There are many different alloys which exhibit the shape memory effects, such as nickel-titanium, copper-aluminum-nickel, nickel-aluminum, nickel-manganese-gallium, indium-thallium and others. For our simulation here, we choose nickel-aluminum as a prototype.

A suitable potential energy for the alloy is given by the Embedded-Atom Method (EAM). This is a semi-empirical method to describe the potential energy of metallic systems on the atomic level. It has been developed by Daw and Baskes [26, 27] and is now a widely used potential for molecular dynamics simulations of metals. It allows for a better description of the material properties than simple pair potentials. The Embedded-Atom Method has already been successfully used to model effects of crack propagation, fracture, surface energy and impurities in solid metallic systems and is even suitable for the liquid phase of such systems.

The EAM defines the potential energy in terms of the electron density, which is obtained by quantum mechanical calculations. This density is then used to empirically define the potential energy to fit certain physical properties.

The original EAM simplifies things by spherically averaging the electron density around the atoms to obtain radially symmetric functions of the distance. This simplification is avoided by the so-called Modified Embedded-Atom Method (MEAM) [14, 13] which takes angle-dependent electron densities into account.

Many parameter sets have been developed to describe different materials with the EAM or the MEAM. Let us note that among these there is also silicon [12]. Furthermore, Thijsse [75] has shown that the Stillinger-Weber potential for silicon is a special case of the MEAM. To this end, he constructed a set of MEAM parameters such that the Stillinger-Weber potential exactly coincides with the MEAM potential. Thus this section can be interpreted as an extension of Section 2.2. Nevertheless, it is not favorable to use this construction because of its computational overhead.

2.3.1   Embedded-Atom Method

The EAM is based on the hypothesis that every potential induces a certain electron density. Vice versa, it has been shown by Hohenberg and Kohn [46] that the electron density uniquely determines the potential. This principle is employed by the EAM to define the potential in terms of the electron density.

The basic concept is that every atom $x \in \mathcal{L} \cap \Omega$ is embedded in the set of surrounding atoms, the so-called host. We assume that the electron density ρ_x^{host} of the host is given by the superposition of the electron densities $\rho_{\tilde{x}}^{\text{atom}}$ of the single atoms $\tilde{x}$ in the host. The latter are presumed to be radially symmetric functions of the distance. They depend on the type of the atom and are quantified by single-determinant Hartree-Fock calculations, see [21]. Thus we write

$$\rho_x^{\text{host}} = \sum_{\tilde{x} \in \mathcal{L} \cap \Omega \setminus \{x\}} \rho_{\tilde{x}}^{\text{atom}}(|y(x) - y(\tilde{x})|). \tag{2.45}$$

Note that the respective atom x itself is not included. To be precise, only the electron densities of the outer orbitals are accounted for in the function $\rho_{\tilde{x}}^{\text{atom}}$, since only the valence electrons are relevant for the bonding and the outer behavior.

The embedding part Φ_x^{emb} of the potential energy for an atom x is now assumed to depend on the electron density ρ_x^{host} of the host:

$$\Phi_x^{\text{emb}} = \Phi_x^{\text{emb}}\big(\rho_x^{\text{host}}\big). \tag{2.46}$$

The embedding function Φ_x^{emb} is fitted to the material properties. Mostly a cubic spline function is used to resemble different material properties such as the lattice constants, the elastic moduli, the sublimation energy and the vacancy-formation energy. The concrete definition of Φ_x^{emb} used here is given in Appendix A.

The embedding part of the overall potential is then obtained by summing over all atoms:

$$\Phi^{\mathrm{emb}} = \sum_{x \in \mathcal{L} \cap \Omega} \Phi_x^{\mathrm{emb}} \left(\sum_{\tilde{x} \in \mathcal{L} \cap \Omega \setminus \{x\}} \rho_{\tilde{x}}^{\mathrm{atom}}(|y(x) - y(\tilde{x})|) \right). \qquad (2.47)$$

Note that Φ^{emb} is not a pair potential, because Φ_x^{emb} is in general nonlinear.

The embedding part by itself is not sufficient to describe the physical properties of the solid. Just as the elastic moduli of any pair potential fulfill the Cauchy relation $\mathbb{C}_{12} = \mathbb{C}_{44}$, the elastic moduli of the embedding energy fulfill the relations $\mathbb{C}_{44} = 0$ and $\mathbb{C}_{11} = \mathbb{C}_{12}$. They are often violated by measurements of real solids as well. But the combination of both a pair potential and the embedding part allows for an accurate description without these nonphysical symmetries. Therefore, we add an additional pair potential Φ^{pair} and obtain the total potential energy

$$\Phi^{(\mathrm{A})} = \Phi^{\mathrm{emb}} + \Phi^{\mathrm{pair}}. \qquad (2.48)$$

The pair potential is given by

$$\Phi^{\mathrm{pair}} = \frac{1}{2} \sum_{\substack{x, \tilde{x} \in \mathcal{L} \cap \Omega \\ x \neq \tilde{x}}} \Phi_{x,\tilde{x}}^{\mathrm{pair}}(|y(x) - y(\tilde{x})|) \qquad (2.49)$$

where

$$\Phi_{x,\tilde{x}}^{\mathrm{pair}}(r) = \frac{1}{4\pi\varepsilon_0} \frac{Z_x(r) Z_{\tilde{x}}(r)}{r}. \qquad (2.50)$$

The functions Z_x and $Z_{\tilde{x}}$ depend on the type of the atom x or $\tilde{x}$, respectively, and are specified for the concrete material in Appendix A. They can be interpreted as effective charges. As they vanish for distances of more than a few Å, the pair potential describes a localized or screened Coulomb potential.[4]

2.3.2   Exploitation of Locality for the Implementation

Since the EAM potential is local, there is hope to exploit this structure for an efficient implementation. But the linked-cell technique cannot be applied directly to the EAM potential, because the embedding part involves the general multi-body interaction of an a priori unbounded number of atoms. This makes up a fundamental difference to the two-body and three-body interactions of the Stillinger-Weber potential. In this section we show how the linked-cell technique as described in Section 2.2.2 can nevertheless be adapted to this setting.

---

[4]The electrostatic pair interaction (2.49) of the EAM potential contains the usual factor $\frac{1}{4\pi\varepsilon_0}$, where $e_0 = 8.8541878 \cdot 10^{-12}$ C^2/Jm denotes the permittivity of the vacuum. Note that this factor is omitted by many authors, because $4\pi\varepsilon_0$ reduces to the dimensionless constant 1 if the CGS unit system instead of the SI system is used.

For the embedding part $\Phi^{\mathrm{emb}} = \sum_x \Phi_x^{\mathrm{emb}}(\rho_x^{\mathrm{host}})$, the trick is to split up the computation into the determination of the electron density ρ_x^{host} of the host and the determination of the embedding energy. The first job can be done within a standard linked-cell cycle. For the latter we append an additional loop over all atoms x, called post-iteration, in which ρ_x^{host} is applied to the embedding function to evaluate $\Phi_x^{\mathrm{emb}}(\rho_x^{\mathrm{host}})$.

Furthermore, we do not only need to compute the potential itself for the molecular dynamics simulation, but also its first derivatives with respect to the particle positions. They read as

$$\nabla_{y(x)}\Phi^{(A)} = \sum_{\tilde{x}\in\mathcal{L}\cap\Omega\setminus\{x\}} \left(\Phi_x^{\mathrm{emb}\prime}(\rho_x^{\mathrm{host}})\cdot\rho_{\tilde{x}}^{\mathrm{atom}\prime} + \Phi_{\tilde{x}}^{\mathrm{emb}\prime}(\rho_{\tilde{x}}^{\mathrm{host}})\cdot\rho_x^{\mathrm{atom}\prime} \right. $$
$$\left. + \frac{(Z_x' Z_{\tilde{x}} + Z_x Z_{\tilde{x}}')|y(x)-y(\tilde{x})| - Z_x Z_{\tilde{x}}}{|y(x)-y(\tilde{x})|^2} \right) \frac{y(x)-y(\tilde{x})}{|y(x)-y(\tilde{x})|} \quad (2.51)$$

for all $x \in \mathcal{L}\cap\Omega$. Obviously the first derivative includes the sum $\Phi_x^{\mathrm{emb}\prime}\rho_{\tilde{x}}^{\mathrm{atom}\prime} + \Phi_{\tilde{x}}^{\mathrm{emb}\prime}\rho_x^{\mathrm{atom}\prime}$. This looks like a pair sum, but actually it is not, since $\Phi_{x/\tilde{x}}^{\mathrm{emb}\prime}$ depends on $\rho_{x/\tilde{x}}^{\mathrm{host}}$ as given by (2.45), which involves an additional sum over all particles and is not yet known during the pair loop. Just like above, this can be fixed by computing ρ_x^{host} and its derivative $\rho_x^{\mathrm{host}\prime}$ in a first linked-cell loop and then evaluating Φ_x^{emb} and $\nabla_{y(x)}\Phi_x^{\mathrm{emb}}$ in a second linked-cell loop.

The pair interaction Φ^{pair} and its derivative $\nabla_{y(x)}\Phi^{\mathrm{pair}}$ can be evaluated in a straightforward manner within a standard linked-cell cycle, as one can see from (2.51). The overall procedure thus reads as follows.

> First loop over all $x, \tilde{x}$ with linked-cell technique:
>> Add up pair part: Φ^{pair} and $\nabla_{y(x)}\Phi^{\mathrm{pair}}$
>> Add up electron density ρ_x^{host} and its derivative $\rho_x^{\mathrm{host}\prime}$
> Second loop over all $x, \tilde{x}$ with linked-cell technique:
>> Add up $\nabla_{y(x)}\Phi^{\mathrm{pair}}$ by using the previously computed
>> electron density ρ_x^{host} and $\rho_x^{\mathrm{host}\prime}$
> Post iteration loop over all x:
>> Compute embedding energy $\Phi_x^{\mathrm{emb}}(\rho_x^{\mathrm{host}})$

The post iteration trivially has the complexity $\mathcal{O}(N)$ and is therefore harmless. Thus the linked-cell technique allows the computation of the EAM potential and its derivatives with complexity $\mathcal{O}(N)$.

2.3.3 Numerical Analysis of Phase Transformations

Now we employ the EAM potential to simulate a nanoparticle which consists of a $\mathrm{Ni}_{64}\mathrm{Al}_{36}$ shape memory alloy on the atomic level. The concrete material parameters for the potential are given in Appendix A.

For the numerical simulation, the same molecular dynamics program is used as for the simulation of the silicon crystal in Section 2.2.3. It makes use of the scheme described in
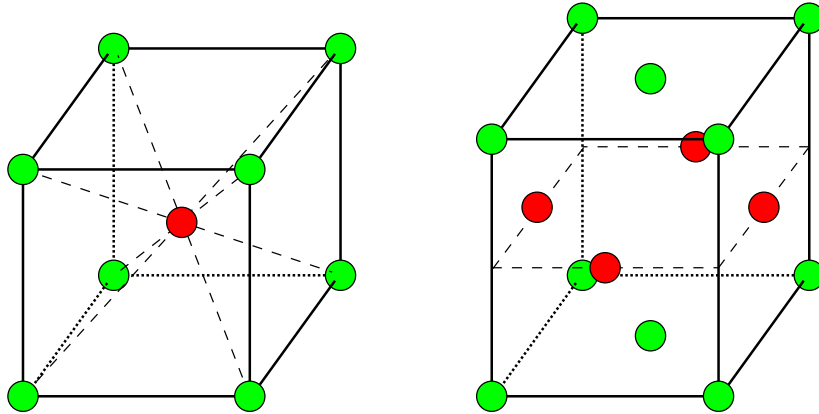
Figure 2.7: B2 (left) and L1$_0$ (right) lattice structures. The color indicates the two different types of atoms. Disregarding the atom types, the left lattice is body-centered cubic (bcc), and the right lattice is face-centered tetragonal (fct).

Section 2.3.2 to compute the EAM potential and its derivatives in an efficient way by the linked-cell technique. Just as before, the time-step is set to 1fs.

A ball of 2474 atoms is chosen as the reference configuration. The reference configuration is also taken as the initial configuration. The initial velocities of the atoms are chosen randomly to realize the initial temperature of 800K.

The lattice structure of the specimen is given by the so-called B2 lattice.[5] Disregarding the type of the atoms, this lattice has the body-centered cubic (bcc) structure. It is composed of two staggered cubic sublattices. One of these sublattices consists of nickel atoms and the other sublattice is randomly occupied by nickel and aluminum atoms, such that the overall composition of 64% nickel atoms and 36% aluminum atoms is reached. In our notation (2.1), it is given by

$$\mathcal{L}_{\text{cell}} = \frac{a_0}{2} \left\{ \begin{pmatrix} 0 \\ 0 \\ 0 \end{pmatrix}, \begin{pmatrix} 1 \\ 1 \\ 1 \end{pmatrix} \right\} \tag{2.52}$$

and $A = a_0 I$, where I denotes the identity matrix and $a_0 = 3\text{Å}$ is the lattice constant. The structure is depicted in Figure 2.7 left.

The simulation has been run for 7ps. Additionally the system is subjected to a cooling process from 800K to 100K during the simulation. To this end, the Berendsen thermostat [15] has been employed.

Figure 2.8 shows four snapshots of the solution. The nickel atoms are plotted in blue and the aluminum atoms in green. In the initial configuration (upper left snapshot), the B2 lattice structure can be clearly recognized. Shortly after the beginning of the simulation, the atoms undergo a slight perturbation due to thermal fluctuations, but the macroscopic

---

[5]We do not give an extensive survey of lattice classifications here, see e.g. [32], [16] and [61] for more information on this topic. Let us just mention that the set of so-called simple lattices, i.e. those which can be written with $|\mathcal{L}_{\text{cell}}| = 1$ in our notation, can be classified into 14 classes of so-called Bravais lattices in three space-dimensions. The so-called multilattices with $|\mathcal{L}_{\text{cell}}| > 1$ can additionally take different types of atoms into account. There is a huge amount of different classes of multilattices, one of them is the B2 lattice structure.

$t = 0\text{ps}, \vartheta = 800\text{K}$ $t = 0.5\text{ps}, \vartheta = 750\text{K}$

$t = 2\text{ps}, \vartheta = 600\text{K}$ $t = 7\text{ps}, \vartheta = 100\text{K}$
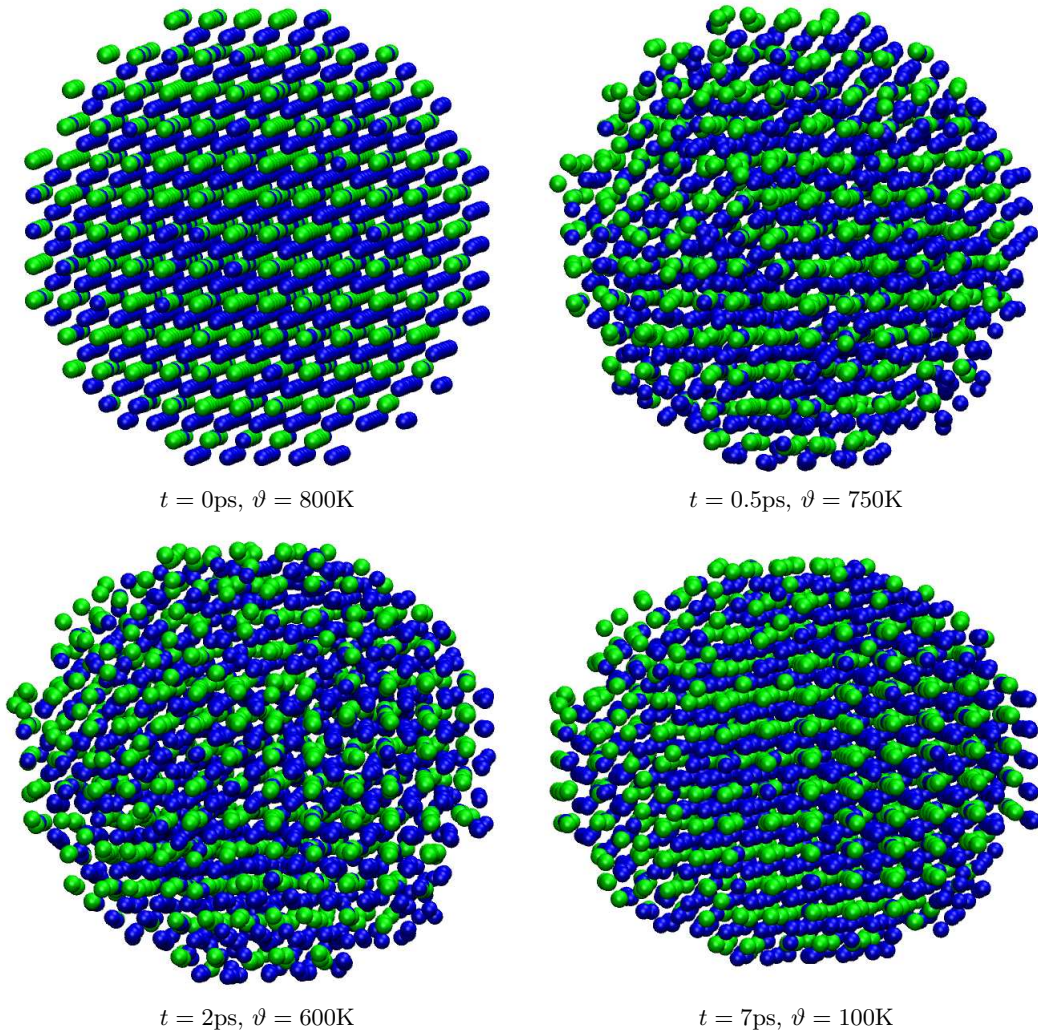
Figure 2.8: Snapshots of the molecular dynamics simulation of a $\text{Ni}_{64}\text{Al}_{36}$ nanoparticle with 2474 atoms.

shape of the specimen remains a ball (upper right snapshot). However, as the simulation proceeds, one can observe that the initial ball is deformed to an ellipsoid (both lower snapshots). It has been elongated along one axis (the x-axis in the figure), whereas it has been compressed along the other two axes.

The reason for this deformation can be found in the underlying lattice structure. To analyze it, we look at the radial distribution diagrams. In such a diagram, the density distribution of the distances of all atom pairs in the system is plotted, see e.g. [49]. Sometimes, this function is also called the pair correlation function. Since the radial distribution function exhibits a specific set of distinct maxima for each lattice type, it can be used to identify the lattice structure of the atomistic system.

In Figure 2.9, the radial distribution diagram for our simulation is plotted. The red curve corresponds to the initial configuration at 800K. It shows clear peaks at $\sqrt{3/4}\,a_0 \approx$ 2.6Å, $a_0 = 3$Å, $\sqrt{2}\,a_0 \approx 4.24$Å and so forth. (Recall that $a_0 = 3$ Å denotes the lattice
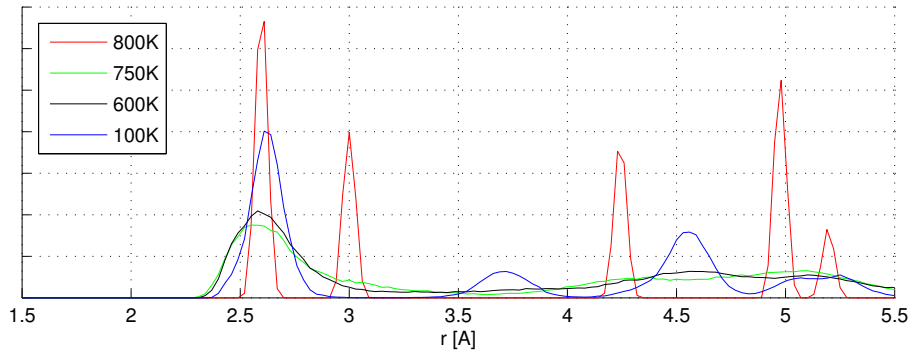
Figure 2.9: Radial distribution diagram of $Ni_{64}Al_{36}$ nanoparticle with 2474 atoms.

constant.) This is the typical shape for a body-centered cubic (bcc) lattice. As the simulation proceeds, the peaks widen up due to thermal fluctuations. It can be read off the green plot that the system at 750K is still close to the bcc structure. But then, the positions of the maxima change (black line for 600K), and finally the radial distribution function attains its maxima at a different set of distances (blue line for 100K), namely at 2.65Å, 3.7Å, 4.55Å and so forth. This corresponds to a face-centered tetragonal (fct) lattice, see Figure 2.7 right. If we additionally take the type of the atoms into account, this structure is called a $L1_0$ lattice.

The transformation from the B2 to the $L1_0$ lattice can be explained as follows. We start with a B2 lattice, see Figure 2.10 left. It can be regarded as a cubic sublattice (green atoms), where an additional atom, drawn in red, is placed in the center of each cubic unit cell. Within this B2 lattice, we choose a cell which is rotated by 45 degrees around the x_3-axis, and whose corner points coincide with atoms of the original cubic sublattice. This cell is depicted in blue in Figure 2.10. Note that now an additional atom is situated in the center of each face of this new cell, instead of the center of each old base cell. To be precise, a green atom lies in the center of the top and the bottom face, and a red one in the center of the other four faces. This structure coincides with the structure of the $L1_0$ lattice, except for the lengths of the edges, compare to Figure 2.7 right. To compensate for this discrepancy, the lengths can be rescaled. The x_1-axis and the x_2 axes are slightly compressed, whereas the x_3-axis is elongated, see Figure 2.10 right. Now we end up with a rotated, but correct $L1_0$ lattice. It is important to note that the involved rescaling is not a local rearrangement of atoms, but a macroscopically uniform deformation. The rescaling is exactly the deformation we observed in our simulation. Note that the scaling could have been equivalently performed in direction of the other two axes to transform the B2 lattice into the $L1_0$ lattice.

All in all, the system underwent a so-called structural phase transformation. Due to the change of the temperature, the initial bcc/B2 lattice structure changed into the fct/$L1_0$ structure. The high-temperature phase is called the austenitic phase, while the low-temperature phase is denoted the martensitic phase. Therefore we speak of an austenitic-martensitic phase transformation. This transformation entails a macroscopically uniform movement of the atoms, which caused the change of the macroscopic shape from the ball to an ellipsoid.
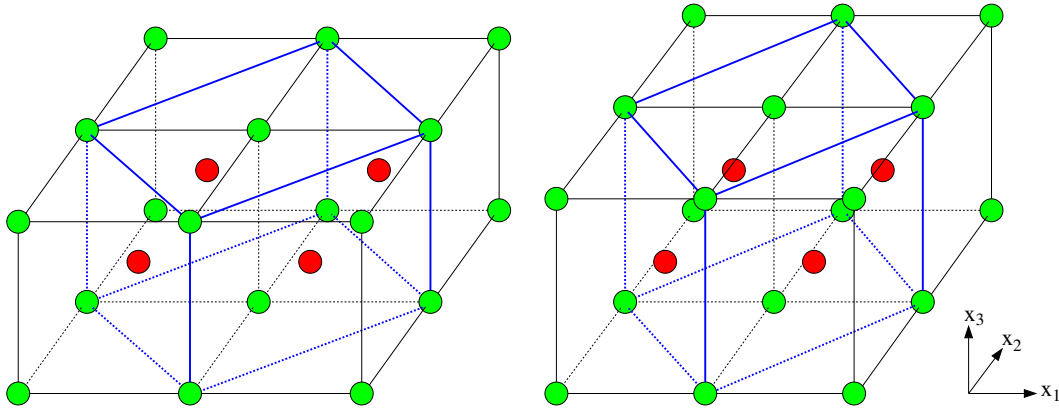
Figure 2.10: Transformation of the B2 lattice to the $L1_0$ lattice. First a rotated base cell of the $L1_0$ lattice is chosen within the B2 lattice (left). Then the correct aspect ratio of the $L1_0$ lattice is achieved by scaling along the axes (right).

The same transformation can be undergone in reverse direction, from the martensitic phase to the austenitic phase. In this case, the original shape is recovered. This is the reason why such materials are called shape memory alloys. We will describe this effect and how it can be exploited for applications in Section 4.4.

Kastner [50] has shown that such structural phase transitions can already be observed for a simple Lennard-Jones model with two different types of atoms. However, this is merely a model problem only for the phase transition and does not resemble any other material properties.

Now we come to the simulation of a larger nanoparticle consisting of 19686 atoms. All other simulation parameters are the same as above. Figure 2.11 shows the snapshots of the simulation. But in contrast to the simulation of the small nanoparticle, we do not observe the clear transformation of the ball to an ellipsoid. Instead, the final nanoparticle roughly remains a ball and only exhibits a slightly irregular macroscopic perturbation. However, the according radial distribution diagrams shown in Figure 2.12 reveal that the same transformation as before must have taken place. This first sounds like a contradiction, but actually it is not. In the larger simulation, the transformation proceeded locally, and the change of shape went into different directions in different regions of the specimen. These regions can be recognized in the lower right snapshot in form of several patches of a regular lattice structure at the surface of the nanoparticle. Each such region corresponds to a so-called martensitic variant. Macroscopically, these transformations average out, such that the overall shape roughly remains. This is the principle of the so-called microstructure which is a typical phenomena of shape memory alloys in the martensitic phase.

However, the large nanoparticle is still much too small to simulate a real crystal. Real alloys consist of a number of atoms which is far out of reach for any molecular dynamics simulation up to now. The examples here already show some typical and important effects, but there is clearly a need for simulations on a larger length scale. Since this is impossible on the atomic level, we have to pass to another level. This leads us to the next chapter, where the upscaling of the atomistic system to the continuum mechanical level will be discussed.
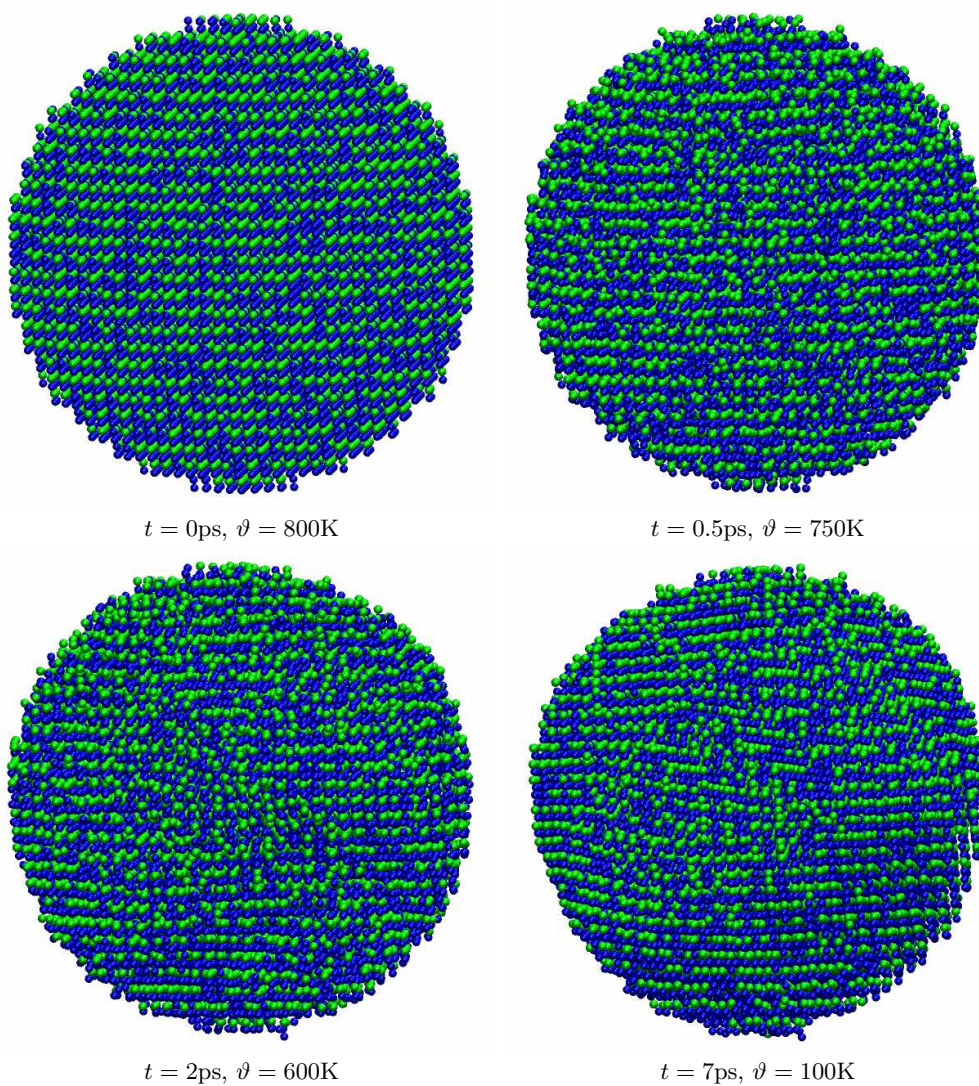
Figure 2.11: Snapshots of the molecular dynamics simulation of a $Ni_{64}Al_{36}$ nanoparticle with 19686 atoms.
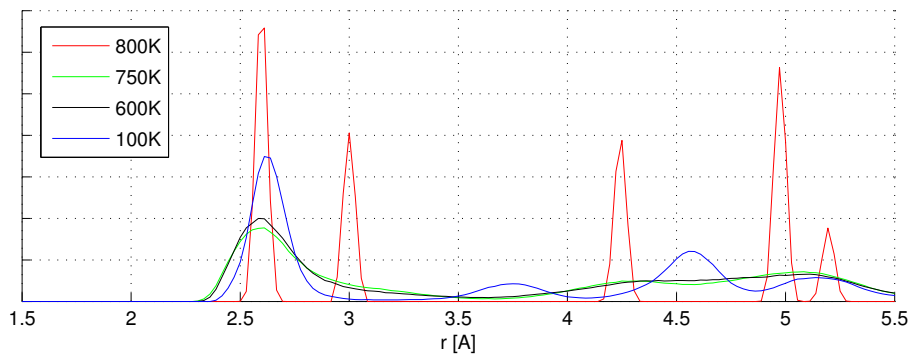
Figure 2.12: Radial distribution diagram of the $Ni_{64}Al_{36}$ nanoparticle with 19686 atoms.

Chapter 3

Upscaling to the Continuum Mechanical Level

In the former chapter, we saw how crystalline solids and other materials can be described by means of atomistic models and how their behavior can be simulated with the method of molecular dynamics. However, only quite small systems can be numerically investigated this way due to computational limits. Realistic systems consist of an extremely large number of atoms, which prevents a numerical treatment. Thus techniques to overcome this problem have to be developed.

The main principle we follow here is to describe the specimen on a larger length scale. To this end, other models than atomistic models are needed. The most common type of models are continuum mechanical models, in which the discrete set of atom positions is replaced by an entire domain $\Omega \subset \mathbb{R}^d$, i.e. by an infinite set. This resembles a "large" number of atoms and at the same time allows for some kind of averaged formulation. The deformation is then described by a continuous function $y : \Omega \to \mathbb{R}^d$. The atomic length scale is often called the microscale, whereas the continuum mechanical length scale is denoted the macroscale.

The continuum mechanical model should of course resemble the properties of the atomistic model as closely as possible. One way to achieve this is to define the continuum mechanical model phenomenologically, i.e. to define the model in such a way that it resembles the material properties which are observed by real experiments. But then the relationship to the atomistic model is unclear. A better way is to strictly derive the continuum mechanical model from the atomistic model. This process is called *upscaling* and depicts the way we follow in this work. The main goal of this chapter is to develop an upscaling technique and to analyze to what extent the resulting continuum models fit with the original atomistic model.

One advantage of the continuum mechanical model is that it allows for a more efficient computation. One is often interested in averaged quantities only, whereas the exact trajectories of all single atoms do not play an important role. To this end, it suffices not to resolve all atoms individually. A continuum mechanical model together with the according numerical techniques can make such an averaging process possible. Another advantage of the continuum model is that it is accessible to analytical techniques, including the powerful differential calculus and the calculus of variations. This allows to further investigate

existence, uniqueness, well-posedness and other qualitative and quantitative properties of solutions.

Here we propose the so-called inner expansion technique [6, 5] to perform the upscaling process. This approach gives a description of the atomistic system within the quasi-continuum regime. It is based on a Taylor series approximation of the deformation function y and captures all higher order terms up to a given order. The continuum model also reflects the discreteness effects of the underlying atomistic system. This may sound paradox, but turns out to be important for an accurate description of the atomistic system. Also, the underlying physical length scale of the atomistic system is preserved this way. Furthermore, the inner expansion technique conserves important properties from the microscale such as convexity of the potential and therefore leads to well-posed evolution equations.

This chapter is organized as follows. First, we describe the inner expansion technique in Section 3.1. In Section 3.2 we apply the technique to the three model problems defined in Section 2.1.2. Furthermore, the properties of the resulting continuum mechanical models are studied by means of a numerical comparison with the underlying atomistic system. This way we analyze to what extent the atomistic model is approximated. Then, in Section 3.3, we analytically show that the inner expansion technique carries over several important properties from the microscale to the macroscale. In Section 3.4, the inner expansion technique is compared to other upscaling schemes, namely the scaling technique and the direct expansion technique. Finally, the inner expansion technique is applied to the physically meaningful example of crystalline silicon as introduced in Section 2.2.

3.1 Inner Expansion Technique

A continuum mechanical model is based on the description of the deformation in terms of a deformation function $y : \Omega \to \mathbb{R}^d$, i.e. a function which maps the reference configuration in form of a complete domain $\Omega \subset \mathbb{R}^d$ to $\mathbb{R}^d$. This stands in contrast to the atomic level, where the deformation is described by a function $y : \Omega \cap \mathcal{L} \to \mathbb{R}^d$, which only maps the discrete set $\Omega \cap \mathcal{L}$ to $\mathbb{R}^d$.

In order to define the continuum mechanical model, the task is now to assign a potential energy to a continuum deformation function $y : \Omega \to \mathbb{R}^d$. This will be done in the next section by a suitable reduction to the underlying atomistic potential.

3.1.1 Inner Expansion

In (2.5) we introduced the points $\overline{x} \in \overline{\mathcal{L}} \cap \Omega$ to localize the overall potential energy $\Phi^{(\mathrm{A})}$ by means of the sum $\sum_{\overline{x} \in \overline{\mathcal{L}} \cap \Omega} \Phi^{(\mathrm{A}),\overline{x}}$. For each point $\overline{x}$, we now consider the Taylor series expansion of the deformation function y around $\overline{x}$ up to some degree $K \in \mathbb{N}$:

$$y(x) \approx \sum_{k=0}^{K} \frac{1}{k!} \nabla^k y(\overline{x}) : (x - \overline{x})^k. \tag{3.1}$$

Here the colon denotes the higher-dimensional scalar product. The expansion (3.1) then allows us to reformulate the local potential $\Phi^{(A),\overline{x}}$ from (2.5) in the following way:

$$\Phi^{(A),\overline{x}}(\{y(x)\}_{x\in\mathcal{L}\cap\Omega}) \approx \Phi^{(A),\overline{x}}\left(\left\{\sum_{k=0}^{K}\frac{1}{k!}\nabla^k y(\overline{x}) : (x-\overline{x})^k\right\}_{x\in\mathcal{L}\cap\Omega}\right)$$

$$= \Phi^{(I),\overline{x}}\left(y(\overline{x}), \nabla y(\overline{x}), \nabla^2 y(\overline{x}), \ldots, \nabla^K y(\overline{x})\right), \qquad (3.2)$$

where $\Phi^{(I),\overline{x}}$ is defined by

$$\Phi^{(I),\overline{x}}(d_0, d_1, d_2, \ldots, d_K) := \Phi^{(A),\overline{x}}\left(\left\{\sum_{k=0}^{K}\frac{1}{k!}d_k : (x-\overline{x})^k\right\}_{x\in\mathcal{L}\cap\Omega}\right). \qquad (3.3)$$

Thus we transformed the original potential $\Phi^{(A),\overline{x}}$ which depends on the deformation y at all lattice points $x \in \mathcal{L}\cap\Omega$ to a representation which depends on the derivatives of y only at the single point $\overline{x}$.[1]

Summing up the local potentials $\Phi^{(I),\overline{x}}$, we obtain the overall potential

$$\Phi^{(I)}(y) = \sum_{\overline{x}\in\overline{\mathcal{L}}\cap\Omega} \Phi^{(I),\overline{x}}\left(y(\overline{x}), \nabla y(\overline{x}), \nabla^2 y(\overline{x}), \ldots, \nabla^K y(\overline{x})\right). \qquad (3.4)$$

Note that we implicitly assume a certain link between the microscale and the macroscale in the above construction, namely that the microscopic atoms exactly follow the macroscopic deformation. Thus, both scales are related to each other by the identity function. This link is the most natural one, but by far not the only possible one. Additionally, it is possible to consider additional local fluctuations which allow the atoms to further relax. This corresponds to the introduction of a mesoscopic length scale, which is situated between the microscale and the macroscale. This approach is followed by the concept of the Γ-limit [18]. For the link between the microscale and the macroscale, see also the discussion in [17].

Let us furthermore note that for the approximation degree $K = 1$, our approach coincides with the well-known Cauchy-Born hypothesis [33]. For $K \geq 2$, it may be regarded as a generalization.

3.1.2 Spatial Averaging

The potential energy $\Phi^{(I)}$ in representation (3.4) still contains the finite sum over all expansion points $\overline{x} \in \overline{\mathcal{L}}\cap\Omega$. This is in contrast to common continuum mechanical energies in which an energy density is integrated over the reference configuration Ω. The sum will now be approximated.

In the first instance we assume that the boundary effects do not play any substantial role. This is reasonable if the potential is of short range or rapidly decaying like the Lennard-Jones potential. Because of the periodic structure of the lattice $\overline{\mathcal{L}}$, the potential then inherits the translational invariance

$$\Phi^{(I),\overline{x}} \equiv \Phi^{(I),\overline{x}+\overline{A}z} \qquad (3.5)$$

---

[1] A similar construction will later be used in (3.64) in Section 3.4.1.3 to explain the behavior of the scaling technique.

for all $\overline{x} \in \overline{\mathcal{L}}_{\text{cell}}$ and $z \in \mathbb{Z}^d$. As a consequence, we can split the sum over all $\overline{x} \in \overline{\mathcal{L}} \cap \Omega$ in the definition of $\Phi^{(\text{I})}$ as follows:

$$
\begin{aligned}
\Phi^{(\text{I})}(y) &= \sum_{\overline{x} \in \overline{\mathcal{L}} \cap \Omega} \Phi^{(\text{I}),\overline{x}} \left(y(\overline{x}), \nabla y(\overline{x}), \nabla^2 y(\overline{x}), \ldots, \nabla^K y(\overline{x}) \right) \\
&= \sum_{\overline{x} \in \overline{\mathcal{L}}_{\text{cell}}} \sum_{\substack{z \in \mathbb{Z}^d: \\ \overline{x} + \overline{A}z \in \Omega}} \Phi^{(\text{I}),\overline{x}} \left(y(\overline{x} + \overline{A}z), \nabla y(\overline{x} + \overline{A}z), \nabla^2 y(\overline{x} + \overline{A}z), \ldots, \nabla^K y(\overline{x} + \overline{A}z) \right).
\end{aligned}
$$

$$(3.6)$$

Observe that the sum over all z in (3.6) acts as a Riemann sum. Especially if the number of base cells is large, the expression is close to an integral. Thus it is justified to interpolate $\Phi^{(\text{I})}(y)$ by passing to the integral representation

$$
\begin{aligned}
\Phi^{(\text{J})}(y) &:= \sum_{\overline{x} \in \overline{\mathcal{L}}_{\text{cell}}} \frac{1}{|\det \overline{A}|} \int_\Omega \Phi^{(\text{I}),\overline{x}} \left(y(x), \nabla y(x), \nabla^2 y(x), \ldots, \nabla^K y(x) \right) \, \mathrm{d}x \\
&= \int_\Omega \Phi^{(\text{J}),x} \left(y(x), \nabla y(x), \nabla^2 y(x), \ldots, \nabla^K y(x) \right) \, \mathrm{d}x,
\end{aligned}
$$

$$(3.7)$$

where the continuum energy density $\Phi^{(\text{J}),x}$ is defined by

$$
\Phi^{(\text{J}),x}(d_0, d_1, \ldots, d_K) := \frac{1}{|\det \overline{A}|} \sum_{\overline{x} \in \overline{\mathcal{L}}_{\text{cell}}} \Phi^{(\text{I}),\overline{x}}(d_0, d_1, \ldots, d_K).
$$

$$(3.8)$$

The factor $\frac{1}{|\det \overline{A}|}$ stems from the volume of the base cell of the lattice $\overline{\mathcal{L}}$, compare to its definition (2.6).

Note that since $\Phi^{(\text{I}),\overline{x}}$ does not depend on z, the interpolation takes place only in the deformation function y, not in Φ. But let us remark that it is also possible to carry out the spatial averaging procedure without neglecting the boundary effects. In this case, the relation (3.5) does not necessarily hold. Then an additional interpolation between the functions $\Phi^{(\text{I}),\overline{x}+Az}$ for different $z \in \mathbb{R}^d$ is needed. Consequently, the interpolated energy density $\Phi^{(\text{J}),x}$ is no longer homogeneous in space, but depends on x. Thus the index x is really necessary. The additional interpolation can be done in various ways, ranging from a piecewise constant interpolation to arbitrary smooth interpolations. But since we do not need this here, this will not be discussed in detail.

Note furthermore that there is in general no reason that some kind of translational invariance like $\Phi^{(\text{I}),\overline{x}_1} = \Phi^{(\text{I}),\overline{x}_2}$ holds for two different points $\overline{x}_1, \overline{x}_2 \in \overline{\mathcal{L}}_{\text{cell}}$, similar to (3.5). The Lennard-Jones potential, which will be discussed later in Section 3.2.2, is an example where such an invariance fails. Thus the sum over all $\overline{x}$ from the base cell $\overline{\mathcal{L}}_{\text{cell}}$ cannot be averaged in the same way as the sum over z.

Here, the following remark is in order: Other upscaling techniques such as the scaling technique which will be discussed in Section 3.4.1 are based on the thermodynamic limit, which drives the number N of atoms to infinity. In this case the limiting procedure $N \to \infty$ includes the limit of the Riemann sum and an integral representation is directly obtained. For the inner expansion technique, however, the number N of atoms is kept fixed. The passage from the Riemann sum to the integral representation (3.7) is now an

additional approximation step which does not correspond to the process of letting the number N of atoms tend to infinity. The result is not a description for the continuum limit, but an interpolated description for the system with a fixed number of atoms in the quasi-continuum regime, which still contains the discreteness effects of the finite system.

3.1.3 Choice of the Expansion Points

Now we consider the choice of the expansion points $\overline{x}$ in more detail. In order to make the truncated Taylor series approximation as accurate as possible, the remainder terms must be minimized. The latter strongly depend on the choice of the expansion points, hence it is crucial to choose them correctly.

The optimal choice can be strictly given in the important special case when the local potential $\Phi^{(A),\overline{x}}$ depends on a linear combination of all components of all points $y(x)$. This means that the local potential can be written as

$$\Phi^{(A),\overline{x}}(\{y(x)\}_{x \in \mathcal{L} \cap \Omega}) = \varphi\left(\sum_{x \in \mathcal{L} \cap \Omega} a_x \cdot y(x)\right), \tag{3.9}$$

where $\varphi : \mathbb{R} \to \mathbb{R}$ is an arbitrary function and $a_x \in \mathbb{R}^d$ are constants for all $x \in \mathcal{L} \cap \Omega$. For the sake of a simple description, we proceed with $d = 1$. Similar arguments hold for higher space dimensions. Because of the crystal symmetry, we can assume that the absolute values of the coefficients a_x satisfy the symmetry relation $|a_x| = |a_{2c-x}|$ for a center point $c \in \Omega$ such that $\mathcal{L} = 2c - \mathcal{L}$. The center point c can be characterized as the barycenter

$$c = \frac{\sum_{x \in \mathcal{L} \cap \Omega} |a_x| x}{\sum_{x \in \mathcal{L} \cap \Omega} |a_x|}. \tag{3.10}$$

The Taylor expansion of the potential $\Phi^{(A),\overline{x}}$ from (3.9) around $\overline{x}$ then reads as

$$\varphi\left(\sum_{x \in \mathcal{L} \cap \Omega} a_x y(x)\right) = \varphi\left(\sum_{x \in \mathcal{L} \cap \Omega} \sum_{k=0}^{K} \frac{a_x}{k!} y^{(k)}(\overline{x})(x - \overline{x})^k\right.$$
$$\left. + \frac{a_x}{(K+1)!} y^{(K+1)}(\xi_x)(x - \overline{x})^{K+1}\right) \tag{3.11}$$

for some points $\xi_x \in \Omega$. Since a priori nothing is known about the behavior of $y^{(K+1)}$, the best way is to minimize the simplified remainder term

$$R(\overline{x}) := \sum_{x \in \mathcal{L} \cap \Omega} |a_x| |x - \overline{x}|^{K+1}. \tag{3.12}$$

Lemma 3.1 *The simplified remainder term (3.12) attains its minimum at the barycenter c.*

PROOF Since the function $\overline{x} \mapsto |x - \overline{x}|^{K+1}$ is convex, we can bound $R(\overline{x})$ from below by

$$R(\overline{x}) \geq \sum_{x \in \mathcal{L} \cap \Omega} |a_x| \left(\left.\frac{\partial |x - \overline{x}|^{K+1}}{\partial \overline{x}}\right|_{\overline{x}=c} (\overline{x} - c) + |x - c|^{K+1}\right)$$
$$= \sum_{x \in \mathcal{L} \cap \Omega} |a_x| |x - c|^{K+1} = R(c). \tag{3.13}$$

Here, due to symmetry, the relation $\frac{\partial |x-\overline{x}|^{K+1}}{\partial \overline{x}}\big|_{\overline{x}=c} = -\frac{\partial |2c-x-\overline{x}|^{K+1}}{\partial \overline{x}}\big|_{\overline{x}=c}$ holds and the differential terms $\frac{\partial |x-\overline{x}|^{K+1}}{\partial \overline{x}}$ disappear in the above sum. $\qquad\square$

Hence each point $\overline{x}$ should be chosen as the barycenter c of the local interaction potential. The set $\overline{\mathcal{L}} \cap \Omega$ is thus constructed by splitting the overall potential $\Phi^{(A)}$ into as many local interactions as possible. For each local interaction the barycenter c is computed according to (3.10) and its value is assigned to the variable $\overline{x}$. The set of all such barycenters c then forms the set $\overline{\mathcal{L}} \cap \Omega$.

In the case of a more general potential which cannot be written as (3.9), many remainder terms occur and are combined in a complex manner. Their interaction can be very complicated and depends strongly on the type of the potential. It is unclear what the minimization of the remainder terms in this case means. An individual analysis is necessary for each such type of potential. Furthermore, the barycenter c of the local interaction cannot be strictly defined due to the missing coefficients a_x. Nevertheless, in many cases it is possible to define some generalized barycenter. From our experience it is best to choose $\overline{x}$ as such a center point.

3.1.4   Evolution Equations

For the atomistic system, the evolution equation is given by Newton's second law of motion (2.20)

$$m(x)y_{tt}(x) = -\nabla_{y(x)}\Phi^{(A)}(\{y(\tilde{x})\}_{\tilde{x}\in\mathcal{L}\cap\Omega}) \tag{3.14}$$

as described in Section 2.1.3. Recall that $m(x)$ denotes the mass of the atom $y(x)$. On the continuum mechanical level, Newton's law reads as

$$\int_{\Omega} \rho \frac{\partial^2 y}{\partial t^2} v \, \mathrm{d}x = -\Phi^{(J)'}(y; v) \tag{3.15}$$

for all test functions $v \in C_c^\infty(\Omega)$, where $\Phi^{(J)'}(y; v)$ denotes the derivative of the continuum potential $\Phi^{(J)}$ at y in the direction v and where

$$\rho = \frac{1}{|\det A|} \sum_{x\in\mathcal{L}_{\text{cell}}} m(x) \tag{3.16}$$

denotes the mass density. From the inner expansion technique, we obtain the continuum mechanical potential (3.7). We substitute this form into (3.15) and yield

$$\int_{\Omega} \rho \frac{\partial^2 y}{\partial t^2} v \, \mathrm{d}x = -\Phi^{(J)'}(y; v) = -\int_{\Omega} \sum_{k=0}^{K} \Phi_{,k}^{(J),x}(y, \nabla y, \dots, \nabla^K y) : \nabla^k v \, \mathrm{d}x$$

$$= -\int_{\Omega} \sum_{k=0}^{K} (-1)^k \operatorname{div}^k \Phi_{,k}^{(J),x}(y, \nabla y, \dots, \nabla^K y) v \, \mathrm{d}x, \tag{3.17}$$

where $\Phi_{,k}^{(J),x}$ denotes the derivative of $\Phi^{(J),x}$ with respect to the argument $\nabla^k y$. Since this holds for all test functions $v \in C_c^\infty(\Omega)$, we obtain the the macroscopic evolution PDE

$$\rho \frac{\partial^2 y}{\partial t^2} = \sum_{k=0}^{K} (-1)^{k+1} \operatorname{div}^k \Phi_{,k}^{(J),x}(y, \nabla y, \nabla^2 y, \dots, \nabla^K y) \qquad \text{in } \Omega. \tag{3.18}$$

It has to be equipped with the initial values

$$y(x,0) = y_0(x) \quad \text{and} \quad \frac{\partial y}{\partial t}(x,0) = y_1(x) \qquad \forall x \in \Omega, \tag{3.19}$$

just as on the atomic level.

Now we come to the behavior on the boundary. If the atomistic potential is constructed in such a way that the specimen is embedded into an infinite bulk crystal (compare the "fixed atoms" or "ghost atoms" in Examples 1–3), this is reflected on the continuum mechanical level by the requirement that the deformation function y at $\partial\Omega$ and its first $K-1$ derivatives in normal direction coincide with the respective derivatives of the surrounding bulk crystal. If the deformation of the surrounding bulk crystal is described by the function z, the boundary conditions read as

$$\nabla_\nu^k y(x,t) = \nabla_\nu^k z(x) \qquad \forall x \in \partial\Omega, t > 0, k = 0,1,\dots,K-1. \tag{3.20}$$

For the important special case of an undeformed surrounding crystal, i.e. $z(x) = x$, this reads as

$$y(x,t) = x, \quad \nabla_\nu y(x,t) = \nu, \quad \nabla_\nu^2 y(x,t) = \dots = \nabla_\nu^{K-1} y(x,t) = 0 \quad \forall x \in \partial\Omega, t > 0. \tag{3.21}$$

These conditions (3.20) and (3.21) are called generalized Dirichlet boundary conditions.

In the case of a specimen which is not embedded into a bulk crystal, the so-called natural boundary conditions are appropriate. They are derived as follows. If the specimen is no longer subjected to a constant deformation at the boundary, the function y must obey Newton's second law also on the boundary $\partial\Omega$. Thus we have to replace the set of test functions $C_c^\infty(\Omega)$ by $C^\infty(\overline{\Omega})$ in the above calculation. For $K = 1$ this leads to

$$\int_\Omega \rho \frac{\partial^2 y}{\partial t^2} v \, \mathrm{d}x = -\int_\Omega \Phi_{,0}^{(\mathrm{J}),x}(y,\nabla y)v \, \mathrm{d}x - \int_{\partial\Omega} \Phi_{,1}^{(\mathrm{J}),x}(y,\nabla y)v\nu \, \mathrm{d}x$$
$$+ \int_\Omega \mathrm{div}\, \Phi_{,1}^{(\mathrm{J}),x}(y,\nabla y)v \, \mathrm{d}x \tag{3.22}$$

instead of (3.17). Because of $C_c^\infty(\Omega) \subset C^\infty(\overline{\Omega})$ we obtain the same PDE (3.18) in the domain Ω. Thus the integrals over Ω in (3.22) vanish, and we have

$$\int_{\partial\Omega} \Phi_{,1}^{(\mathrm{J}),x}(y,\nabla y)v\nu \, \mathrm{d}x = 0 \tag{3.23}$$

for all $v \in C^\infty(\overline{\Omega})$. Thus we conclude the natural boundary conditions or so-called Neumann boundary conditions

$$\Phi_{,1}^{(\mathrm{J}),x}(y,\nabla y)\nu = 0 \qquad \text{on } \partial\Omega. \tag{3.24}$$

For an approximation order $K \geq 2$ the same procedure can be carried out, but the resulting natural boundary conditions are more complex. This type of boundary conditions is then called generalized Neumann boundary conditions.

3.2   Application to Atomic Chain

After having described in Section 3.1 how the upscaling process by the inner expansion technique works in detail, we will now study its outcome for the three model problems introduced in Section 2.1.2.

3.2.1   Example 1: Hookean Springs

First, we consider the atomic chain with the spring potential (2.7) as given by Example 1:

$$\Phi^{(A)}(\{y(x)\}_{x\in\mathcal{L}\cap\Omega}) = \sum_{x=0}^{L-1} \varphi\big(y(x+1) - y(x)\big). \tag{3.25}$$

According to Lemma 3.1 in Section 3.1.3, the expansion point $\overline{x}$ for the interaction of the particles $y(x)$ and $y(x+1)$ is given by the barycenter $\overline{x} = x + \frac{1}{2}$. This leads to the associated lattice $\overline{\mathcal{L}} = \mathbb{Z} + \frac{1}{2}$, and the localization

$$\Phi^{(A)} = \sum_{\overline{x}\in\overline{\mathcal{L}}\cap\Omega} \Phi^{(A),\overline{x}} \qquad \text{where} \qquad \Phi^{(A),\overline{x}}(\{y(x)\}_{x\in\mathcal{L}\cap\Omega}) = \varphi\left(y\left(\overline{x}+\tfrac{1}{2}\right) - y\left(\overline{x}-\tfrac{1}{2}\right)\right)$$

$$\tag{3.26}$$

as given by (2.10) already fits to this scheme.

The Taylor series expansion of $y(x)$ and $y(x+1)$ around $\overline{x}$ leads to

$$\Phi^{(I),\overline{x}}(y(\overline{x}),\dots,\nabla^K y(\overline{x})) = \varphi\left(\sum_{k=0}^{K} \frac{1}{k!2^k} y^{(k)}(\overline{x}) - \sum_{k=0}^{K} \frac{1}{k!(-2)^k} y^{(k)}(\overline{x})\right)$$

$$= \varphi\left(\sum_{\substack{k=1 \\ k \text{ odd}}}^{K} \frac{1}{k!2^{k-1}} y^{(k)}(\overline{x})\right). \tag{3.27}$$

We finally apply the spatial averaging procedure and obtain the continuum energy density

$$\Phi^{(J),x}(d_0, d_1, \dots, d_K) = \varphi\left(\sum_{\substack{k=1 \\ k \text{ odd}}}^{K} \frac{1}{k!2^{k-1}} d_k\right). \tag{3.28}$$

Thus we have the following lemma.

Lemma 3.2 *Let $K \in \mathbb{N}$ denote the order of approximation, and let $y \in C^K(\overline{\Omega})$. Then the quasi-continuum energy obtained from the inner expansion technique for the atomic chain with the spring potential (2.7) is given by*

$$\Phi^{(J)}(y) = \int_\Omega \Phi^{(J),x}(y(x), \nabla y(x), \dots, \nabla^K y(x)) = \int_\Omega \varphi\left(\sum_{\substack{k=1 \\ k \text{ odd}}}^{K} \frac{1}{k!2^{k-1}} y^{(k)}(x)\right) \mathrm{d}x. \tag{3.29}$$

Thus, in the case of a Hookean spring, i.e. $\varphi(r) = \frac{1}{2}(r-1)^2$, we end up with the interpolated quasi-continuum energy

$$\Phi^{(J)}(y) = \frac{1}{2}\int_\Omega y'^2(x)\,\mathrm{d}x \tag{3.30a}$$

for $K = 1$ and $K = 2$. Larger parameters K result in additional discreteness terms. We obtain

$$\Phi^{(\mathrm{J})}(y) = \frac{1}{2} \int_\Omega \left(y'(x) + \frac{1}{24} y'''(x) \right)^2 \mathrm{d}x \qquad (3.30\mathrm{b})$$

for $K = 3$ and $K = 4$ and

$$\Phi^{(\mathrm{J})}(y) = \frac{1}{2} \int_\Omega \left(y'(x) + \frac{1}{24} y'''(x) + \frac{1}{1920} y'''''(x) \right)^2 \mathrm{d}x \qquad (3.30\mathrm{c})$$

for $K = 5$ and $K = 6$.

Now we derive the equations of evolution from these potential energies. We normalize the mass of each atom to one, hence the mass density ρ disappears. According to Section 3.1.4, we obtain

$$\frac{\partial^2 y}{\partial t^2} = \frac{\partial^2 y}{\partial x^2} \qquad\qquad\qquad\qquad\qquad\qquad \text{for } K = 1, 2, \quad (3.31\mathrm{a})$$

$$\frac{\partial^2 y}{\partial t^2} = \frac{\partial^2 y}{\partial x^2} + \frac{1}{12} \frac{\partial^4 y}{\partial x^4} + \frac{1}{576} \frac{\partial^6 y}{\partial x^6} \qquad\qquad \text{for } K = 3, 4, \quad (3.31\mathrm{b})$$

$$\frac{\partial^2 y}{\partial t^2} = \frac{\partial^2 y}{\partial x^2} + \frac{1}{12} \frac{\partial^4 y}{\partial x^4} + \frac{1}{360} \frac{\partial^6 y}{\partial x^6} + \frac{1}{23040} \frac{\partial^8 y}{\partial x^8} + \frac{1}{3686400} \frac{\partial^{10} y}{\partial x^{10}} \quad \text{for } K = 5, 6. \quad (3.31\mathrm{c})$$

To compare the behavior of the solutions of these evolution equations, we solve them numerically. We choose a chain of 999 atoms with lattice constant one. This corresponds to the domain $\Omega = (0, 1000)$. The initial values at time $t = 0$ are given by $y(x, 0) = x + p(x)$ and by $\frac{\partial y}{\partial t}(x, 0) = 0$ for all $x \in \Omega$. Here, the function p introduces a small smooth perturbation around the center point $x = 500$. To be precise, p is a piecewise polynomial of order $2\omega + 1$ such that $p \equiv 0$ on $[0, 490] \cup [510, 1000]$, $p(500) = 1$ and

$$p'(x) = p''(x) = \ldots = p^{(\omega)}(x) = 0 \qquad \text{for } x = 490, 500, 510. \qquad (3.32)$$

Here we use $\omega = 3$. Concerning the boundary, we assume that the chain is embedded into an infinite undeformed chain. Thus we use the generalized Dirichlet boundary conditions (3.21) to prescribe that the chain is fixed to the identity deformation at the left and at the right side. All details concerning the discretization, the solver and the convergence analysis are given in Chapter 5.

The time evolution of the so-computed solutions of (3.31a), (3.31b) and (3.31c) is shown in Figure 3.1. To this end, the x-axis is plotted horizontally and the t-axis is plotted vertically going from top to bottom. Moreover, the color indicates the quantity $(y')^{-1}$, which corresponds to the atom density of the atomistic model. Gray denotes the equilibrium, whereas yellow and red denote regions with a high particle density and blue denotes regions with a low particle density, compare also the color bar in Figure 3.1. The time evolution of the solution of the original particle system is given in Figure 3.1 (upper left) as reference.

In all cases, we can clearly observe the propagation of the initial perturbation with constant speed to the left and to the right side. The propagation speed is correctly reproduced for all continuum models. For the model (3.31a), the initial perturbation is propagated without changing its shape. This is in full agreement with the established theory for the linear wave equation (3.31a). However, this behavior does not match that of
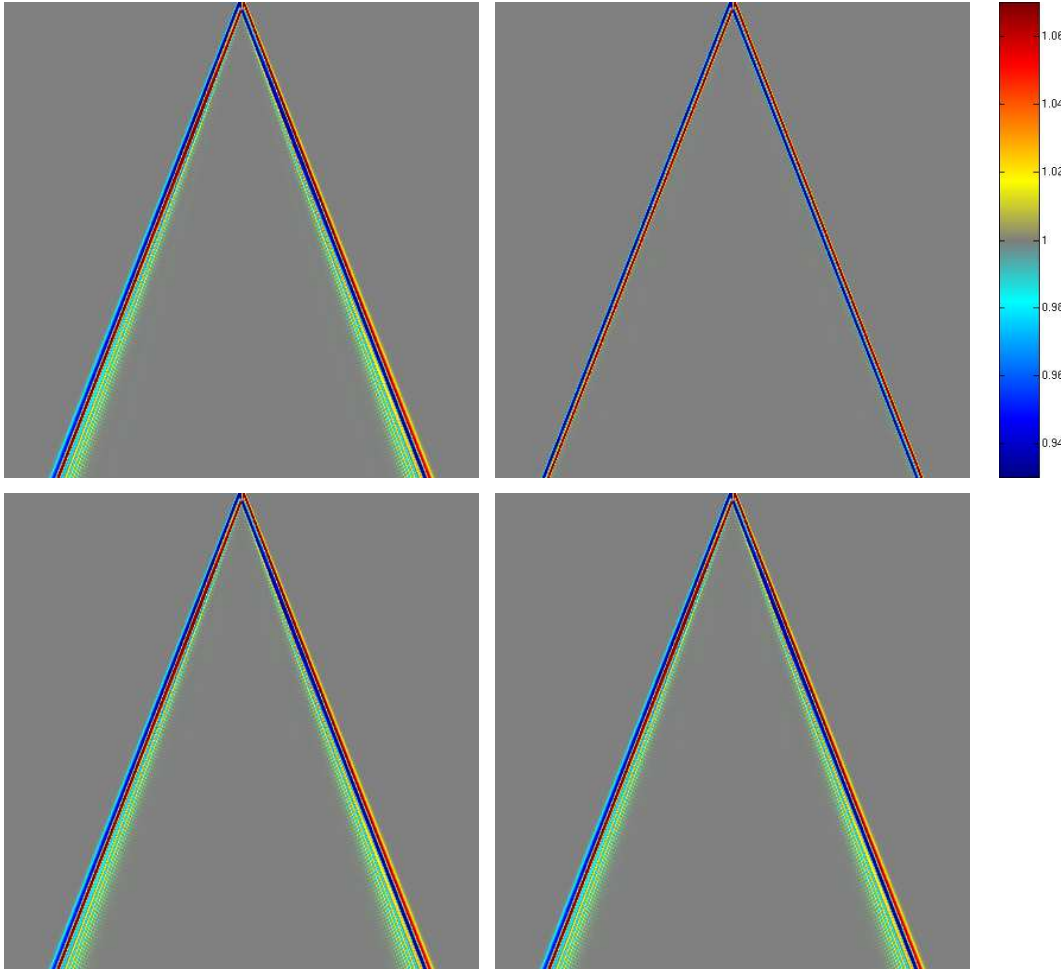
Figure 3.1: Example 1: Solutions of particle system (upper left) and of quasi-continuum systems (3.31a) for $K = 1, 2$ (upper right), (3.31b) for $K = 3, 4$ (lower left) and (3.31c) for $K = 5, 6$ (lower right).

K	2-norm of error	∞-norm of error
1	1.9306179105e-1	7.2139674139e-2
3	1.0595174636e-2	3.0471826890e-3
5	4.3215088073e-3	9.2014282448e-4

Table 3.1: Error of solution of quasi-continuum model obtained by the inner expansion technique for Example 1 at $t = 400$ with respect to solution of original particle system.

the original atomistic system. Here a distinct amount of dispersion due to the discreteness of the underlying atomistic system can be observed. But this dispersion is captured by the continuum models for $K = 3, 4$ and $K = 5, 6$. Their solutions coincide very well with the solution of the original atomistic system. The dispersion is reproduced both qualitatively and quantitatively to a high extent.

The solutions of (3.31b) and (3.31c) differ only slightly, such that the difference is
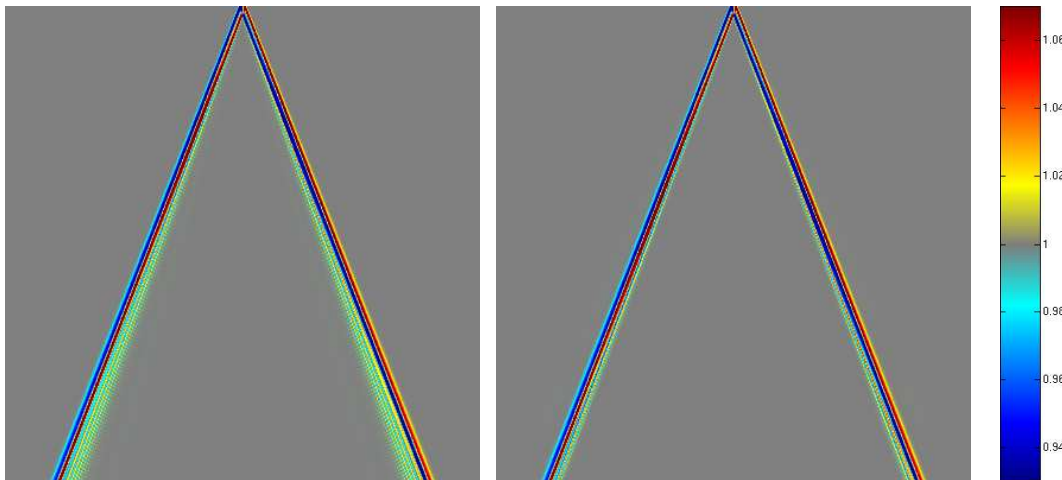
Figure 3.2: Example 1: Solutions of particle system (left) and of quasi-continuum system (3.34) for $K = 3, 4$ with non-centered expansion points (right).

not noticeable in Figure 3.1. However the deviation can be measured. The corresponding error with respect to the solution of the original particle system is given in Table 3.1. Here we see that the error is approximately 20 times smaller for $K = 3$ than for $K = 1$, but only two times smaller for $K = 5$ than for $K = 3$. Thus, the inner expansion technique with $K = 3$ already gives a very good quasi-continuum approximation of the model. The involved terms up to the third-order derivative in the potential energy suffice to accurately describe the microscopic effects.

Now we study how the choice of the expansion points affects the resulting quasi-continuum model. The choices $\overline{x} = x$ and $\overline{x} = x + 1$ instead of $\overline{x} = x + \frac{1}{2}$ lead to

$$\Phi^{(\mathrm{J})}(y) = \frac{1}{2} \int_\Omega \left(y'(x) + \frac{1}{2} y''(x) + \frac{1}{6} y'''(x) + \frac{1}{24} y''''(x) + \dots \right)^2 \mathrm{d}x \qquad (3.33\mathrm{a})$$

and

$$\Phi^{(\mathrm{J})}(y) = \frac{1}{2} \int_\Omega \left(y'(x) - \frac{1}{2} y''(x) + \frac{1}{6} y'''(x) - \frac{1}{24} y''''(x) \pm \dots \right)^2 \mathrm{d}x, \qquad (3.33\mathrm{b})$$

respectively. For $K = 3$, both potential energies result in the same evolution equation

$$\frac{\partial^2 y}{\partial t^2} = \frac{\partial^2 y}{\partial x^2} + \frac{1}{12} \frac{\partial^4 y}{\partial x^4} + \frac{1}{36} \frac{\partial^6 y}{\partial x^6}. \qquad (3.34)$$

The numerical solution of (3.34) for $K = 3$ is depicted in Figure 3.2 right. Compared to the solution of the particle system (again given in Figure 3.2 left), we see that the dispersion is clearly underestimated. Thus the choice of the expansion points has a serious impact on the resulting quasi-continuum model. It is essential to chose the correct expansion points as determined in Section 3.1.3.

3.2.2 Example 2: Lennard-Jones Potential

The inner expansion technique is certainly not limited to local interactions. We demonstrate this for the Lennard-Jones potential (2.11) from Example 2. To circumvent an
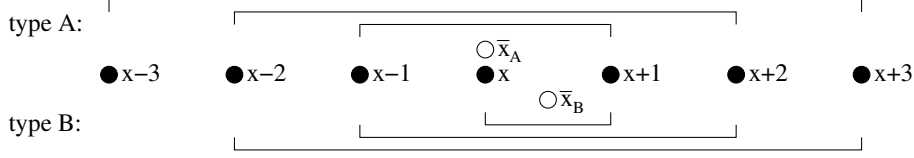
Figure 3.3: Type A and type B interactions of the Lennard-Jones potential.

annoying formalism with the boundary, we treat all atoms to be contained in an infinite bulk crystal. This is reasonable due to the rapid decay of the Lennard-Jones potential.

Again, according to Lemma 3.1, we choose the expansion points as the barycenters of the respective pair interactions. That means that we set $\overline{x} = \frac{1}{2}(x + \tilde{x})$ for the interaction of two atoms $y(x)$ and $y(\tilde{x})$. This leads to the associated lattice

$$\overline{\mathcal{L}} = \{\overline{x} + \overline{A}z \mid \overline{x} \in \overline{\mathcal{L}}_{\text{cell}}, z \in \mathbb{Z}^d\} = \tfrac{1}{2}\mathbb{Z} \qquad \text{where } \overline{A} = 1 \text{ and } \overline{\mathcal{L}}_{\text{cell}} = \{0, \tfrac{1}{2}\}. \qquad (3.35)$$

Note that many different pair interactions now share a common expansion point, such as $y(x)$ and $y(x+1)$, $y(x-1)$ and $y(x+2)$, $y(x-2)$ and $y(x+3)$ and so on. Since it makes no sense to distinguish them within the inner expansion technique, all such interactions are merged for the localization. This leads to the localized potential $\Phi^{(A)} = \sum_{\overline{x} \in \overline{\mathcal{L}} \cap \Omega} \Phi^{(A),\overline{x}}$ like in (2.5) where

$$\Phi^{(A),\overline{x}}\big(\{y(x)\}_{x \in \mathcal{L} \cap \Omega}\big) = \begin{cases} \sum\limits_{z=1}^{\infty} \varphi\big(y(\overline{x}+z) - y(\overline{x}-z)\big) & \text{if } \overline{x} \in \mathbb{Z} \cap \Omega \\ & \text{(type A interaction),} \\ \sum\limits_{z=1}^{\infty} \varphi\big(y(\overline{x}+z-\tfrac{1}{2}) - y(\overline{x}-z+\tfrac{1}{2})\big) & \text{if } \overline{x} \in (\mathbb{Z}+\tfrac{1}{2}) \cap \Omega \\ & \text{(type B interaction).} \end{cases}$$
$$(3.36)$$

We now have two different types A and B of interaction for the two respective elements of $\overline{\mathcal{L}}_{\text{cell}}$, see Figure 3.3. This forces us to define the associated lattice $\overline{\mathcal{L}}$ as in (3.35) and not by means of the simpler definition $\overline{A} = \frac{1}{2}$ and $\overline{\mathcal{L}}_{\text{cell}} = \{0\}$.

Then, we substitute the Taylor series expansion (3.1) of y around $\overline{x}$ into (3.36) and reformulate the potential according to (3.2):

$$\Phi^{(I),\overline{x}}(d_0, \ldots, d_K) = \begin{cases} \sum\limits_{z=1}^{\infty} \varphi\bigg(\sum\limits_{\substack{k=1 \\ k \text{ odd}}}^{K} \frac{2}{k!} y^{(k)}(x) z^k \bigg) & \text{if } \overline{x} \in \mathbb{Z} \cap \Omega \\ & \text{(type A interaction),} \\ \sum\limits_{z=1}^{\infty} \varphi\bigg(\sum\limits_{\substack{k=1 \\ k \text{ odd}}}^{K} \frac{2}{k!} y^{(k)}(x) \big(z-\tfrac{1}{2}\big)^k \bigg) & \text{if } \overline{x} \in (\mathbb{Z}+\tfrac{1}{2}) \cap \Omega \\ & \text{(type B interaction).} \end{cases} \qquad (3.37)$$

Note that this is an example where the sum over all $\overline{x} \in \overline{\mathcal{L}}_{\text{cell}}$ in (3.7) cannot be avoided, because the two different types of interaction have to be distinguished. As the next step, we apply the averaging procedure and yield

$$\Phi^{(J),x}(d_0, \ldots, d_K) = \frac{1}{\det \overline{A}} \sum_{\overline{x} \in \overline{\mathcal{L}}_{\text{cell}}} \Phi^{(I),\overline{x}}(d_0, \ldots, d_K)$$

$$= \sum_{z=1}^{\infty} \left[\varphi\left(\sum_{\substack{k=1 \\ k \text{ odd}}}^{K} \frac{2}{k!} d_k z^k \right) + \varphi\left(\sum_{\substack{k=1 \\ k \text{ odd}}}^{K} \frac{2}{k!} d_k \left(z - \tfrac{1}{2} \right)^k \right) \right]$$

$$= \sum_{z=1}^{\infty} \left[\varphi\left(\sum_{\substack{k=1 \\ k \text{ odd}}}^{K} \frac{1}{k!2^{k-1}} d_k (2z)^k \right) + \varphi\left(\sum_{\substack{k=1 \\ k \text{ odd}}}^{K} \frac{2}{k!2^{k-1}} d_k (2z-1)^k \right) \right]$$

$$= \sum_{z=1}^{\infty} \varphi\left(\sum_{\substack{k=1 \\ k \text{ odd}}}^{K} \frac{1}{k!2^{k-1}} d_k z^k \right). \tag{3.38}$$

Thus we end up with the following lemma.

Lemma 3.3 *Let $K \in \mathbb{N}$ denote the order of approximation, and let $y \in C^K(\overline{\Omega})$. Then the interpolated quasi-continuum energy obtained from the inner expansion technique for the atomic chain with the Lennard-Jones potential* (2.11) *is given by*

$$\Phi^{(\mathrm{J})}(y) = \int_{\Omega} \sum_{z=1}^{\infty} \varphi\left(\sum_{\substack{k=1 \\ k \text{ odd}}}^{K} \frac{1}{k!2^{k-1}} y^{(k)}(x) z^k \right) \, \mathrm{d}x. \tag{3.39}$$

In case of $K = 1$ and $K = 2$, this can be further simplified as

$$\Phi^{(\mathrm{J})}(y) = \int_{\Omega} \sum_{z=1}^{\infty} \varphi\big(z y'(x) \big) \, \mathrm{d}x$$

$$= \int_{\Omega} \sum_{z=1}^{\infty} \frac{1}{z^{12}} \left(\frac{\sigma}{y'(x)} \right)^{12} - \sum_{z=1}^{\infty} \frac{1}{z^6} \left(\frac{\sigma}{y'(x)} \right)^6$$

$$= \int_{\Omega} \overline{\varphi}\big(y'(x) \big) \, \mathrm{d}x, \tag{3.40}$$

where the effective interaction potential $\overline{\varphi}$ is given by

$$\overline{\varphi}(r) = \zeta(12) \left(\frac{\sigma}{r} \right)^{12} - \zeta(6) \left(\frac{\sigma}{r} \right)^6, \tag{3.41}$$

compare the definition (2.14) of the ζ-function.

For $K = 3$ and $K = 4$ we obtain

$$\Phi^{(\mathrm{J})}(y) = \int_{\Omega} \sum_{z=1}^{\infty} \varphi\left(y'(x) z + \tfrac{1}{24} y'''(x) z^3 \right) \, \mathrm{d}x, \tag{3.42}$$

and for $K = 5$ and $K = 6$ we have

$$\Phi^{(\mathrm{J})}(y) = \int_{\Omega} \sum_{z=1}^{\infty} \varphi\left(y'(x) z + \tfrac{1}{24} y'''(x) z^3 + \tfrac{1}{1920} y'''''(x) z^5 \right) \, \mathrm{d}x. \tag{3.43}$$

For $K \geq 3$, no closed form is known to us which avoids the sum over all z as in (3.40).

The equations of evolution (3.18) for this potential read as

$$\frac{\partial^2 y}{\partial t^2} = \frac{\partial}{\partial x}\overline{\varphi}'(y') \qquad\qquad\qquad \text{for } K = 1, 2, \qquad (3.44\text{a})$$

$$\frac{\partial^2 y}{\partial t^2} = \sum_{z=1}^{\infty} \left[z\frac{\partial}{\partial x}\varphi'\big(y'z + \tfrac{1}{24}y'''z^3\big) \right.$$

$$\left. + \frac{1}{24}z^3\frac{\partial^3}{\partial x^3}\varphi'\big(y'z + \tfrac{1}{24}y'''z^3\big) \right] \qquad\qquad \text{for } K = 3, 4, \qquad (3.44\text{b})$$

$$\frac{\partial^2 y}{\partial t^2} = \sum_{z=1}^{\infty} \left[z\frac{\partial}{\partial x}\varphi'\big(y'z + \tfrac{1}{24}y'''z^3 + \tfrac{1}{1920}y'''''z^5\big) \right.$$

$$+ \frac{1}{24}z^3\frac{\partial^3}{\partial x^3}\varphi'\big(y'z + \tfrac{1}{24}y'''z^3 + \tfrac{1}{1920}y'''''z^5\big)$$

$$\left. + \frac{1}{1920}z^5\frac{\partial^5}{\partial x^5}\varphi'\big(y'z + \tfrac{1}{24}y'''z^3 + \tfrac{1}{1920}y'''''z^5\big) \right] \qquad \text{for } K = 5, 6. \qquad (3.44\text{c})$$

For the numerical comparison of the evolution equations (3.44a), (3.44b) and (3.44c), we use the same atomic chain with 999 atoms as in Example 1. The main difference to the previous example is the nonlinearity of the evolution equation. Thus we have to deal with shocks. The initial configuration is the same as in Example 1, the only difference is that we have chosen a wider support (400 instead of 20) of the perturbation function p and $\omega = 10$ to make the shocks more visible.

The time evolution of the numerically computed solutions of the original atomistic system and of the macroscopic models obtained by the inner expansion technique with $K = 1$, $K = 3$ and $K = 5$ are shown in Figure 3.4. We can observe essentially the same propagation of the initial perturbation towards both boundaries as in Example 1. Note that now the propagation speed is no longer constant due to the nonlinearity, i.e. the perturbation changes its shape. After a certain time, sharp shock waves develop, which can be clearly seen in all solutions. Note furthermore that in the vicinity of the shock waves the solution of the original atomistic model shows a distinct scattering. This dispersive effect is lost on the macroscopic level for $K = 1$, but it is captured to a very high extent for $K = 3$ and $K = 5$.

3.2.3   Example 3: Multibody Potential

Now we consider the atomic chain with the three-body potential (2.16) from Example 3. Here, the expansion point $\overline{x}$ for the interaction of $y(x - 1)$, $y(x)$ and $y(x + 1)$ is given by $\overline{x} = x$. Therefore we have $\overline{\mathcal{L}} = \mathcal{L}$. By a calculation which is similar to that for Example 1, the substitution of the Taylor series expansion of y and the averaging procedure lead to the continuum energy density

$$\Phi^{(\text{J}),\overline{x}}(d_0, d_1, \ldots, d_K) = \varphi\left(\sum_{\substack{k=1 \\ k \text{ even}}}^{K} \frac{2}{k!}d_k \right). \qquad (3.45)$$

Thus we have the following lemma.
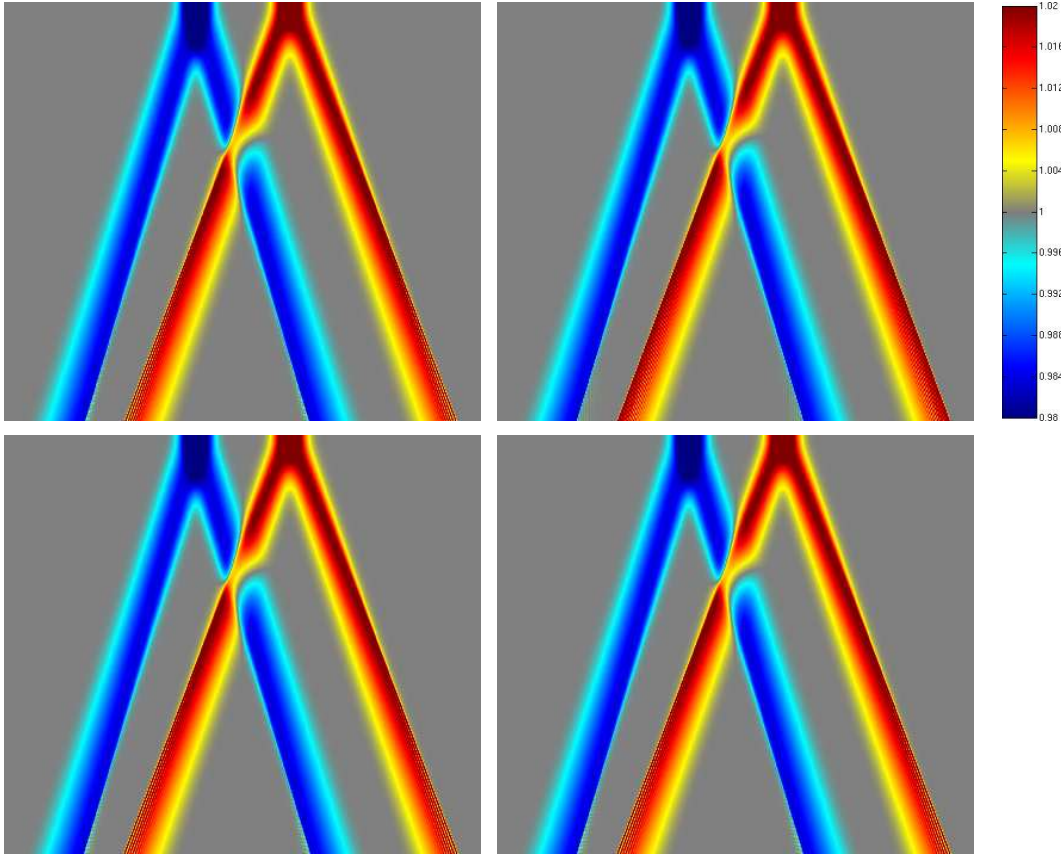
Figure 3.4: Example 2: Solutions of particle system (upper left) and of quasi-continuum systems (3.44a) for $K = 1, 2$ (upper right), (3.44b) for $K = 3, 4$ (lower left) and (3.44c) for $K = 5, 6$ (lower right).

Lemma 3.4 *Let $K \in \mathbb{N}$ denote the order of approximation, and let $y \in C^K(\overline{\Omega})$. Then the quasi-continuum potential energy obtained from the inner expansion technique for the atomic chain with the potential (2.16) is given by*

$$\Phi^{(\mathrm{J})}(y) = \int_\Omega \varphi\left(\sum_{\substack{k=1 \\ k \text{ even}}}^{K} \frac{2}{k!} y^{(k)}(x) \right) \mathrm{d}x. \tag{3.46}$$

This results in the potential energies

$$\Phi^{(\mathrm{J})}(y) = \int_\Omega \varphi\big(y''(x)\big) \, \mathrm{d}x \qquad \text{for } K = 2, 3, \tag{3.47a}$$

$$\Phi^{(\mathrm{J})}(y) = \int_\Omega \varphi\left(y''(x) + \tfrac{1}{12} y''''(x)\right) \, \mathrm{d}x \qquad \text{for } K = 4, 5 \text{ and} \tag{3.47b}$$

$$\Phi^{(\mathrm{J})}(y) = \int_\Omega \varphi\left(y''(x) + \tfrac{1}{12} y''''(x) + \tfrac{1}{360} y''''''(x)\right) \, \mathrm{d}x \qquad \text{for } K = 6, 7. \tag{3.47c}$$
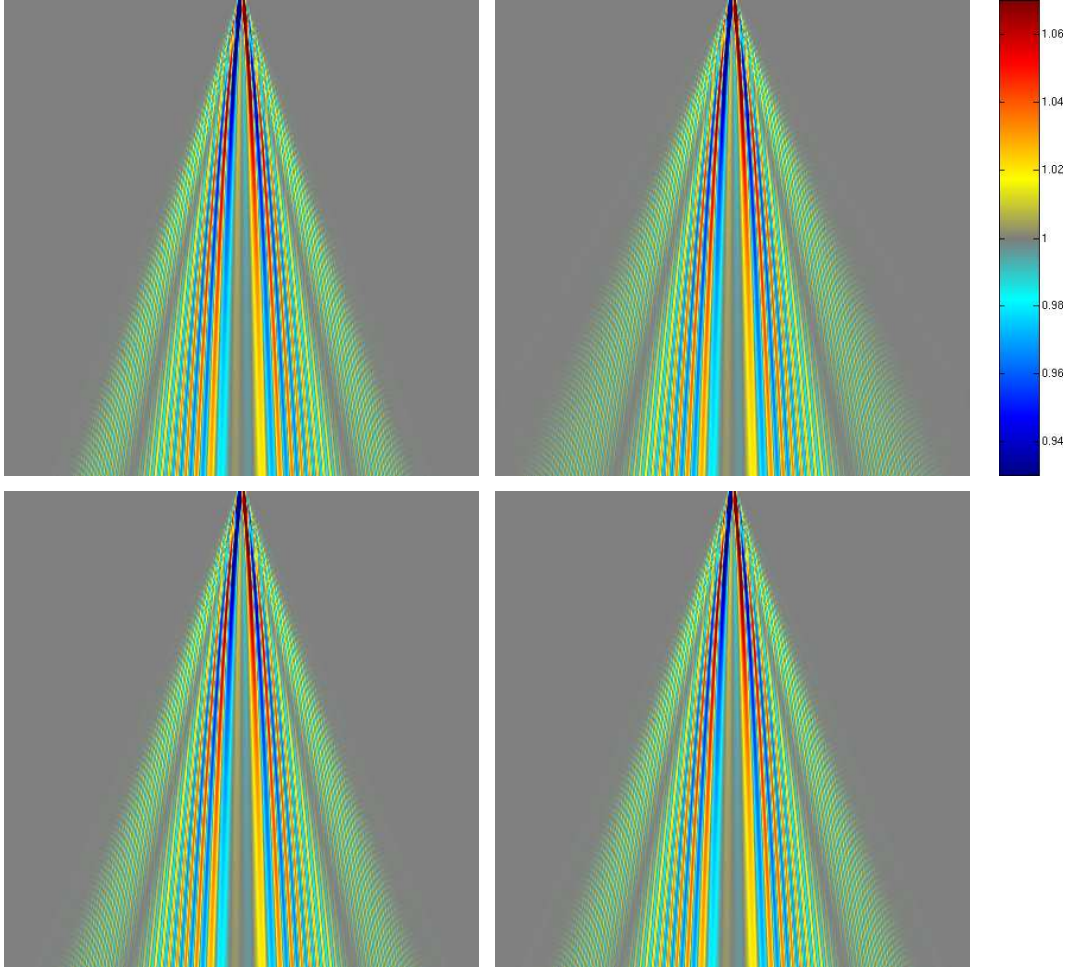
Figure 3.5: Example 3: Solutions of particle system (upper left) and of quasi-continuum systems (3.48a) for $K = 2, 3$ (upper right), (3.48b) for $K = 4, 5$ (lower left) and (3.48c) for $K = 6, 7$ (lower right).

The according macroscopic evolution equations for the interaction potential $\varphi(r) = \frac{1}{2}r^2$ as given by (2.17) then read as

$$\frac{\partial^2 y}{\partial t^2} = -\frac{\partial^4 y}{\partial x^4} \qquad\qquad\qquad\qquad\qquad\qquad\qquad \text{for } K = 2, 3, \qquad (3.48a)$$

$$\frac{\partial^2 y}{\partial t^2} = -\frac{\partial^4 y}{\partial x^4} - \frac{1}{6}\frac{\partial^6 y}{\partial x^6} - \frac{1}{144}\frac{\partial^8 y}{\partial x^8} \qquad\qquad\qquad \text{for } K = 4, 5 \text{ and} \quad (3.48b)$$

$$\frac{\partial^2 y}{\partial t^2} = -\frac{\partial^4 y}{\partial x^4} - \frac{1}{6}\frac{\partial^6 y}{\partial x^6} - \frac{1}{80}\frac{\partial^8 y}{\partial x^8} - \frac{1}{2160}\frac{\partial^{10} y}{\partial x^{10}} - \frac{1}{129600}\frac{\partial^{12} y}{\partial x^{12}} \quad \text{for } K = 6, 7. \qquad (3.48c)$$

For the numerical comparison, we use the same setting as for Example 1. The time evolution of the numerically computed solutions of the original atomistic system and of equations (3.48a) and (3.48b) are shown in Figure 3.5. All three solutions are in good agreement. The fanning out pattern is captured qualitatively very well. However, a closer look reveals that the angles of the resulting striped delta shapes are not correctly

reproduced for $K = 2$. But for $K = 4$ and $K = 6$, they are very close to the ones of the particle system.

3.3   Hyperbolicity and Well-posedness

After we analyzed the inner expansion technique numerically, we now show an important feature of this technique analytically, namely that convexity of the atomistic model is preserved under the inner expansion technique. This is a relevant point, since the fact which characteristic properties of the atomistic potential are transferred from the microscale to the macroscale and which are not heavily affects the behavior of the continuum model. In this case, convexity is used to prove that the resulting macroscopic evolution equations are well-posed.

The essential criterion whether the evolution equations studied here are well-posed or ill-posed is hyperbolicity. We call the equation (3.18) hyperbolic if the right hand side is a negative semidefinite operator in space. This property is the essential ingredient in existence proofs to derive stability estimates. We prove in Lemma 3.6 below that this property holds if the continuum potential is convex.

Now, if already the original atomistic potential is not convex, this cannot be expected to hold for the resulting continuum potential. But if the original atomistic potential is convex, it still depends on the upscaling scheme whether this property is carried over to the continuum level or not. The next lemma shows that the inner expansion technique indeed preserves convexity of the atomistic potential.

One immediately obtains the following lemma from the description of the inner expansion technique.

Lemma 3.5 *Let the atomistic potential $\Phi^{(A)}$ be convex. Then the continuum potentials $\Phi^{(I)}$ and $\Phi^{(J)}$ obtained by the inner expansion technique are convex as well.*

Let us note that this lemma holds for the scaling technique as well, but not for the direct expansion technique.

The convexity of the continuum potential is now used to proof that the corresponding macroscopic evolution equations are hyperbolic and well-posed.

Lemma 3.6 *Assume that the continuum potential (3.7) is convex and that the reference configuration is an equilibrium configuration. Then the corresponding evolution equation (3.17) with boundary conditions (3.21) is hyperbolic.*

PROOF It has to be verified that the spatial operator of (3.17) is negative semidefinite. To this end, we test with $y - \mathrm{id}$. By the mean value theorem we have for some intermediate function $\tilde{y} = \mathrm{id} + \vartheta(y - \mathrm{id})$ with $\vartheta \in (0, 1)$:

$$
-\int_\Omega \sum_{k=0}^{K} (-1)^k \operatorname{div}^k \Phi_{,k}^{(\mathrm{J}),x}(y, \nabla y, \ldots, \nabla^K y)(y - \mathrm{id}) \, \mathrm{d}x
$$

$$
= -\int_\Omega \sum_{k=0}^{K} \Phi_{,k}^{(\mathrm{J}),x}(y, \nabla y, \ldots, \nabla^K y) : \nabla^k (y - \mathrm{id}) \, \mathrm{d}x
$$

$$= -\int_\Omega \sum_{k=0}^K \Phi_{,k}^{(\mathrm{J}),x}(\mathrm{id}, I, 0, \ldots, 0) : \nabla^k (y - \mathrm{id}) \, \mathrm{d}x$$

$$\quad - \int_\Omega \sum_{k,l=0}^K \nabla^l (y - \mathrm{id}) : \Phi_{,k,l}^{(\mathrm{J}),x}(\tilde{y}, \nabla \tilde{y}, \ldots, \nabla^K \tilde{y}) : \nabla^k (y - \mathrm{id}) \, \mathrm{d}x$$

$$= -\Phi^{(\mathrm{J})'}(\mathrm{id}; y - \mathrm{id}) - \Phi^{(\mathrm{J})''}(\tilde{y}; y - \mathrm{id}, y - \mathrm{id}). \tag{3.49}$$

Here the boundary integrals which arise from the partial integration vanish due to the boundary conditions. The first directional derivative $\Phi^{(\mathrm{J})'}(\mathrm{id}; y - \mathrm{id})$ vanishes because id is an equilibrium configuration. The second directional derivative $\Phi^{(\mathrm{J})''}(\tilde{y}; y - \mathrm{id}, y - \mathrm{id})$ is nonnegative, since the potential $\Phi^{(\mathrm{J})}$ is assumed to be convex. Hence the expression (3.49) is non-positive. $\square$

Note that the Lennard-Jones potential is locally convex around the equilibrium configuration, but not globally convex. However, if the initial conditions are close to the equilibrium, then the solution is close to the equilibrium as well. Thus, if the initial conditions are chosen sufficiently small, the solution stays within this convex region. Then the locally convex potential acts as a globally convex potential and the above argumentation works for this case as well.

In several cases the assumption of convexity of the atomistic potential may not be fulfilled, for example in the multivariate case where the frame indifference inhibits this property. Then, similar arguments can be used to show that other characteristic properties are transferred to the macroscale by the inner expansion technique. This point will be discussed extensively in Section 4.1 for the frame indifference.

3.4   Comparison with Other Upscaling Techniques

Besides the inner expansion technique, other methods for the upscaling process from atomistic to continuum mechanical models have been proposed by several authors. Two important methods are given by the so-called scaling technique and by the so-called direct expansion technique. In the following, we will briefly describe these methods and compare them to the inner expansion technique.

3.4.1   Scaling Technique

First, we come to the scaling technique. It has been used and analyzed by Blanc, Le Bris and Lions [17], E and Huang [31] and many others.

3.4.1.1   Description of the Scheme

Recall that the shape of the specimen is described by the domain $\Omega \subset \mathbb{R}^d$, see Section 2.1.1. From the atomic level, we are given the filling $\mathcal{L} \cap \Omega$ of the domain Ω with atoms arranged in form of the lattice $\mathcal{L}$. The lattice distance resembles the physical length scale of the atoms and has always been fixed up to now. The principle of the scaling technique is to replace $\mathcal{L} \cap \Omega$ by a filling with a finer lattice. To this end, we scale the lattice by some factor $\varepsilon \in \mathbb{R}^+$ and replace $\mathcal{L} \cap \Omega$ in (2.2) by $\varepsilon \mathcal{L} \cap \Omega$. For $\varepsilon < 1$, this corresponds to a description of the solid with more atoms, see Figure 3.6.
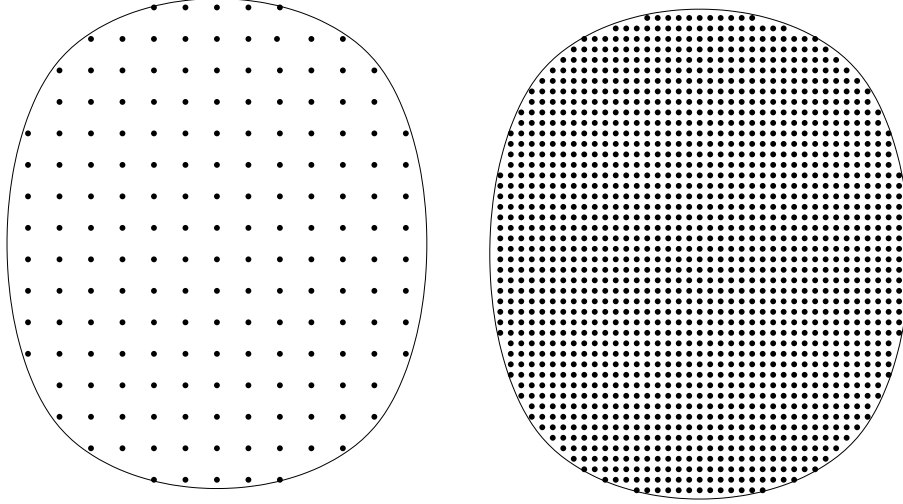
Figure 3.6: Filling of the domain Ω with $\mathcal{L}$ (left) and $\varepsilon\mathcal{L}$ (right).

The set of atoms is used to describe the behavior of the specimen in terms of the potential energy. The original atomistic potential $\Phi^{(A)}$ and the local potentials $\Phi^{(A),\overline{x}}$ for $\overline{x} \in \overline{\mathcal{L}} \cap \Omega$ as defined in (2.5) are given on the length scale of the physical lattice constant. We denote this length scale by one. Now, the original potentials cannot directly be applied to the length scale ε, but must be rescaled properly. To this end, we multiply the arguments of $\Phi^{(A),\overline{x}}$ with ε^{-1}. If the points $\{y(x)\}_{x\in\varepsilon\mathcal{L}\cap\Omega}$ denote the atom positions on the length scale ε, then the points $\{\varepsilon^{-1}y(x)\}_{x\in\varepsilon\mathcal{L}\cap\Omega}$ are atom positions on the length scale one. They now can be used for the physical potential $\Phi^{(A),\overline{x}}$. This way, the potential $\Phi^{(A),\varepsilon,\overline{x}}$ for the length scale ε is obtained from $\Phi^{(A),\overline{x}}$ by

$$\Phi^{(A),\varepsilon,\overline{x}}(\{y(x)\}_{x\in\varepsilon\mathcal{L}\cap\Omega}) := \Phi^{(A),\overline{x}}(\{\varepsilon^{-1}y(x)\}_{x\in\varepsilon\mathcal{L}\cap\Omega}). \tag{3.50}$$

The total potential $\Phi^{(A),\varepsilon}$ for the length scale ε is then given by the sum over $\Phi^{(A),\varepsilon,\overline{x}}$ for all expansion points $\overline{x} \in \varepsilon\overline{\mathcal{L}} \cap \Omega$. Since the number $N_\varepsilon = |\varepsilon\overline{\mathcal{L}} \cap \Omega|$ of expansion points as well as the number of atoms on the length scale ε scale like ε^{-d}, i.e. $N_\varepsilon \approx \varepsilon^{-d}N_1$, we multiply this sum by ε^d to keep the total potential energy at the order $\mathcal{O}(1)$. Altogether, we obtain

$$\Phi^{(A),\varepsilon}(\{y(x)\}_{x\in\varepsilon\mathcal{L}\cap\Omega}) := \varepsilon^d \sum_{\overline{x}\in\varepsilon\overline{\mathcal{L}}\cap\Omega} \Phi^{(A),\varepsilon,\overline{x}}(\{y(x)\}_{x\in\varepsilon\mathcal{L}\cap\Omega})$$

$$= \varepsilon^d \sum_{\overline{x}\in\varepsilon\overline{\mathcal{L}}\cap\Omega} \Phi^{(A),\overline{x}}(\{\varepsilon^{-1}y(x)\}_{x\in\varepsilon\mathcal{L}\cap\Omega}). \tag{3.51}$$

Note that $\Phi^{(A),\varepsilon,\overline{x}}$ here acts as a discrete energy density.

An equivalent way to construct $\Phi^{(A),\varepsilon}$ is to replace the domain Ω by the scaled domain $\varepsilon^{-1}\Omega$, to fill it with atoms by means of $\mathcal{L} \cap \varepsilon^{-1}\Omega$, and then to define $\Phi^{(A),\varepsilon}$ as $\varepsilon^d\Phi^{(A)}$ on this set.

Now assume that the deformation y is not only given on the discrete sets $\mathcal{L} \cap \Omega$ or $\varepsilon\mathcal{L} \cap \Omega$, but continuously on the whole domain Ω, i.e. that $y : \Omega \to \mathbb{R}^d$ is a mapping from

the full domain Ω to $\mathbb{R}^d$. Then, the potential energy of y can be defined for any length scale $\varepsilon > 0$ by restricting y to $\varepsilon\mathcal{L} \cap \Omega$:

$$\Phi^{(A),\varepsilon}(y) := \Phi^{(A),\varepsilon}(\{y(x)\}_{x\in\varepsilon\mathcal{L}\cap\Omega}). \tag{3.52}$$

The challenge is now to determine the continuum limit

$$\Phi^{(S)}(y) := \lim_{\varepsilon\to 0} \Phi^{(A),\varepsilon}(y). \tag{3.53}$$

The limit potential energy $\Phi^{(S)}$ is then used in a model on the macroscale.

For simple pair potentials which satisfy a certain decay condition that ensures finiteness of the sums, it can be shown that this limit is of the form

$$\Phi^{(S)}(y) = \int_\Omega \Phi^{(S),x}(\nabla y(x))\, \mathrm{d}x, \tag{3.54}$$

see [17] for a rigorous proof. We expect that similar results also hold for more complicated many-body potentials, though we are not aware of any proof in the literature. Note however that the mere existence of the limit does not yet say anything about its *quality*, i.e. which information from the microscale is kept on the macroscale and which is not. This point will be examined in more detail in the next section.

3.4.1.2   Typical Examples

We now analyze how the scaling technique performs for typical sample problems. For the situation of Example 1, the following lemma holds according to [17, Theorem 1].

Lemma 3.7 *Let $y \in C^2(\overline{\Omega})$. Then the continuum limit obtained from the scaling technique for the atomic chain with spring potential* (2.7) *is given by*

$$\Phi^{(S)}(y) = \lim_{\varepsilon\to 0} \Phi^{(A),\varepsilon}(y) = \int_\Omega \varphi\big(y'(x)\big)\, \mathrm{d}x. \tag{3.55}$$

For the proof, the difference $y(\overline{x}+\frac{1}{2})-y(\overline{x}-\frac{1}{2})$ for some point $\overline{x} \in \overline{\mathcal{L}}\cap\Omega$ is transformed under the scaling procedure to the difference quotient

$$\frac{y(\overline{x} + \varepsilon\frac{1}{2}) - y(\overline{x} - \varepsilon\frac{1}{2})}{\varepsilon}, \tag{3.56}$$

which nicely converges to $y'(\overline{x})$. Furthermore, the sum $\varepsilon\sum_{\overline{x}\in\varepsilon\mathcal{L}\cap\Omega}$ is a Riemann sum for the integral. The smoothness assumption on y then allows to simultaneously perform both limit processes.

The resulting continuum model coincides with the model obtained by the inner expansion technique for $K = 1$. For this model, the numerical experiments showed that the corresponding solutions reproduce the transport effect of the initial shape very well, but lack any dispersive effects. These dispersive effects come from the discreteness of the atomistic system. The absence of the dispersion is immanent to the scaling technique, because it describes the thermodynamic limit $N \to \infty$ and not the quasi-continuum behavior for a large, but finite N. In the limit the dispersion vanishes.

Similar to the spring model, the scaling technique also works for nonlocal interactions as given in Example 2. Again, [17, Theorem 1] provides us with the following lemma.

Lemma 3.8 *Let $y \in C^2(\overline{\Omega})$. Then the continuum limit obtained from the scaling technique for the atomic chain with Lennard-Jones potential* (2.11) *is given by*

$$\Phi^{(S)}(y) = \lim_{\varepsilon \to 0} \Phi^{(A),\varepsilon}(y) = \frac{1}{2} \int_\Omega \sum_{z \in \mathbb{Z} \setminus \{0\}} \varphi(y'(x)z) \, \mathrm{d}x. \tag{3.57}$$

Here, the infinite sum can be explicitly determined in a similar way to (3.40). It holds

$$\frac{1}{2} \sum_{z \in \mathbb{Z} \setminus \{0\}} \varphi(y'(x)z) = \sum_{z=1}^{\infty} \left[\left(\frac{\sigma}{y'(x)z} \right)^{12} - \left(\frac{\sigma}{y'(x)z} \right)^{6} \right]$$

$$= \left(\frac{\sigma}{y'(x)} \right)^{12} \zeta(12) - \left(\frac{\sigma}{y'(x)} \right)^{6} \zeta(6)$$

$$= \overline{\varphi}(y'(x)), \tag{3.58}$$

where $\overline{\varphi}$ is given by (3.41). Hence the continuum energy (3.57) reads as

$$\Phi^{(S)}(y) = \int_\Omega \overline{\varphi}\big(y'(x)\big) \, \mathrm{d}x. \tag{3.59}$$

The function $\overline{\varphi}$ plays the role of an "effective Lennard-Jones potential". It is close to φ since $\zeta(6)$ and $\zeta(12)$ are close to 1, compare Table 2.1. This resembles the fact that the far field interactions contribute to the overall potential only up to a small extent due to the rapid decay of the Lennard-Jones potential.

Note that the continuum potential (3.59) again coincides with the outcome of the inner expansion technique for $K = 1$.

Both, the spring potential and the Lennard-Jones potential, are relatively simple potentials. Physically meaningful potentials of real solids are much more complex. As already described in the previous chapter, it is often not sufficient to deal with pair potentials only, instead one has to take into account many-body interactions as well. This however can have adverse effects for the scaling technique, as we can see from the (still simple) three-body potential of Example 3. We have the following lemma.

Lemma 3.9 *Let $\Omega \subset \mathbb{R}$ be a bounded domain. Let $y \in C^2(\overline{\Omega})$ and let φ be continuous at 0. Then the continuum limit obtained from the scaling technique for the atomic chain with potential* (2.16) *is given by*

$$\Phi^{(S)}(y) = \int_\Omega \varphi(0) \, \mathrm{d}x. \tag{3.60}$$

PROOF The scaled potential is given by

$$\Phi^{(A),\varepsilon}(y) = \varepsilon \sum_{\overline{x} \in \varepsilon \overline{\mathcal{L}} \cap \Omega} \varphi \left(\frac{y(\overline{x} + \varepsilon) - 2y(\overline{x}) + y(\overline{x} - \varepsilon)}{\varepsilon} \right). \tag{3.61}$$

The Taylor expansion of $y(\overline{x} + \varepsilon)$ and $y(\overline{x} - \varepsilon)$ around $\overline{x}$ gives

$$\varphi \left(\frac{y(\overline{x} + \varepsilon) - 2y(\overline{x}) + y(\overline{x} - \varepsilon)}{\varepsilon} \right) = \varphi \left(\varepsilon y''(\xi_{\overline{x}}) \right) \tag{3.62}$$

for some point $\xi_{\overline{x}} \in \Omega$. Now, let $\mathrm{vol}\,\Omega := \int_{\Omega} 1\,\mathrm{d}x$ denote the volume of Ω and card the cardinality of a set. We then obtain

$$\left| \Phi^{(A),\varepsilon}(y) - \int_{\Omega} \varphi(0)\,\mathrm{d}x \right|$$

$$= \left| \varepsilon \sum_{\overline{x} \in \varepsilon\overline{\mathcal{L}} \cap \Omega} \left(\varphi\big(\varepsilon y''(\xi_{\overline{x}})\big) - \varphi(0) \right) - \varphi(0)\left(\mathrm{vol}\,\Omega - \varepsilon\,\mathrm{card}(\varepsilon\overline{\mathcal{L}} \cap \Omega) \right) \right|$$

$$\leq \varepsilon\,\mathrm{card}(\varepsilon\overline{\mathcal{L}} \cap \Omega) \max_{\overline{x} \in \varepsilon\overline{\mathcal{L}} \cap \Omega} \left| \varphi\big(\varepsilon y''(\xi_{\overline{x}})\big) - \varphi(0) \right| + |\varphi(0)| \left| \mathrm{vol}\,\Omega - \varepsilon\,\mathrm{card}(\varepsilon\overline{\mathcal{L}} \cap \Omega) \right|$$

$$\overset{\varepsilon \to 0}{\longrightarrow} 0 \tag{3.63}$$

since y'' is bounded and $\varepsilon\,\mathrm{card}(\varepsilon\overline{\mathcal{L}} \cap \Omega) \to \mathrm{vol}\,\Omega$ as $\varepsilon \to 0$. $\hspace{1cm}\square$

Hence $\Phi^{(S)}$ is a constant functional and gives no information about the system at all. The continuum limit obtained by the scaling technique is completely useless for this specific model problem. We admit that the interaction potential (2.16) is somewhat artificial and marks an extreme case. However this example shows an effect which can occur for the scaling technique if many-body potentials are used instead of pair potentials.

The reason for this failure of the scaling technique will be examined in the following section.

3.4.1.3 Asymptotic Analysis

Consider the Taylor series expansion of the deformation function y around a point $\hat{x} \in \Omega$. Without loss of generality we set $\hat{x} = 0$, the same behavior for general $\hat{x} \in \Omega$ is obtained after a translation. If we assume for the moment that the series expansion exists and converges to y, we obtain

$$\Phi^{(A),\varepsilon,0}(\{y(x)\}_{x \in \varepsilon\mathcal{L} \cap \Omega}) = \Phi^{(A),\varepsilon,0}\left(\left\{ \sum_{k=0}^{\infty} \frac{1}{k!} x^k y^{(k)}(0) \right\}_{x \in \varepsilon\mathcal{L} \cap \Omega} \right)$$

$$= \Phi^{(A),0}\left(\left\{ \varepsilon^{-1} \sum_{k=0}^{\infty} \frac{1}{k!} (\varepsilon x)^k y^{(k)}(0) \right\}_{x \in \mathcal{L} \cap \varepsilon^{-1}\Omega} \right)$$

$$= \Phi^{(A),0}\left(\left\{ \sum_{k=0}^{\infty} \varepsilon^{k-1} \frac{1}{k!} x^k y^{(k)}(0) \right\}_{x \in \mathcal{L} \cap \varepsilon^{-1}\Omega} \right). \tag{3.64}$$

The terms with $k = 0$ would blow up to infinity as $\varepsilon \to 0$. However, since every physically reasonable potential is translation invariant, these terms do not appear at all. The terms with $k = 1$ are of order one. They are thus captured by the limit process and the first derivatives show up in the limit continuum energy. All higher terms, i.e. those with $k \geq 2$, disappear in the limit process because $\varepsilon^{k-1} \to 0$ as $\varepsilon \to 0$.

Therefore the continuum energy obtained by the scaling technique depends only on the first derivatives. The scaling preserves the terms of the first non-vanishing order $k = 1$. All higher order effects of the potential are lost by this type of scaling and the limiting process. This is just what happened in Example 3, where the arguments of the potential function formed a difference stencil for the second derivative.

3.4.2 Direct Expansion Technique

To preserve the higher order effects which are lost by the scaling technique as described in the previous section, it is necessary to omit the full thermodynamic limit, which drives the number N of atoms to infinity and therefore destroys all discreteness effects. Instead one has to consider a model within the quasi-continuum regime, i.e. for a large but fixed number N of atoms. The inner expansion technique described in Section 3.1 is one way to do so. Another way is given by the so-called direct expansion technique. It has been proposed by Kruskal and Zabusky [53, 85], Collins [22] and Rosenau [64, 65, 66] and is based on the Taylor expansion of the evolution equation of the atomistic system. The atomistic potential itself is not treated directly, but it is possible to reconstruct the continuum potential afterwards.

The method will now be shortly described for the atomic chain with the spring potential (2.7), for further details see [64]. According to Newton's second law of motion, the evolution equation reads as

$$m\frac{\partial^2}{\partial t^2}y(x) = \varphi'\big(y(x+1) - y(x)\big) - \varphi'\big(y(x) - y(x-1)\big) \qquad \forall x \in \mathcal{L} \cap \Omega, \tag{3.65}$$

where m denotes the mass of each atom. In terms of the discrete lattice width $z(x) := y(x) - y(x-1)$, it can be written as

$$m\frac{\partial^2}{\partial t^2}z(x) = \varphi'\big(z(x+1)\big) - 2\varphi'\big(z(x)\big) + \varphi'\big(z(x-1)\big). \tag{3.66}$$

Taylor expansion of $\varphi' \circ z$ around x leads to

$$m\frac{\partial^2}{\partial t^2}z(x) = L(\varphi' \circ z)(x) \tag{3.67}$$

with the infinite series of differential operators

$$L = 4\sinh^2\left(\frac{1}{2}\frac{\partial}{\partial x}\right) = \sum_{k=1}^{\infty}\frac{2}{(2k)!}\frac{\partial^{2k}}{\partial x^{2k}} = \frac{\partial^2}{\partial x^2} + \frac{1}{12}\frac{\partial^4}{\partial x^4} + \frac{1}{360}\frac{\partial^6}{\partial x^6} + \ldots \tag{3.68}$$

L is then truncated to the desired order.

For a chain of Hookean springs, i.e. $\varphi(r) = \frac{1}{2}(r-1)^2$ as in Example 1, and a truncation of L after the fourth derivative, this leads to

$$m\frac{\partial^2}{\partial t^2}z = \frac{\partial^2}{\partial x^2}z + \frac{1}{12}\frac{\partial^4}{\partial x^4}z. \tag{3.69}$$

Now, the quasi-continuum potential energy $\Phi^{(D)}$ can be reconstructed. For this purpose, we have to find a potential function from which the evolution equation results by computing the directional derivative and applying the discrete formula of partial integration. This leads to

$$\Phi^{(D)}(z) = \sum_{x \in \mathcal{L} \cap \Omega}\frac{1}{2}z'^2(x) - \frac{1}{24}z''^2(x). \tag{3.70}$$

Note that the atomistic evolution equation is rewritten in terms of the variable z in this approach. Thus the resulting equations are expressed in terms of the changed variable

z, which plays the role of the deformation gradient: $z \approx \partial y / \partial x$. Hence (3.69) does not correspond to an evolution equation for y, but to an evolution equation for its first spatial derivative.

In the example considered here, the simple pair potential depends on the difference $y(x) - y(x-1)$. Thus the change of variables from $y(x)$ to $z(x) = y(x) - y(x-1)$ allows to express the potential and its derivative in terms of a single variable, which then leads to the formulations (3.69) and (3.70). In principle, any translation invariant N-body potential can be written in terms of the differences of $N-1$ pairs of atom position. Thus, this approach should work for many-body potentials as well. However, the corresponding equations can then become quite involved.

Note furthermore that the coefficients of the series L of differential operators depend on the number of atoms. To analyze this dependence, the evolution equation (3.65) is scaled as in Section 3.4.1:

$$\varepsilon m \frac{\partial^2}{\partial t^2} y(x) = \varphi' \left(\frac{y(x+\varepsilon) - y(x)}{\varepsilon} \right) - \varphi' \left(\frac{y(x) - y(x-\varepsilon)}{\varepsilon} \right) \qquad \forall x \in \varepsilon \mathcal{L} \cap \Omega. \quad (3.71)$$

Here the mass of the atoms scales with ε to keep the total mass of the system constant. The difference equation is then rewritten in terms of the normalized lattice width $z(x) := \frac{y(x) - y(x-\varepsilon)}{\varepsilon}$ as

$$m \frac{\partial^2}{\partial t^2} z(x) = \frac{\varphi'(z(x+\varepsilon)) - 2\varphi'(z(x)) + \varphi'(z(x-\varepsilon))}{\varepsilon^2}. \quad (3.72)$$

Then, the Taylor expansion of $\varphi' \circ z$ leads to (3.67) with the differential operator

$$L = \sum_{k=1}^{\infty} \frac{2}{(2k)!} \varepsilon^{2k-2} \frac{\partial^{2k}}{\partial x^{2k}} = \frac{\partial^2}{\partial x^2} + \frac{\varepsilon^2}{12} \frac{\partial^4}{\partial x^4} + \frac{\varepsilon^4}{360} \frac{\partial^6}{\partial x^6} + \dots \quad (3.73)$$

Clearly the principal part $\partial^2 / \partial x^2$ remains unaffected by the scaling, but the higher order terms, i.e. the dispersion effects, are weighted by certain polynomials in ε. Their influence now depends on the specific choice of ε and is substantially reduced for $\varepsilon < 1$. They would completely vanish in the limit $\varepsilon \to 0$, which is consistent with the results of the scaling technique.

Let us remark a major drawback of the direct expansion technique: The evolution equation (3.69) is ill-posed, since the right-hand side is not a negative semidefinite operator in space. In other words, the equation lacks hyperbolicity. As a consequence, the potential energy dramatically blows up during the time evolution. This leads to an uncontrolled behavior of the solution, if the corresponding evolution equation can be solved at all. Contrary to this, the evolution equation of the original atomistic model is well-posed. The upscaling process by the direct expansion technique therefore must have destroyed essential properties of the atomistic model. A closer look at the continuum potential energy (3.70) shows that it is not bounded from below, although this holds for the original atomistic potential (2.7). Furthermore, the continuum potential is not convex, in contrast to its atomistic counterpart. Thus the direct expansion technique does not preserve these two important properties. This leads to the non-hyperbolicity of equation (3.69) and makes it ill-posed.

Note that if the differential operator L is truncated after the sixth-order term, the resulting evolution equation is well-posed by chance. We conclude from these observations
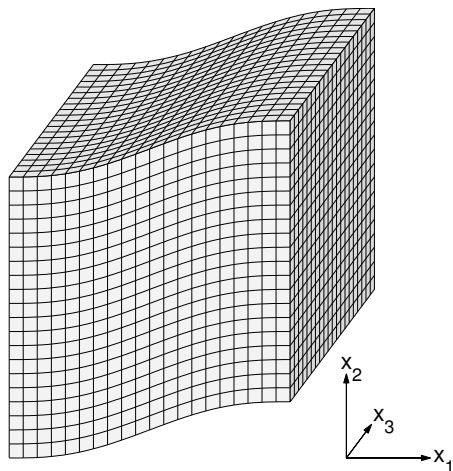
Figure 3.7: Deformation (3.81) for $\delta = 0.2$.

that an arbitrary truncation of L is sometimes feasible, but that it does not lead in general to a well-posed evolution equation.

Several ways to overcome this problem have been proposed. If (3.69) would be replaced by

$$m\frac{\partial^2}{\partial t^2}z = \frac{\partial^2}{\partial x^2}z - \frac{1}{12}\frac{\partial^4}{\partial x^4}z, \tag{3.74}$$

i.e. if the sign of the fourth order term would be altered, then the equation would be well-posed. This is known as the wrong sign problem, and (3.69) is denoted as the bad Boussinesq equation, see [64]. Another way to overcome this problem is to replace the Taylor series expansion of L by a more general Padé approximation, see e.g. [84] and [65, 66]. Sometimes these approximations lead to a well-posed evolution equation, but sometimes they do not. Thus, these approaches also do not satisfactorily correct the problems of the direct expansion technique.

3.5   Application to Crystalline Silicon

3.5.1   Upscaling of the Stillinger-Weber Potential

So far, we introduced the inner expansion technique, studied it for simple one-dimensional model problems and compared it to the scaling technique and the direct expansion technique. The inner expansion technique proved to be a useful technique to obtain a quasi-continuum description of the atomistic system, which avoids the drawbacks of the other methods. We now apply it to an atomistic model of crystalline silicon to see whether its advantages hold for this more realistic problem in three dimensions as well.

We apply the inner expansion technique in a straightforward but tedious calculation to the potential of Stillinger and Weber. To this end, the overall potential $\Phi^{(A)}$ from (2.37) is split into all two-body and three-body interactions. The expansion points $\overline{x}$ are chosen as $\overline{x} = \frac{1}{2}(x_1 + x_2)$ for the two-body terms and as $\overline{x} = \frac{1}{3}(x_1 + x_2 + x_3)$ for the three-body

terms. The Taylor series expansion with $K = 3$ of the term $y(x_2) - y(x_1)$ then reads as

$$y(x_2) - y(x_1) \approx (x_2 - x_1) \cdot \nabla y(\overline{x}) + \frac{1}{2} \left((x_2 - \overline{x})^2 - (x_1 - \overline{x})^2 \right) : \nabla^2 y(\overline{x})$$

$$+ \frac{1}{6} \left((x_2 - \overline{x})^3 - (x_1 - \overline{x})^3 \right) : \nabla^3 y(\overline{x}). \qquad (3.75)$$

For $y(x_3) - y(x_1)$ we obtain an analogous expression. We now substitute $z_2 := x_2 - x_1$ and $z_3 := x_3 - x_1$ to pass over to difference vectors. This way the expansion (3.75) is transformed to

$$T_{z_2}^1 := z_2 \cdot \nabla y(\overline{x}) + \frac{1}{24} z_2{}^3 : \nabla^3 y(\overline{x}) \qquad (3.76)$$

for the two-body terms and to

$$T_{z_2,z_3}^2 := z_2 \cdot \nabla y(\overline{x}) + \frac{1}{18} \left((2z_2 - z_3)^2 - (z_2 + z_3)^2 \right) : \nabla^2 y(\overline{x})$$

$$+ \frac{1}{162} \left((2z_2 - z_3)^3 + (z_2 + z_3)^3 \right) : \nabla^3 y(\overline{x}),$$

$$T_{z_2,z_3}^3 := z_3 \cdot \nabla y(\overline{x}) + \frac{1}{18} \left((2z_3 - z_2)^2 - (z_2 + z_3)^2 \right) : \nabla^2 y(\overline{x})$$

$$+ \frac{1}{162} \left((2z_3 - z_2)^3 + (z_2 + z_3)^3 \right) : \nabla^3 y(\overline{x}) \qquad (3.77)$$

for the three-body terms. These expressions are substituted into the atomistic potential. We eliminate the boundary effects by replacing the sums $\sum_{z_2,z_3 \in \mathcal{L} \cap \Omega - x_1}$ by the sums $\sum_{z_2,z_3 \in \mathcal{L}}$ over the full lattice. This leads to the continuum energy density

$$\Phi^{(\mathrm{I}),\overline{x}}(\nabla y, \nabla^2 y, \nabla^3 y)$$

$$= \sum_{z_2 \in \mathcal{L}} \varphi_2 \left(|T_{z_2}^1| \right) + \frac{1}{2} \sum_{z_2,z_3 \in \mathcal{L}} \varphi_3 \left(|T_{z_2,z_3}^2|, |T_{z_2,z_3}^3|, \frac{T_{z_2,z_3}^2 \cdot T_{z_2,z_3}^3}{|T_{z_2,z_3}^2||T_{z_2,z_3}^3|} \right) \qquad (3.78)$$

and the interpolated potential

$$\Phi^{(\mathrm{J})}(y) = \frac{1}{a_0{}^3} \int_\Omega \Phi^{(\mathrm{I}),\overline{x}}(\nabla y, \nabla^2 y, \nabla^3 y) \, d\overline{x}. \qquad (3.79)$$

The corresponding evolution equation is then given by

$$a_0{}^3 \rho \frac{\partial^2 y}{\partial t^2} = \operatorname{div} \frac{\partial \Phi^{(\mathrm{I}),\overline{x}}}{\partial \nabla y} - \operatorname{div}^2 \frac{\partial \Phi^{(\mathrm{I}),\overline{x}}}{\partial \nabla^2 y} + \operatorname{div}^3 \frac{\partial \Phi^{(\mathrm{I}),\overline{x}}}{\partial \nabla^3 y} \qquad \text{in } \Omega. \qquad (3.80)$$

To analyze how the quasi-continuum potential deviates from the original atomistic potential, we compute the potential energy on both the atomic level and the continuum mechanical level for the same system. We choose an atomistic system of 32768 atoms, where the atoms are arranged in the form of the diamond lattice and which is formed like a cube in the reference configuration. The system is embedded in a larger system of fixed atoms to constitute the Dirichlet-like boundary conditions as in the previous sections.

To obtain a nontrivial setting, the two opposite faces of the cube perpendicular to the x_1-axis are displaced by a shearing with a ratio δ ranging from 0 to 0.2. In-between, the deformation of the specimen is smoothly interpolated by

$$q(x_1, x_2, x_3) = (x_1, x_2 + \delta p(x_1), x_3). \qquad (3.81)$$

Here p denotes the fifth-order polynomial such that $p(0) = 0$, $p(L) = \delta$ and $p'(0) = p''(0) = p'(L) = p''(L) = 0$, where L is the length of the cube edges.

Now, the atomistic and the quasi-continuum potential for $K = 1, 2, 3$ is computed for each parameter δ. This is done separately for the two-body and three-body interactions. For the numerical quadrature of the integral in the quasi-continuum potential (3.7), a simple trapezoid rule with the cell size equivalent to one atomic cell is used. Of course more sophisticated quadrature schemes with larger cell sizes could be employed for higher computational efficiency. But here the simple scheme corresponds directly to the finite sum (3.4) and does not introduce an integration error. This allows to precisely evaluate the approximation quality of the expansion scheme and separate it from any integration error.

Hence we obtain values $\Phi_{B,\delta}^{(A)}$, $\Phi_{B,\delta,K}^{(I)}$ for $K = 1, 2, 3$, $\delta = 0 \ldots 0.2$ and $B = 2, 3$, where $B = 2$ denotes the two-body interactions and $B = 3$ the three-body interactions. In Figure 3.8, the absolute errors

$$\Phi_{B,\delta,K}^{(I)} - \Phi_{B,\delta}^{(A)} \tag{3.82}$$

are displayed. One can clearly see that the approximation for $K = 3$ is much better than for $K = 1$ and $K = 2$. Note furthermore that the curves for $K = 1$ and $K = 2$ coincide for the two-body potential. This is because the choice of the expansion point $\overline{x}$ as barycenter completely inhibits the dependency on the second derivative $\nabla^2 y$. Figure 3.8 also shows the relative error

$$\frac{\Phi_{B,\delta,K}^{(I)} - \Phi_{B,\delta}^{(A)}}{\Phi_{B,\delta}^{(A)} - \Phi_{B,0}^{(A)}}. \tag{3.83}$$

For $K = 1$ and $K = 2$, it is below 0.07% and 0.3%, respectively. For $K = 3$, it is even below 0.003% and 0.004%. Especially the three-body angle terms profit from an approximation order of $K = 3$, because bending effects are captured correctly then, whilst they are in part lost for $K \leq 2$.

Thus it seems to be reasonable to use an approximation order of $K = 3$ for the Stillinger-Weber potential. Note however that the influence of the higher order contributions depends on the size of the system. This influence gets successively smaller for an increasing number of atoms. For systems with a very high number of atoms, it can even be appropriate to use $K = 1$, since the higher order contributions are negligibly small then. But these contributions result in a qualitatively different behavior in the evolution equation as we have already seen in Section 3.2. Thus it is justified to incorporate them despite their quantitatively small contribution to the overall energy.

3.5.2 Dynamics of the Elastic Response

Now we consider the time evolution of a silicon crystal. According to the considerations in the previous subsection, we use the approximation order $K = 3$. The evolution is then governed by equation (3.80). We are interested in the elastic response of the crystal. To this end, we choose as initial value the deformation q as given by (3.81) with the deformation ratio $\delta = 0.1$, together with an initial velocity of zero. The boundary values are chosen in such a way that the specimen is embedded in an infinite bulk crystal which
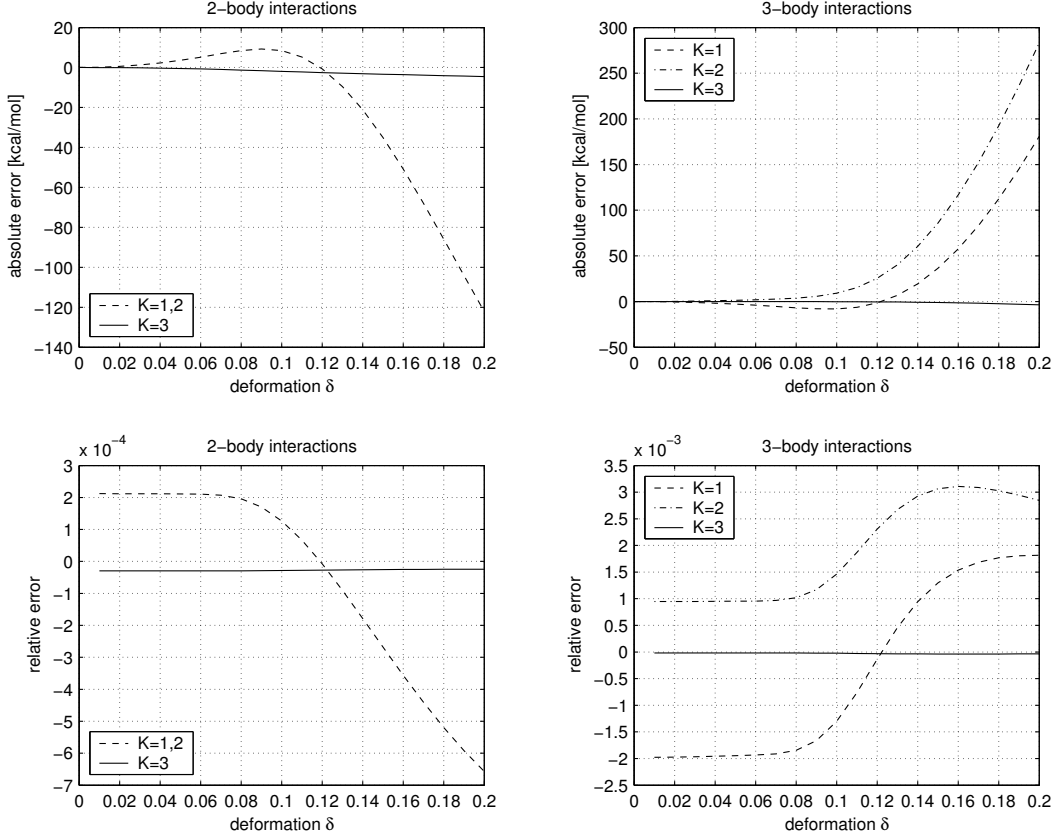
Figure 3.8: Absolute (top) and relative (bottom) errors of the Stillinger-Weber potential for the inner expansion technique. Left: two-body interactions (2.38), right: three-body interactions (2.39).

underwent the same deformation. Analogously to (3.20), this reads as

$$
\begin{aligned}
y(x,t) &= q(x), \\
\nabla_\nu y(x,t) &= \nabla_\nu q(x), \\
\nabla_\nu^2 y(x,t) &= \nabla_\nu^2 q(x) \qquad \forall x \in \partial\Omega, t > 0.
\end{aligned}
\tag{3.84}
$$

The spatial discretization of the continuum mechanical system is done by finite differences where we again exploit the divergence structure of the PDE as in the last section. This is even more important in the three-dimensional setting, since it considerably reduces the computational costs. In a first step, the discrete derivatives up to order three are computed. Then, in a second step, the discrete divergence operators are applied. For both steps, a difference stencil formed as the tensor product of one-dimensional five-point stencils is used. The stencils are consistent of order four for the first and second derivative and of order two for the third derivative. This ensures a sufficient accuracy. For the time discretization, an explicit Euler scheme is applied.

The dimensions are chosen such that each grid point of the finite difference discretization corresponds to $64^3 = 262,144$ atoms. We use $36^3 = 46,656$ grid points, hence the complete continuum system models 12,230,590,464 atoms. For the time step, a value of
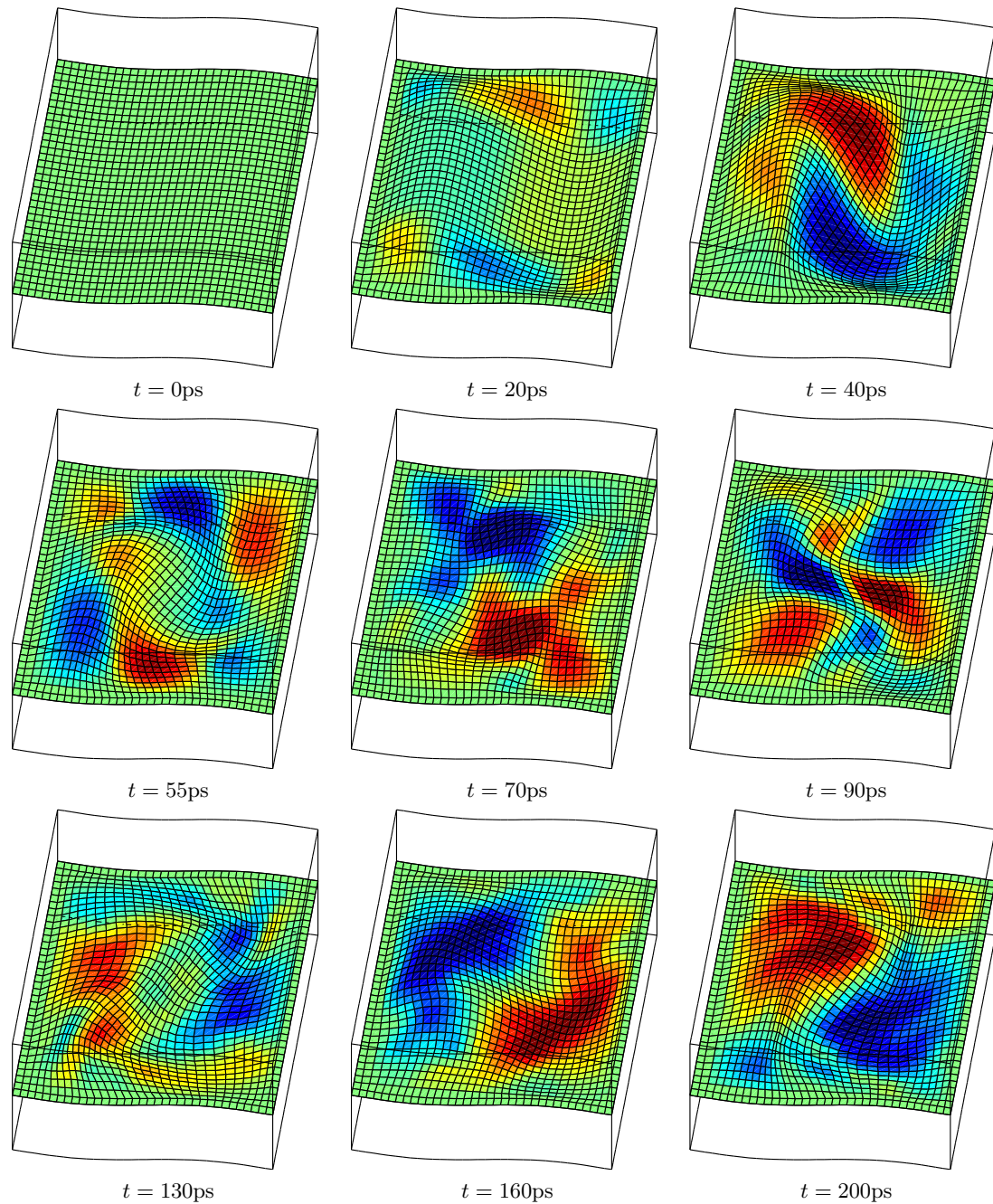
Figure 3.9: Elastic behavior of silicon. The cross section shows the displacement, magnified by the factor 8. The color denotes the velocity in the horizontally plotted x_1-direction.

0.2ps turned out to be sufficient for stability. This is substantially larger than the time step size of 1fs which is usually used for atomistic simulations.

Figure 3.9 shows the results of the simulation at different time steps. The plots show a planar cross section through the specimen. The associated displacement of the specimen

is visualized using a mesh. It is magnified by a factor of eight for better recognizability. The color indicates the velocity in the x_1-direction.

One can clearly observe how the system relaxes from its stressed initial configuration. The relaxation leads to eigenmode oscillations of the specimen. First, one can observe a basically circular movement of the whole inner part of the specimen. Later on, additional local oscillations with a higher frequency develop.

This particular simulation here is not only of interest because of its results, but it also represents a concrete example where a substantial improvement of computational efficiency is achieved by the averaged continuum description. The quasi-continuum model describes the discreteness effects of the original atomistic model. The discretized quasi-continuum model then inherits this discreteness, but the mesh size can be chosen much larger. Moreover, a much larger time step is sufficient. Therefore the quasi-continuum approach here allows us to address a problem which is too large to be solved on the atomic level. Nevertheless the discreteness properties from the microscale are properly incorporated by a meaningful choice of the approximation order. This way, the quasi-continuum model here serves as an averaging tool to pass from the original atomistic model to another discrete model with an arbitrary discretization size without losing the microscopic properties from the atomic level.

Chapter 4

Macroscopic Approximation

In the last chapter, we developed the inner expansion technique to derive a continuum mechanical model from an atomistic model. The continuum mechanical model describes the potential energy in terms of the derivatives of the deformation function up to a given order. We have shown that the atomistic system can be approximated to a high extent this way. The drawback of this technique is that the continuum potential is in general a very complex function, especially for multi-body interactions like the Stillinger-Weber potential or the Embedded-Atom Method. It can be computationally very time consuming to evaluate it.

Therefore we perform a next step in this chapter: The precise but complex continuum mechanical model is further approximated by another higher-order continuum mechanical model, which can be evaluated much faster, but which at the same time retains the important properties of the original potential.

First, we investigate mechanical invariances of the atomistic system and study how they transfer to the continuum mechanical level in Section 4.1. They help to reduce the complexity of the following approximations substantially. Then, the approximation techniques are discussed in detail. They are based on a decoupling of the different higher-order derivative terms.

The first-order derivative is addressed in Section 4.3. It forms the principal part which all common continuum mechanical models are based on. The approximation here employs an expansion around the energy wells in terms of the Cauchy strain tensor and the Young modulus. Accordingly, the approximation of the higher order part of the potential is discussed in Section 4.5.

As an application, we present the finite element simulations of the dynamics of one-way and two-way micro-actuators in Section 4.4. Such devices can cause small and precise movements and play an important role in the rapidly advancing field of nanotechnology.

4.1   Atomic and Continuum Mechanical Invariances

On the atomic level, the system exhibits several invariances. This means that many different atomic configurations lead to the same potential energy. These invariances include the rigid body motions and the symmetries which result from the underlying lattice. We analyze their structure and show how they are transferred to the continuum mechanical

level by the inner expansion technique. The results will be employed to simplify the description of the continuum mechanical potential later.

Every physically meaningful atomistic potential is invariant with respect to rigid body motions.[1] The latter are composed of translations, rotations and reflections. The simplest rigid body motions are the translations. The translational invariance for the localized atomistic potential $\Phi^{(A),\overline{x}}$ reads as

$$\Phi^{(A),\overline{x}}\left(\{y(x)+y_0\}_{x\in\mathcal{L}\cap\Omega}\right) = \Phi^{(A),\overline{x}}\left(\{y(x)\}_{x\in\mathcal{L}\cap\Omega}\right) \qquad \forall y_0 \in \mathbb{R}^d. \tag{4.1}$$

Not surprisingly it transforms to the continuum mechanical level as follows.

Lemma 4.1 *Let the atomistic potential $\Phi^{(A),\overline{x}}$ be translation invariant. Then the continuum mechanical energy density $\Phi^{(I),\overline{x}}(d_0, d_1, \ldots, d_K)$ does not depend on d_0.*

As a consequence, all derived quantities $\Phi^{(I)}$, $\Phi^{(J),\overline{x}}$ and $\Phi^{(J)}$ do not depend on this argument as well.

PROOF By definition of $\Phi^{(I),\overline{x}}$ we have

$$\begin{aligned}
\Phi^{(I),\overline{x}}(d_0, d_1, \ldots, d_K) &= \Phi^{(A),\overline{x}}\left(\left\{\sum_{k=0}^{K}\frac{1}{k!}(x-\overline{x})^k : d_k\right\}_{x\in\mathcal{L}\cap\Omega}\right) \\
&= \Phi^{(A),\overline{x}}\left(\left\{d_0 + \sum_{k=1}^{K}\frac{1}{k!}(x-\overline{x})^k : d_k\right\}_{x\in\mathcal{L}\cap\Omega}\right) \\
&\overset{(4.1)}{=} \Phi^{(A),\overline{x}}\left(\left\{\sum_{k=1}^{K}\frac{1}{k!}(x-\overline{x})^k : d_k\right\}_{x\in\mathcal{L}\cap\Omega}\right) \\
&= \Phi^{(I),\overline{x}}(0, d_1, \ldots, d_K). \tag{4.2}
\end{aligned}$$

Thus $\Phi^{(I),\overline{x}}(d_0, d_1, \ldots, d_K)$ does not depend on d_0. $\square$

Next, the rigid body motions contain rotations and reflections. Such motions can be described by a multiplication of the atom positions with a matrix $R \in O(d)$ from the left side.[2] The according invariance is denoted the frame indifference and thus reads as

$$\Phi^{(A)}(\{Ry(x)\}_{x\in\mathcal{L}\cap\Omega}) = \Phi(\{y(x)\}_{x\in\mathcal{L}\cap\Omega}) \qquad \forall R \in O(d). \tag{4.3}$$

Furthermore, the symmetry of the underlying lattice in crystals implies symmetry relations of the atomistic potential, the so-called lattice symmetries. The symmetry group $\mathcal{S} \subset O(d)$ of a lattice $\mathcal{L}$ is defined by

$$\mathcal{S} := \{S \in O(d) : S\mathcal{L} = \mathcal{L}\}. \tag{4.4}$$

---

[1]Boundary conditions can restrict the rigid body motions. But this is essentially a matter of constricting the set of admissible deformations and not of the potential energy itself, compare to the construction of the ghost atoms in Chapter 2. Hence it is justified to disregard this point here.

[2]Actually, a reflection cannot be attained by a smooth deformation, since this would require an intermediate singular deformation of the body due to continuity. Nevertheless it is common to include them in the notion of frame indifference, see e.g. [61]. We follow this convention here. Otherwise (4.3) would be required to hold for all $R \in SO(d)$ only.

Hence $\mathcal{S}$ just contains those matrices S which transfer the lattice back to itself.[3]

   Because atoms of the same type are not distinguished by the potential energy, a deformation y applied to the lattice which is transformed by S possesses the same potential energy as the deformation y applied to the original lattice. Precisely this reads as follows: The atom configuration $\{y(Sx) : x \in \mathcal{L} \cap S^{-1}\Omega\}$ possesses the same potential energy as the original atom configuration $\{y(x) : x \in \mathcal{L} \cap \Omega\}$. Because $\mathcal{S} \subset O(d)$, the frame indifference (4.3) allows us to transform back afterwards without changing the potential. Of course, the center point $\overline{x}$ of the localized potential must be transformed to $S\overline{x}$ as well. Hence the lattice symmetry reads as

$$\forall S \in \mathcal{S} : \qquad \Phi^{(A),\overline{x}}(\{S^T y(Sx)\}_{x \in \mathcal{L} \cap S^{-1}\Omega}) = \Phi^{(A),S\overline{x}}(\{y(x)\}_{x \in \mathcal{L} \cap \Omega}). \qquad (4.5)$$

Note that the lattice symmetry is automatically fulfilled for the formulation of the atomistic potential energy used here, because the notation $\{y(x)\}_{x \in \mathcal{L} \cap \Omega}$ as an indexed set and $S\mathcal{L} = \mathcal{L}$ immediately imply $\{y(x)\}_{x \in \mathcal{L} \cap \Omega} = \{y(x)\}_{x \in S\mathcal{L} \cap \Omega}$. In other formulations used by other authors the lattice symmetry has to be postulated explicitly.

   Both the frame indifference and the lattice symmetry can be expressed together as

Lemma 4.2 *(Frame indifference and lattice symmetry) The atomistic potential* $\Phi^{(A),\overline{x}}$ *fulfills*

$$\forall R \in O(d), S \in \mathcal{S} : \qquad \Phi^{(A),\overline{x}}(\{Ry(Sx)\}_{x \in \mathcal{L} \cap S^{-1}\Omega}) = \Phi^{(A),S\overline{x}}(\{y(x)\}_{x \in \mathcal{L} \cap \Omega}). \qquad (4.6)$$

   Now we analyze how these symmetries transfer to the continuum mechanical level. To this end, the transformations by $R \in O(d)$ and $S \in \mathcal{S}$ are expressed by the functions r and s which are defined by

$$\begin{aligned} r : \mathbb{R}^d \to \mathbb{R}^d, \qquad r(x) = Rx, \\ s : \mathbb{R}^d \to \mathbb{R}^d, \qquad s(x) = Sx. \end{aligned} \qquad (4.7)$$

The atomic frame indifference and lattice symmetry (4.6) can now be stated as

$$\Phi^{(A),\overline{x}}(\{(r \circ y \circ s)(x)\}_{x \in \mathcal{L} \cap S^{-1}\Omega}) = \Phi^{(A),S\overline{x}}(\{y(x)\}_{x \in \mathcal{L} \cap \Omega}). \qquad (4.8)$$

With this notation, the invariances transfer to the continuum mechanical level as follows:

Lemma 4.3 *Let the atomistic potential* $\Phi^{(A),\overline{x}}$ *fulfill the requirement of frame indifference and lattice symmetry (4.6). Then the continuum mechanical potential* $\Phi^{(I),\overline{x}}$ *obtained by the inner expansion technique obeys*

$$\Phi^{(I),\overline{x}}(r \circ y \circ s, \ldots, \nabla^K(r \circ y \circ s)) = \Phi^{(I),S\overline{x}}(y, \ldots, \nabla^K y). \qquad (4.9)$$

PROOF The k-th derivative of the l-th component of $r \circ y \circ s$ with respect to the coordinates $x_{i_1}, x_{i_2}, \ldots, x_{i_k}$ computes to

$$\frac{\partial^k(r^l \circ y \circ s)}{\partial x_{i_1} \partial x_{i_2} \cdots \partial x_{i_k}} = \sum_{j=1}^d \sum_{j_1,j_2,\ldots,j_k=1}^d R_{lj}(y^j_{,j_1,j_2,\ldots,j_d} \circ s)S_{j_1 i_1} S_{j_2 i_2} \cdots S_{j_d i_d}. \qquad (4.10)$$

---

[3]Here we assume that the base cell $\mathcal{L}_{\text{cell}}$ does not contain a translational offset. Otherwise an additional translation has to be applied in the definition (4.4). Due to the translational invariance (4.1), this does not affect the subsequent argumentation.

Thus we get

$$\Phi^{(\mathrm{I}),\overline{x}}(r \circ y \circ s)$$

$$= \Phi^{(\mathrm{A}),\overline{x}}\Bigg(\Bigg\{\sum_{k=0}^{K}\frac{1}{k!}\sum_{i_1,i_2,\ldots,i_k=1}^{d}(r \circ y \circ s)_{,i_1,i_2,\ldots,i_k}(\overline{x})$$

$$\cdot (x-\overline{x})_{i_1}(x-\overline{x})_{i_2}\cdots(x-\overline{x})_{i_k}\Bigg\}_{x\in\mathcal{L}\cap S^{-1}\Omega}\Bigg)$$

$$= \Phi^{(\mathrm{A}),\overline{x}}\Bigg(\Bigg\{\sum_{k=0}^{K}\frac{1}{k!}\sum_{i_1,i_2,\ldots,i_k=1}^{d}\sum_{j_1,j_2,\ldots,j_k=1}^{d}R\cdot y_{,j_1,j_2,\ldots,j_d}(S\overline{x})\cdot S_{j_1i_1}S_{j_2i_2}\cdots S_{j_di_d}$$

$$\cdot (x-\overline{x})_{i_1}(x-\overline{x})_{i_2}\cdots(x-\overline{x})_{i_k}\Bigg\}_{x\in\mathcal{L}\cap S^{-1}\Omega}\Bigg)$$

$$= \Phi^{(\mathrm{A}),\overline{x}}\Bigg(\Bigg\{R\sum_{k=0}^{K}\frac{1}{k!}\sum_{j_1,j_2,\ldots,j_k=1}^{d}y_{,j_1,j_2,\ldots,j_d}(S\overline{x})$$

$$\cdot (Sx-S\overline{x})_{j_1}(Sx-S\overline{x})_{j_2}\cdots(Sx-S\overline{x})_{j_k}\Bigg\}_{x\in\mathcal{L}\cap S^{-1}\Omega}\Bigg)$$

$$\overset{(*)}{=} \Phi^{(\mathrm{A}),S\overline{x}}\Bigg(\Bigg\{\sum_{k=0}^{K}\frac{1}{k!}\sum_{j_1,j_2,\ldots,j_k=1}^{d}y_{,j_1,j_2,\ldots,j_d}(S\overline{x})$$

$$\cdot (x-S\overline{x})_{j_1}(x-S\overline{x})_{j_2}\cdots(x-S\overline{x})_{j_k}\Bigg\}_{x\in S\mathcal{L}\cap\Omega}\Bigg)$$

$$= \Phi^{(\mathrm{I}),S\overline{x}}(y). \tag{4.11}$$

The equality $(*)$ is obtained by applying (4.6), in which y has been replaced by its Taylor expansion. $\square$

4.2   Decoupling of the Continuum Mechanical Potential

After the invariances of the continuum mechanical potential $\Phi^{(\mathrm{I}),\overline{x}}$ have been studied, the dependence on the different arguments $d_0, d_1, d_2, \ldots, d_K$ of the potential is now decoupled. This allows to handle the resulting terms independently in the subsequent sections.

First, Lemma 4.1 allows us to skip the parameter d_0 completely, because the potential does not depend on it at all. Then, the remaining potential energy density $\Phi^{(\mathrm{I}),\overline{x}}(d_1, d_2, \ldots, d_K)$ is expanded up to order two, but only in the variables $d_2, \ldots, d_K$ and not in d_1. This gives

$$\Phi^{(\mathrm{I}),\overline{x}}(d_1, d_2, \ldots, d_K) \approx \Phi^{(\mathrm{I}),\overline{x}}(d_1, 0, \ldots, 0) + \sum_{k=2}^{K}\Phi^{(\mathrm{I}),\overline{x}}_{,d_k}(d_1, 0, \ldots, 0) : d_k$$

$$+ \frac{1}{2}\sum_{k=2}^{K}\sum_{l=2}^{K}\Phi^{(\mathrm{I}),\overline{x}}_{,d_k,d_l}(d_1, 0, \ldots, 0) : d_k : d_l. \tag{4.12}$$

To further simplify this expression, we make use of the following considerations. Each mechanical system tends to minimize the potential energy. For the time evolution of such a system, this tendency is expressed by Newton's second law of motion, which states that the acceleration always points towards the direction of steepest descent of the potential energy. In the stationary setting, one even imposes the minimization of the potential energy as the governing principle. As a consequence, the system stays nearby the minima of the energy landscape, except for extreme outer conditions. Thus it makes most sense to approximate the energy landscape in the vicinity of the minima of the potential energy.

At each minimum, the first derivatives $\Phi_{d_k}^{(\mathrm{I}),\overline{x}}$ of the energy density vanish as a necessary condition. Nearby such a minimum, these derivatives are at least small. Thus it is reasonable to neglect them. (4.12) then simplifies to

$$\Phi^{(\mathrm{I}),\overline{x}}(d_1, d_2, \ldots, d_K) \approx \Phi^{(\mathrm{I}),\overline{x}}(d_1, 0, \ldots, 0) + \frac{1}{2} \sum_{k=2}^{K} \sum_{l=2}^{K} \Phi_{,d_k,d_l}^{(\mathrm{I}),\overline{x}}(d_1, 0, \ldots, 0) : d_k : d_l. \quad (4.13)$$

The term $\Phi^{(\mathrm{I}),\overline{x}}(d_1, 0, \ldots, 0)$ is called the principal part and will be addressed in Section 4.3. The remaining terms are higher order contributions and will be discussed in Section 4.5.

4.3   Approximation of the Principal Part

This section is devoted to the approximation of the principal part $\Phi^{(\mathrm{I}),\overline{x}}(d_1, 0, \ldots, 0)$. The principal part only depends on the first order gradient $d_1 = \nabla y(\overline{x})$ of the deformation. In most of the literature about continuum mechanics, this deformation gradient is denoted by F. We follow the convention in this section. Thus we have

$$d_1 = \nabla y(\overline{x}) = F. \quad (4.14)$$

To shorten notation, we write

$$\Phi^P(F) = \Phi^{(\mathrm{I}),\overline{x}}(F, 0, \ldots, 0) \quad (4.15)$$

for the continuum mechanical energy density. Thus the principal part of the overall potential is given by

$$\int_\Omega \Phi^P(\nabla y(\overline{x})) \, \mathrm{d}\overline{x}. \quad (4.16)$$

As already mentioned before, the subsequent approximation will be done in the vicinity of the minima of the potential energy. We first identify the precise location of the minima in Section 4.3.1. Then, the actual approximation is carried out in Section 4.3.2.

4.3.1   Identification of the Wells

In this section, the minima of the principal part $\Phi^P(F)$ of the potential energy will be identified. Unfortunately, it turns out that there is an infinite number of such minima. Therefore a classification is in order first.

According to Lemma 4.3, the frame indifference of the potential states that if F is a minimum of Φ^P, then RF for all $R \in O(d)$ is a minimum as well. Thus the set of minima

consists of the union of orbits $O(d)F = \{RF : R \in O(d)\}$. Each orbit is called a well, and F is a representative of that well. For each well, let W_i denote a representative. Then the set of minima has the form

$$\bigcup_i O(d)W_i. \tag{4.17}$$

Hence it suffices to identify one representative W_i of each well.

Since every element of the well $O(d)W_i$ can serve as a representative, it is convenient to prescribe a normal form. The polar decomposition assures the existence of a nice normal form, which later turns out to be useful.

Lemma 4.4 *(Polar decomposition) For every matrix $F \in \mathbb{R}^{d \times d}$ there exist a matrix $R \in O(d)$ and a uniquely determined symmetric positive semidefinite matrix $U \in \mathbb{R}^{d \times d}$ such that*

$$F = RU. \tag{4.18}$$

If in addition $F \in GL(d, \mathbb{R})$, then R is also uniquely determined and U is symmetric positive definite.

The proof can be found in any textbook about linear algebra, see e.g. [44]. As a consequence of the polar decomposition, each well contains exactly one representative which is symmetric positive definite. We choose this representation as our normal form.

Now we are ready to actually find the minima. Since the complexity of the potential inhibits to address this problem analytically, we do so numerically. To this end, a program has been developed to determine the specific potential energy and its derivatives of a bulk nickel-aluminum crystal which is deformed by a matrix F.

The program works as follows. First, the base cell $\mathcal{L}_{\text{cell}}$ is generated. For the B2 lattice of the reference configuration here, it consists of two atoms A and B with positions x_A and x_B, compare (2.52). The lattice constant is chosen as $a_0 = 2.985\text{Å}$, such that the austenitic phase is situated at $F = I$.[4] Then the full lattice is generated by a translation of the atoms A and B along the base cell. This is done separately for the two atoms, such that we obtain two different sublattices which are generated by A and B, respectively. Finally, the whole lattice is homogeneously deformed by a multiplication by F, i.e. each point $x \in \mathcal{L}$ is moved to $y(x) = Fx$.

Now the potential energy can be computed. According to (2.48), the potential corresponding to the two atoms in the base cell is given by

$$\sum_{x \in \mathcal{L}} \frac{1}{2} \left(\Phi^{\text{pair}}(|y(x) - y(x_A)|) + \Phi^{\text{pair}}(|y(x) - y(x_B)|) \right)$$
$$+ \Phi^{\text{emb}}(\rho_A^{\text{host}}) + \Phi^{\text{emb}}(\rho_B^{\text{host}}). \tag{4.19}$$

Here the different types of the involved atoms have to be taken into account, since they determine the parameters of the potential. The fractions of nickel and aluminum in the crystal are given by $\mu = 0.64$ and $1 - \mu = 0.36$, respectively. As already discussed in Chapter 2, sublattice A consists of nickel atoms only, whereas sublattice B consists of

---

[4]Actually, a guessed value has been used first. The critical point of Φ^P at which the austenitic phase is located has then been determined by the program itself. The precise value of a_0 has been adjusted afterwards such that the critical point is located at $F = I$.

randomly placed nickel and aluminum atoms. Thus on sublattice B, the fractions of nickel and aluminum are $2\mu - 1$ and $2 - 2\mu$, respectively.

For the pair interaction, there are three combinations of atom types: Ni-Ni, Ni-Al and Al-Al. The corresponding interaction functions $\Phi^{\text{pair}}_{\text{NiNi}}$, $\Phi^{\text{pair}}_{\text{NiAl}}$ and $\Phi^{\text{pair}}_{\text{AlAl}}$ are added according to their frequency of appearance:

sublattice combination	interaction
A – A	$\Phi^{\text{pair}} = \Phi^{\text{pair}}_{\text{NiNi}}$
A – B	$\Phi^{\text{pair}} = (2\mu - 1)\Phi^{\text{pair}}_{\text{NiNi}} + (2 - 2\mu)\Phi^{\text{pair}}_{\text{NiAl}}$
B – B	$\Phi^{\text{pair}} = (2\mu - 1)^2\Phi^{\text{pair}}_{\text{NiNi}} + 2(2\mu - 1)(2 - 2\mu)\Phi^{\text{pair}}_{\text{NiAl}} + (2 - 2\mu)^2\Phi^{\text{pair}}_{\text{AlAl}}$

For the embedding energy, we proceed similarly. The electron density of each atom A or B in the host is given by

$$\rho^{\text{host}}_{\text{A/B}} = \sum_{x \in \mathcal{L}} \rho^{\text{atom}}(|y(x) - y(x_{\text{A/B}})|). \qquad (4.20)$$

Here the density ρ^{atom} depends on the type of atom x and is given by

sublattice of atom x	electron density
A	$\rho^{\text{atom}} = \rho^{\text{atom}}_{\text{Ni}}$
B	$\rho^{\text{atom}} = (2\mu - 1)\rho^{\text{atom}}_{\text{Ni}} + (2 - 2\mu)\rho^{\text{atom}}_{\text{Al}}$

Then the embedding function Φ^{emb} is applied. It depends on the type of the atom x_{A} or x_{B} and is given by

sublattice of atom $x_{\text{A/B}}$	embedding function
A	$\Phi^{\text{emb}} = \Phi^{\text{emb}}_{\text{Ni}}$
B	$\Phi^{\text{emb}} = (2\mu - 1)\Phi^{\text{emb}}_{\text{Ni}} + (2 - 2\mu)\Phi^{\text{emb}}_{\text{Al}}$

Finally, the so-computed pair potential and the embedding potential are summed up and divided by the volume of the base cell. This gives the specific energy $\Phi^P(F)$ per unit volume.

We now have a program at our disposal to compute the potential energy and its derivatives for the nickel-aluminum alloy at zero temperature. We use it to identify the local minima of the potential energy. To this end, it is sufficient to restrict ourselves to the region of attainable deformations. A deformation is attainable if it does not differ too much from the reference configuration. Otherwise it will not be found anyway during the time evolution of real alloys.[5] Here a deformation F is called attainable if it differs from the identity deformation only by an entry-wise perturbation of 0.25 at maximum, i.e. if $|F_{ij} - \delta_{ij}| \leq 0.25$ for all i, j.

For the minimum search, we employ a Monte Carlo technique followed by a local minimization algorithm. First, we choose an attainable random start point. Then the energy Φ^P is minimized by a steepest descent algorithm with an Armijo step-size control. This is repeated until the gradient gives no further descent due to the finite machine precision. We end up with a local minimum F. Then we split F into the product $F =$

---

[5] This concept has been formalized in terms of the so-called Ericksen-Pitteri or weak transformation neighborhoods, see [61].

local minimum $F = RW$	number of occurrences
$W_1 = \begin{pmatrix} 1.2256 & 0 & 0 \\ 0 & 0.89522 & 0 \\ 0 & 0 & 0.89522 \end{pmatrix}$	658,673
$W_2 = \begin{pmatrix} 0.89522 & 0 & 0 \\ 0 & 1.2256 & 0 \\ 0 & 0 & 0.89522 \end{pmatrix}$	654,655
$W_3 = \begin{pmatrix} 0.89522 & 0 & 0 \\ 0 & 0.89522 & 0 \\ 0 & 0 & 1.2256 \end{pmatrix}$	654,786
unattainable	31,886

Table 4.1: Results of the Monte Carlo search for local minima of the potential energy. The minima are classified into the set of wells.

RW of an orthogonal and a symmetric positive definite matrix by means of the polar decomposition.[6]

We performed the search procedure 2,000,000 times. This ensures that the whole space of attainable deformations is suitably sampled. The results are given in Table 4.1. Some entries had to be removed, because the algorithm converged to an unattainable deformation with a deformation ratio of ≥ 1.4 in one direction. Note that the austenitic well $W_0 = I$ cannot be found by the minimum search, because we are at zero temperature.[7] This resembles the fact that the austenite does not occur at low temperatures.

One can clearly see that the set of minima is given by the union of the three different wells represented by

$$W_1 = \begin{pmatrix} \beta & 0 & 0 \\ 0 & \alpha & 0 \\ 0 & 0 & \alpha \end{pmatrix}, \qquad W_2 = \begin{pmatrix} \alpha & 0 & 0 \\ 0 & \beta & 0 \\ 0 & 0 & \alpha \end{pmatrix}, \qquad W_3 = \begin{pmatrix} \alpha & 0 & 0 \\ 0 & \alpha & 0 \\ 0 & 0 & \beta \end{pmatrix} \qquad (4.21)$$

where $\alpha = 0.89522$ and $\beta = 1.2256$. The three wells correspond to the three variants of the martensitic phase. Note that the corresponding deformations are nearly volume-preserving, since $\det W_1 = \det W_2 = \det W_3 = \alpha^2 \beta \approx 0.98222$ is nearby of 1.

All three wells describe deformations in which the specimen is stretched along one axis by the factor $\beta > 1$, while the other two axes are compressed by the factor $\alpha < 1$. The transformation corresponding to these wells is called a tetragonal transformation.[8] As already described in Section 2.3.3, the deformations transform the body-centered cubic (bcc) lattice into a face-centered lattice. Since the ratio $\beta/\alpha \approx 1.36905$ differs from $\sqrt{2} \approx$

---

[6]For this specific potential, the matrix W always turns out to be diagonal. In this case the polar decomposition coincides with the QR factorization.

[7]Actually, Φ^P has a critical point at I. But the Hessian matrix is indefinite, such that I is a saddle point which cannot be found by the minimization algorithm.

[8]An overview of all possible transformations can be found in [61].

1.41421, the target lattice is not face-centered cubic (fcc), but face-centered tetragonal (fct).

Note furthermore that the three wells exhibit even more structure. They are not completely different, but related to each other. Each representative W_i emerges from each other by a permutation of the axes. For example, W_2 is obtained from W_1 by exchanging the x_1- and the x_2-axis, and W_3 is obtained from W_1 by exchanging the x_1- and the x_3-axis.

The underlying structure behind this relationship is the lattice symmetry. As shown in Lemma 4.3, the potential fulfills

$$\Phi^P(S^T F S) = \Phi^P(F) \qquad \forall S \in \mathcal{S}. \tag{4.22}$$

Consequently, if W is a minimum of the potential energy, so is $S^T F S$ for all $S \in \mathcal{S}$. In our application of the nickel-aluminum alloy, the symmetry group $\mathcal{S}$ of the bcc/B2 lattice is given by

$$\mathcal{S} = \left\{ \begin{pmatrix} \pm 1 & 0 & 0 \\ 0 & \pm 1 & 0 \\ 0 & 0 & \pm 1 \end{pmatrix}, \begin{pmatrix} 0 & \pm 1 & 0 \\ 0 & 0 & \pm 1 \\ \pm 1 & 0 & 0 \end{pmatrix}, \begin{pmatrix} 0 & 0 & \pm 1 \\ \pm 1 & 0 & 0 \\ 0 & \pm 1 & 0 \end{pmatrix}, \right.$$
$$\left. \begin{pmatrix} \pm 1 & 0 & 0 \\ 0 & 0 & \pm 1 \\ 0 & \pm 1 & 0 \end{pmatrix}, \begin{pmatrix} 0 & 0 & \pm 1 \\ 0 & \pm 1 & 0 \\ \pm 1 & 0 & 0 \end{pmatrix}, \begin{pmatrix} 0 & \pm 1 & 0 \\ \pm 1 & 0 & 0 \\ 0 & 0 & \pm 1 \end{pmatrix} \right\}. \tag{4.23}$$

Now, the set $\{S^T W_i S : S \in \mathcal{S}\}$ for all $i = 1, 2, 3$ exactly coincides with the set $\{W_1, W_2, W_3\}$ of the wells, which explains the above mentioned relationship. For example, for

$$S_1 = \begin{pmatrix} 0 & 1 & 0 \\ 1 & 0 & 0 \\ 0 & 0 & 1 \end{pmatrix} \qquad \text{and} \qquad S_2 = \begin{pmatrix} 0 & 0 & 1 \\ 0 & 1 & 0 \\ 1 & 0 & 0 \end{pmatrix} \tag{4.24}$$

we have $S_1^T W_1 S_1 = W_2$ and $S_2^T W_1 S_2 = W_3$.

Furthermore, the potential energy coincides in the vicinity of all three orbits due to (4.22) as well. Thus it suffices to restrict ourselves to one of the three martensitic wells in the following section, where the potential will be studied nearby the wells. The results can then be transferred to the other martensitic wells by means of (4.22).

Beyond the martensitic wells W_1, W_2 and W_3, there is the austenitic well. It cannot be found by the minimization algorithm, because the function Φ^P describes the potential energy at zero temperature, whereas the austenitic phase occurs only at high temperatures, as we have seen in the atomistic simulations in Section 2.3.3. Because we defined the reference configuration in such a way that it reflects the austenitic phase, the austenitic well is situated at

$$W_0 = I. \tag{4.25}$$

Of course the austenitic well exhibits the same invariances of frame indifference and lattice symmetry as the martensitic wells.

4.3.2 Young Modulus

After we identified and classified the wells, we now approximate the potential energy around these wells. The symmetry of the system allows to reduce the degrees of freedom for this considerably. Therefore we first rewrite the energy in terms of the so-called strain tensor.

The requirement of frame indifference (4.9) constricts the form of the potential energy. Indeed, the potential energy cannot depend on the deformation gradient $F = \nabla y$ in an arbitrary way. Instead, it in fact depends only on the so-called Green strain tensor (or shortly strain tensor)

$$\varepsilon := \frac{1}{2}\left(\nabla y^T \nabla y - I\right) = \frac{1}{2}\left(F^T F - I\right), \tag{4.26}$$

as stated in the next lemma. Note that the strain tensor ε is symmetric and frame indifferent.

Lemma 4.5 *Let $\Phi : \mathbb{R}^{d \times d} \to \mathbb{R}$ be a frame indifferent function, i.e. assume that*

$$\Phi(F) = \Phi(RF) \tag{4.27}$$

for all $F \in \mathbb{R}^{d \times d}$ and $R \in O(d)$. Then there exists a function $\hat{\Phi} : \mathbb{R}^{d \times d}_{sym} \to \mathbb{R}$ such that

$$\Phi(F) = \hat{\Phi}(\varepsilon), \tag{4.28}$$

where ε and F are related to each other by (4.26). Here $\mathbb{R}^{d \times d}_{sym}$ denotes the set of real symmetric $d \times d$-matrices.

PROOF According to Lemma 4.4, F can be decomposed into $F = \tilde{R}U$, where $\tilde{R} \in O(d)$ and U is symmetric positive semidefinite. Applying the frame indifference with $R = \tilde{R}^{-1}$ leads to

$$\Phi(F) = \Phi(\tilde{R}U) = \Phi(R\tilde{R}U) = \Phi(U). \tag{4.29}$$

Hence Φ depends on U only. Because $2\varepsilon + I = F^T F = U^T U$ is symmetric positive semidefinite, it possesses the unique square root $U = \sqrt{U^T U} = \sqrt{2\varepsilon + I}$. Thus we can define

$$\hat{\Phi}(\varepsilon) := \Phi(\sqrt{2\varepsilon + I}) = \Phi(U), \tag{4.30}$$

which proves the lemma. $\qquad\square$

Now, after we have rewritten the potential in terms of the strain tensor, we approximate the potential in the vicinity of the wells. We start with the austenitic well $W_0 = I$ at $\varepsilon = 0$. To this end, we perform the Taylor series expansion of the energy $\hat{\Phi}^P(\varepsilon)$ with respect to the strain tensor ε:

$$\hat{\Phi}^P(\varepsilon) \approx \hat{\Phi}^P(0) + \varepsilon_{ij}\hat{\Phi}^P_{,ij}(0) + \frac{1}{2}\varepsilon_{ij}\varepsilon_{kl}\hat{\Phi}^P_{,ij,kl}(0) + \dots \tag{4.31}$$

Here and in the following we use the Einstein summation convention to simplify notation: The sum is taken over all indices which appear twice. The term $\hat{\Phi}^P(0)$ is just a constant and will be named c_A. Here the subscript A indicates the austenitic well. The first order

term vanishes, because $\varepsilon = 0$ is a critical point of the energy. Thus the second order term is the most decisive one. The coefficients are called the Young modulus $\mathbb{C}^{\mathrm{A}}$:

$$\mathbb{C}^{\mathrm{A}}_{ijkl} := \frac{\partial^2}{\partial \varepsilon_{ij} \partial \varepsilon_{kl}} \hat{\Phi}^P \bigg|_{\varepsilon=0}. \tag{4.32}$$

They also determine the frequency of the natural oscillations of the crystal.

It is usually sufficient to truncate the expansion after the quadratic terms. This corresponds to the mostly used description of the potential energy in common continuum mechanics, see e.g. Ericksen [34] and [35]. Altogether, we yield the approximation of the energy around the austenite

$$\hat{\Phi}^P(\varepsilon) \approx c_A + \frac{1}{2} \varepsilon_{ij} \varepsilon_{kl} \mathbb{C}^{\mathrm{A}}_{ijkl}. \tag{4.33}$$

In the three-dimensional setting $d = 3$, there are $3^4 = 81$ coefficients $\mathbb{C}^{\mathrm{A}}_{ijkl}$. But due to the symmetry of the strain tensor, $\mathbb{C}^{\mathrm{A}}$ fulfills

$$\mathbb{C}^{\mathrm{A}}_{ijkl} = \mathbb{C}^{\mathrm{A}}_{jikl} = \mathbb{C}^{\mathrm{A}}_{ijlk} = \mathbb{C}^{\mathrm{A}}_{jilk} \tag{4.34}$$

for all $i, j, k, l = 1, 2, \ldots, d$. As a consequence, the number of possibly different values reduces from $9 \times 9 = 81$ to $6 \times 6 = 36$ for $d = 3$. Furthermore, the symmetry of the second derivative (assuming that $\hat{\Phi}^P$ is smooth) leads to

$$\mathbb{C}^{\mathrm{A}}_{ijkl} = \mathbb{C}^{\mathrm{A}}_{klij} \tag{4.35}$$

for all i, j, k, l. This further reduces the number of possibly different values to $6 \times (6+1)/2 = 21$ for $d = 3$. Thus the changeover from the deformation gradient $F = \nabla y$ to the strain tensor ε reduces the number of coefficients $\mathbb{C}^{\mathrm{A}}_{ijkl}$ to be handled from 81 to 21.

To actually compute the Young modulus $\mathbb{C}^{\mathrm{A}}$ later, we need to express it in terms of Φ^P instead of $\hat{\Phi}^P$. This is done as follows. We have

$$\frac{\partial \varepsilon_{mn}}{\partial F_{ij}} = \frac{1}{2} \left(F_{im} \delta_{jn} + F_{in} \delta_{jm} \right). \tag{4.36}$$

Thus it follows that

$$\begin{aligned}
\frac{\partial^2 \Phi^P}{\partial F_{ij} \partial F_{kl}} \bigg|_{F=I} &= \frac{\partial}{\partial F_{ij}} \left[\frac{\partial \hat{\Phi}^P}{\partial \varepsilon_{pq}} \frac{\partial \varepsilon_{pq}}{\partial F_{kl}} \right]_{F=I} = \left[\frac{\partial^2 \hat{\Phi}^P}{\partial \varepsilon_{mn} \partial \varepsilon_{pq}} \frac{\partial \varepsilon_{mn}}{\partial F_{ij}} \frac{\partial \varepsilon_{pq}}{\partial F_{kl}} + \frac{\partial \hat{\Phi}^P}{\partial \varepsilon_{pq}} \frac{\partial^2 \varepsilon_{pq}}{\partial F_{ij} \partial F_{kl}} \right]_{F=I} \\
&= \frac{1}{4} \hat{\Phi}^P_{,mn,pq}(0) \left(F_{im} \delta_{jn} + F_{in} \delta_{jm} \right) \left(F_{kp} \delta_{lq} + F_{kq} \delta_{lp} \right) \bigg|_{F=I} + 0 \\
&= \frac{1}{4} \hat{\Phi}^P_{,mn,pq}(0) \left(\delta_{im} \delta_{jn} + \delta_{in} \delta_{jm} \right) \left(\delta_{kp} \delta_{lq} + \delta_{kq} \delta_{lp} \right) \\
&= \frac{1}{4} \left(\hat{\Phi}^P_{,ij,kl}(0) + \hat{\Phi}^P_{,ij,lk}(0) + \hat{\Phi}^P_{,ji,kl}(0) + \hat{\Phi}^P_{,ji,lk}(0) \right) \\
&= \hat{\Phi}^P_{,ij,kl}(0).
\end{aligned} \tag{4.37}$$

Here we used that the term $\frac{\partial \hat{\Phi}^P}{\partial \varepsilon_{pq}} \frac{\partial^2 \varepsilon_{pq}}{\partial F_{ij} \partial F_{kl}} \big|_{F=I}$ vanishes because we are in a minimum. All in all we yield

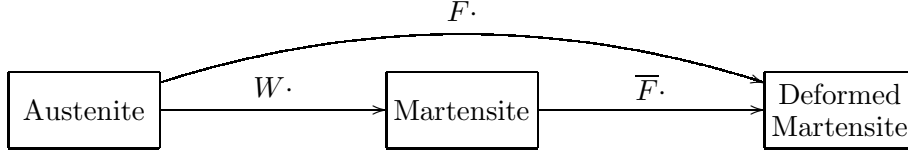$$\mathbb{C}^{\mathrm{A}}_{ijkl} = \Phi^P_{,ij,kl}(I). \tag{4.38}$$

Figure 4.1: Deformations for the computation of the martensitic Young moduli.

Now the same has to be done for the martensitic wells. But here we have to take into account that the martensitic wells are not situated around I, but the other matrices W_1, W_2 and W_3. The guiding principle is that the specimen is first deformed from austenite to martensite by means of W, and then this new configuration is considered as the reference configuration.[9] From there on, the elastic moduli are computed as above by applying a further matrix $\overline{F}$, independently of the transformation by W before. This procedure is depicted in Figure 4.1.

To reduce the case of martensitic wells to the already considered case of the austenitic well, we define the potential energy function $\overline{\Phi}^P$ relative to the martensite by

$$\overline{\Phi}^P(\overline{F}) = \Phi^P(\overline{F}W). \tag{4.39}$$

Thus we have

$$\overline{\Phi}^P(\overline{F}) = \Phi^P(F) \qquad \text{where} \qquad F = \overline{F}W. \tag{4.40}$$

Now the function $\overline{\Phi}^P$ expresses the energy relative to the respective martensitic well, which means that the martensitic well is situated at $\overline{F} = I$. Similar to the procedure above, we pass from $\overline{F}$ to the strain tensor $\overline{\varepsilon}$ via

$$\hat{\overline{\Phi}}^P(\overline{\varepsilon}) = \overline{\Phi}^P(\overline{F}) \qquad \text{where} \qquad \overline{\varepsilon} = \frac{1}{2}\left(\overline{F}^T\overline{F} - I\right) = \frac{1}{2}\left(W^{-1}F^TFW^{-1} - I\right). \tag{4.41}$$

Now $\hat{\overline{\Phi}}^P$ and $\overline{\varepsilon}$ can be used for the Taylor expansion

$$\hat{\overline{\Phi}}^P(\overline{\varepsilon}) \approx c_M + \frac{1}{2}\overline{\varepsilon}_{ij}\overline{\varepsilon}_{kl}\mathbb{C}^{\mathrm{M}}_{ijkl} \tag{4.42}$$

with the martensitic Young modulus

$$\mathbb{C}^{\mathrm{M}}_{ijkl} := \frac{\partial^2}{\partial\overline{\varepsilon}_{ij}\partial\overline{\varepsilon}_{kl}}\hat{\overline{\Phi}}^P\bigg|_{\overline{\varepsilon}=0}. \tag{4.43}$$

Of course the symmetries (4.34) and (4.35) apply here, too.

Finally, the martensitic moduli have to be expressed in terms of Φ^P. Similar to (4.37), we have

$$\hat{\overline{\Phi}}^P_{,ij,kl}(0) = \frac{\partial^2\overline{\Phi}^P}{\partial\overline{F}_{ij}\partial\overline{F}_{kl}}\bigg|_{\overline{F}=I}. \tag{4.44}$$

---

[9]This principle has also been used in [8].

Using $\overline{\Phi}^P(\overline{F}) = \Phi^P(\overline{F}W)$, $F = \overline{F}W$ and $\Phi^P_{,pq}(W) = 0$, we can compute

$$
\begin{aligned}
\overline{\Phi}^P_{,ij,kl}(I) = \left. \frac{\partial^2 \overline{\Phi}^P}{\partial \overline{F}_{ij} \partial \overline{F}_{kl}} \right|_{\overline{F}=I} &= \frac{\partial}{\partial \overline{F}_{ij}} \left[\frac{\partial \Phi^P}{\partial F_{pq}} \frac{\partial F_{pq}}{\partial \overline{F}_{kl}} \right]_{F=W} \\
&= \left[\frac{\partial^2 \Phi^P}{\partial F_{mn} \partial F_{pq}} \frac{\partial F_{mn}}{\partial \overline{F}_{ij}} \frac{\partial F_{pq}}{\partial \overline{F}_{kl}} + \frac{\partial \Phi^P}{\partial F_{pq}} \frac{\partial^2 F_{pq}}{\partial \overline{F}_{ij} \partial \overline{F}_{kl}} \right]_{F=W} \\
&= \Phi^P_{,mn,pq}(W) \delta_{mi} W_{jn} \delta_{pk} W_{lq} \\
&= \Phi^P_{,in,kq}(W) W_{jn} W_{lq}.
\end{aligned}
\tag{4.45}
$$

Thus we conclude

$$
\mathbb{C}^M_{ijkl} = \Phi^P_{,in,kq}(W) W_{jn} W_{lq}.
\tag{4.46}
$$

Already from the last section, we have a program at our disposal to compute the energy $\Phi^P(F)$. Since it determines the second derivatives of the potential as well, we can use it to compute the elastic moduli of the martensite according to (4.46). For the well W_1 we yield[10]

$$
\begin{aligned}
\mathbb{C}^{M1}_{1111} &= 553.119 \text{ GPa}, \\
\mathbb{C}^{M1}_{2222} = \mathbb{C}^{M1}_{3333} &= 491.451 \text{ GPa}, \\
\mathbb{C}^{M1}_{2233} &= 292.370 \text{ GPa}, \\
\mathbb{C}^{M1}_{1122} = \mathbb{C}^{M1}_{1133} &= 412.757 \text{ GPa}, \\
\mathbb{C}^{M1}_{2323} &= 44.720 \text{ GPa}, \\
\mathbb{C}^{M1}_{1212} = \mathbb{C}^{M1}_{1313} &= 104.353 \text{ GPa}.
\end{aligned}
\tag{4.47}
$$

All remaining moduli vanish. For the other wells W_2 and W_3, the axes are interchanged accordingly:

$$
\begin{aligned}
\mathbb{C}^{M2}_{2222} &= 553.119 \text{ GPa}, & \mathbb{C}^{M3}_{3333} &= 553.119 \text{ GPa}, \\
\mathbb{C}^{M2}_{1111} = \mathbb{C}^{M2}_{3333} &= 491.451 \text{ GPa}, & \mathbb{C}^{M3}_{1111} = \mathbb{C}^{M3}_{2222} &= 491.451 \text{ GPa}, \\
\mathbb{C}^{M2}_{1133} &= 292.370 \text{ GPa}, & \mathbb{C}^{M3}_{1122} &= 292.370 \text{ GPa}, \\
\mathbb{C}^{M2}_{1122} = \mathbb{C}^{M2}_{2233} &= 412.757 \text{ GPa}, & \mathbb{C}^{M3}_{1133} = \mathbb{C}^{M3}_{2233} &= 412.757 \text{ GPa}, \\
\mathbb{C}^{M2}_{1313} &= 44.720 \text{ GPa}, & \mathbb{C}^{M3}_{1212} &= 44.720 \text{ GPa}, \\
\mathbb{C}^{M2}_{1212} = \mathbb{C}^{M2}_{2323} &= 104.353 \text{ GPa}, & \mathbb{C}^{M3}_{1313} = \mathbb{C}^{M3}_{2323} &= 104.353 \text{ GPa}.
\end{aligned}
\tag{4.48}
$$

Note that the values given in (4.47) refer to the face-centered tetragonal (fct) lattice which is rotated by 45 degrees within the x_2- and x_3-plane. This orientation is the natural consequence of the lattice transformation from bcc to fct as described in Section 2.3.3. However, in most tables of elastic moduli in literature, the values refer to the base vectors of the lattice. They can be converted as follows. The matrix

$$
R = \begin{pmatrix} 1 & 0 & 0 \\ 0 & \sqrt{\frac{1}{2}} & -\sqrt{\frac{1}{2}} \\ 0 & \sqrt{\frac{1}{2}} & \sqrt{\frac{1}{2}} \end{pmatrix}
\tag{4.49}
$$

---

[10]Note that the elastic moduli of the alloy are higher than the elastic moduli of the pure metals. The latter are given in [49, 56] for the construction of the potential and are reproduced exactly by our procedure here.

describes the rotation which is needed to align the base vectors of the lattice with the coordinate axes. The moduli $\mathbb{C}^{\mathrm{M}}$ from (4.47) refer to the strain tensor $\overline{\varepsilon}$ given by (4.41). We rotate this tensor $\overline{\varepsilon}$ by means of R and yield the new strain tensor

$$\tilde{\varepsilon} = \frac{1}{2}\left(R^{-T}\overline{F}^{T}\overline{F}R^{-1} - I\right) = R^{-T}\overline{\varepsilon}R^{-1}. \tag{4.50}$$

To satisfy the same quadratic approximation, the rotated moduli $\tilde{\mathbb{C}}^{\mathrm{M}}$ must fulfill

$$\overline{\varepsilon}_{ij}\overline{\varepsilon}_{kl}\mathbb{C}^{\mathrm{M}}_{ijkl} = \tilde{\varepsilon}_{i'j'}\tilde{\varepsilon}_{k'l'}\tilde{\mathbb{C}}^{\mathrm{M}}_{i'j'k'l'}. \tag{4.51}$$

Because of $\overline{\varepsilon} = R^{T}\tilde{\varepsilon}R$, this leads to

$$\tilde{\varepsilon}_{i'j'}\tilde{\varepsilon}_{k'l'}\tilde{\mathbb{C}}^{\mathrm{M}}_{i'j'k'l'} = \overline{\varepsilon}_{ij}\overline{\varepsilon}_{kl}\mathbb{C}^{\mathrm{M}}_{ijkl} = R_{i'i}\tilde{\varepsilon}_{i'j'}R_{j'j}R_{k'k}\tilde{\varepsilon}_{k'l'}R_{l'l}\mathbb{C}^{\mathrm{M}}_{ijkl}. \tag{4.52}$$

Hence

$$\tilde{\mathbb{C}}^{\mathrm{M}}_{i'j'k'l'} = R_{i'i}R_{j'j}R_{k'k}R_{l'l}\mathbb{C}^{\mathrm{M}}_{ijkl}. \tag{4.53}$$

We apply this to the values given in (4.47) and yield

$$\begin{aligned}
\tilde{\mathbb{C}}^{\mathrm{M1}}_{1111} &&&= 553.119 \text{ GPa}, \\
\tilde{\mathbb{C}}^{\mathrm{M1}}_{2222} &= \tilde{\mathbb{C}}^{\mathrm{M1}}_{3333} &&= 436.631 \text{ GPa}, \\
\tilde{\mathbb{C}}^{\mathrm{M1}}_{2233} &&&= 347.191 \text{ GPa}, \\
\tilde{\mathbb{C}}^{\mathrm{M1}}_{1122} &= \tilde{\mathbb{C}}^{\mathrm{M1}}_{1133} &&= 412.757 \text{ GPa}, \\
\tilde{\mathbb{C}}^{\mathrm{M1}}_{2323} &&&= 99.541 \text{ GPa}, \\
\tilde{\mathbb{C}}^{\mathrm{M1}}_{1212} &= \tilde{\mathbb{C}}^{\mathrm{M1}}_{1313} &&= 104.353 \text{ GPa}.
\end{aligned} \tag{4.54}$$

Similar values are obtained for the moduli $\tilde{\mathbb{C}}^{\mathrm{M2}}$ and $\tilde{\mathbb{C}}^{\mathrm{M3}}$ of the other two wells from (4.48).

The austenitic Young moduli cannot be measured analogously to the martensitic moduli by means of (4.38) instead of (4.46), since the potential $\Phi^{P}(F)$ describes the energy at zero temperature where the austenitic phase does not occur. Actually, the potential possesses a critical point at the austenitic well $F = I$. But this point is a saddle point, not a minimum. Thus we have to proceed differently. Since there is no way to measure the austenitic moduli at zero temperature, we transform the martensitic moduli appropriately and use them instead.

To this end, the martensitic moduli are transformed from the fct lattice to the bcc lattice. First, they are rotated back as described in (4.53). This leads to $\tilde{\mathbb{C}}$ as given by (4.54). Now we have elastic moduli, which refer to a tetragonally deformed bcc lattice. They do not satisfy the symmetry relations imposed by the symmetry group of the bcc lattice, which require $\mathbb{C}_{1111} = \mathbb{C}_{2222} = \mathbb{C}_{3333}$, $\mathbb{C}_{1122} = \mathbb{C}_{1133} = \mathbb{C}_{2233}$ and $\mathbb{C}_{1212} = \mathbb{C}_{1313} = \mathbb{C}_{2323}$. These additional requirements can be achieved best by taking the geometric mean values:

$$\begin{aligned}
\mathbb{C}^{\mathrm{A}}_{1111} = \mathbb{C}^{\mathrm{A}}_{2222} = \mathbb{C}^{\mathrm{A}}_{3333} &:= \sqrt[3]{\tilde{\mathbb{C}}^{\mathrm{M1}}_{1111}\cdot\tilde{\mathbb{C}}^{\mathrm{M1}}_{2222}\cdot\tilde{\mathbb{C}}^{\mathrm{M1}}_{3333}} = 472.443 \text{ GPa}, \\
\mathbb{C}^{\mathrm{A}}_{1122} = \mathbb{C}^{\mathrm{A}}_{1133} = \mathbb{C}^{\mathrm{A}}_{2233} &:= \sqrt[3]{\tilde{\mathbb{C}}^{\mathrm{M1}}_{1122}\cdot\tilde{\mathbb{C}}^{\mathrm{M1}}_{1133}\cdot\tilde{\mathbb{C}}^{\mathrm{M1}}_{2233}} = 389.630 \text{ GPa}, \\
\mathbb{C}^{\mathrm{A}}_{1212} = \mathbb{C}^{\mathrm{A}}_{1313} = \mathbb{C}^{\mathrm{A}}_{2323} &:= \sqrt[3]{\tilde{\mathbb{C}}^{\mathrm{M1}}_{1212}\cdot\tilde{\mathbb{C}}^{\mathrm{M1}}_{1313}\cdot\tilde{\mathbb{C}}^{\mathrm{M1}}_{2323}} = 102.724 \text{ GPa}.
\end{aligned} \tag{4.55}$$

It remains to determine the constants c_A and c_M, which describe the offset of the potential energy for the austenitic phase and the martensitic phase, respectively. These

offsets are strongly temperature dependent. Since the function Φ^P describes the potential energy only at temperature 0, it cannot be used to determine them. Thus we derive the values from real physical measurements.

The absolute values of the constants are of no interest for the potential. The potential energy is only determined up to an additive constant anyway. But the difference of c_A and c_M has a great influence, since it determines whether the martensitic phase or the austenitic phase is dominant. This difference is basically an affine linear function of the temperature ϑ for a relatively large temperature range. Thus we have

$$c_M - c_A = \mathcal{C}(\vartheta - \vartheta_{\mathrm{eq}}), \tag{4.56}$$

where ϑ_{eq} is the equilibrium temperature at which the phase transformation takes place. For the nickel-aluminum shape memory alloy used here, it is given by $\vartheta_{\mathrm{eq}} = 400K$, see [69]. The constant $\mathcal{C}$ denotes the so-called Clausius-Clapeyron slope. For our alloy, it is given by $\mathcal{C} = 5.4\,\mathrm{MPa/K}$, see [81].

Now, we are given the approximations

$$\Phi^{\mathrm{A}}(F) = c_A + \frac{1}{2}\varepsilon_{ij}\varepsilon_{kl}\mathbb{C}^{\mathrm{A}}_{ijkl} \tag{4.57}$$

$$\Phi^{\mathrm{M}w}(F) = c_M + \frac{1}{2}\overline{\varepsilon}^w_{ij}\overline{\varepsilon}^w_{kl}\mathbb{C}^{\mathrm{M}w}_{ijkl} \tag{4.58}$$

for the austenitic and the martensitic wells $w = 1, 2, 3$ from the construction above. Recall that F, ε and $\overline{\varepsilon}$ are related by (4.26) and (4.41). From this, we construct the overall approximated potential by taking the minimum of these single potentials:

$$\Phi^P(F, \vartheta) = \min\left(\Phi^{\mathrm{A}}(F),\ \Phi^{\mathrm{M1}}(F),\ \Phi^{\mathrm{M2}}(F),\ \Phi^{\mathrm{M3}}(F)\right) - c_A$$
$$= \min\left(\frac{1}{2}\varepsilon_{ij}\varepsilon_{kl}\mathbb{C}^{\mathrm{A}}_{ijkl},\ \mathcal{C}(\vartheta - \vartheta_{\mathrm{eq}}) + \min_{w=1,2,3}\frac{1}{2}\overline{\varepsilon}^w_{ij}\overline{\varepsilon}^w_{kl}\mathbb{C}^{\mathrm{M}w}_{ijkl}\right). \tag{4.59}$$

The temperature dependent offset now determines which wells are active and which are not for a given temperature.

4.4 Application to SMA-based Micro-actuators

The approximated principal part of the potential can now be used for numerical simulations. As an example, we consider the dynamics of micro-actuators made of the shape memory alloy $\mathrm{Ni_{64}Al_{36}}$. Such actuators are an important tool in the field of nano-engineering. These small components are used to generate forces or to cause small movements and thus form the active part within microscale and nanoscale devices. The area of application is very broad and rapidly increasing and includes micro-valves, nano-pliers and other devices. The advantage of SMA-based actuators compared to actuators based on other materials is their precision due to the fixed underlying lattice structures.

We distinguish one-way and two-way micro-actuators. The latter are characterized by their ability to perform a certain movement in forward and in backward direction by themselves. In other words the process is reversible. In contrast to this, one-way actuators can only perform a certain movement in one direction, whereas the return movement has to be induced by outer forces or the like.

In the following, we study both actuator types and an application of each type by numerical simulation. We start with the two-way actuator.
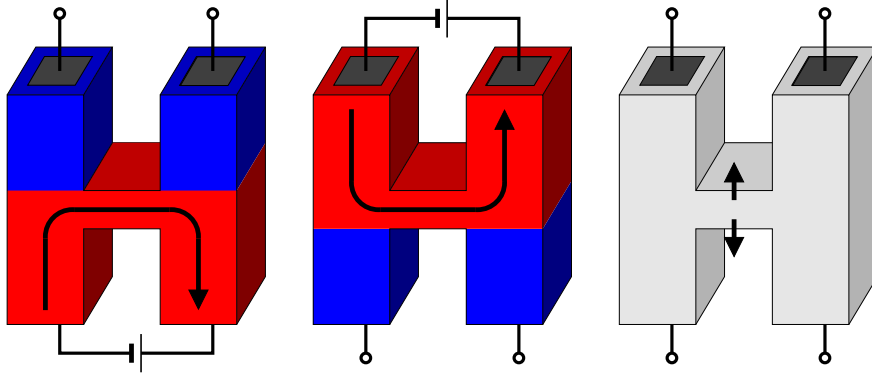
Figure 4.2: Operating principle of the two-way micro-actuator.

4.4.1 Two-way Micro-actuator

The geometry of the two-way micro-actuator that we consider here is shaped like the letter H. The device is fixed at all four end points in such a way that it is slightly stretched in vertical direction. Electrodes are attached to all four end points. The impression of an electrical voltage to two of these electrodes causes a current to flow through a part of the actuator. As a consequence, certain parts of the device will be heated.

The operating principle is depicted in Figure 4.2. First, the electrical voltage is impressed to the lower two electrodes. This induces a current through the lower part of the actuator, including the bridge in the middle. This part is now heated, whereas the remaining part stays cold. This is depicted in red and blue in the left part of Figure 4.2. As a consequence, the specimen transforms to the austenitic phase in the lower part, because this phase is energetically preferable at high temperatures. Opposed to this, the upper part exists in the martensitic phase. Due to the tensile stress in vertical direction, the upper part consists of the martensitic variant with the elongation in vertical direction, see the according well in Table 4.1. Thus the two upper rods of the actuator are slightly longer and thinner than the lower ones.

Then the process is reversed. The electrical current is turned off at the lower part and turned on at the upper part. Therefore, the upper and the middle part will be heated, whereas the lower part cools down, see the second diagram of Figure 4.2. The upper part now transforms to the austenitic phase and the lower part to the martensitic phase. For the same reason as above, the two upper rods of the actuator are shortened and the lower ones lengthened. Since the whole actuator is fixed at the ends, the bridge in the middle of the actuator undergoes a vertical movement. This movement can be used for any desired purpose within the micro-device, such as to control a valve or the like.

The behavior of the actuator will now be simulated numerically. The principal part Φ^P of the potential energy is given by (4.59). The time evolution is then governed by the equation

$$\rho\frac{\partial^2 y}{\partial t^2} = \operatorname{div}\Phi^{P'}(\nabla y) \qquad \text{in } \Omega. \tag{4.60}$$

The H-shaped domain Ω is meshed by means of a simplicial grid. In our application here, 159,744 simplices have been used in total. The evolution equation (4.60) is then discretized in space using piecewise linear and globally continuous finite elements on this

grid. The time discretization is done using finite differences and an implicit scheme. The resulting discrete problem is then reformulated as a non-convex incremental minimization problem in terms of the potential energy. In each time step, it is solved by a steepest descent minimization routine with an Armijo time-step control. Due to the relatively slow transformation process, the mass ρ can be neglected.

The code was developed by the author and has already been used before to simulate the behavior of indium-thallium shape memory alloys. In this application, higher order terms with fractional derivatives and a phenomenological dissipation mechanism have been additionally included, see [7].

For the numerical simulation, the process of redirecting the electrical current is repeated several times. After any redirection, the temperature increases linearly in one part and decreases linearly in the other part. This is reflected in the model by setting the temperature ϑ accordingly, which affects the offset of the different wells in the potential energy (4.59). The middle part is kept continuously hot due to the constant electrical current there.

The results of the numerical simulation are shown in Figure 4.3. First, the current is applied to the lower part. This leads to a transition to the austenitic phase, which is indicated by the green color. The upper part occurs in the martensitic variant which is elongated in vertical direction and displayed in yellow. The remaining two martensitic variants are plotted in red and blue. Then the current is altered. As a consequence, the upper rods transform to the austenite, whereas the lower ones transform to the martensite. This is depicted in the second and third snapshot. One can clearly observe the typical microstructure in the martensitic phase here. The fourth snapshot shows the fully finished transformation process. Note that the middle bar moved upwards during the transformation. Then the current is altered again. The resulting reverse transformation is shown in the fifth and sixth snapshot. Again, it can be clearly recognized that the middle bar has undergone the downward return movement.

4.4.2 One-way Micro-actuator

Let us now consider the second application, namely a pair of pliers whose head parts act as one-way micro-actuators. The underlying geometry consists of a Y-shaped body. At both upper end points, the plier heads are attached, see Figure 4.4. The whole pliers are made of the $Ni_{64}Al_{36}$ shape memory alloy, but only the plier heads work as an active part. The overall size of the pliers can range from $10\mu m$ to 1mm, depending on manufacturing capabilities and the field of application. Larger devices are possible as well, but then classical actuators might be a suitable alternative.

The operating principle of the active plier heads is shown in Figure 4.5. Here only the left head part is depicted. At the beginning, no current is applied such that the head part is cold. It therefore exists in the martensitic phase. The initial configuration is chosen such that the martensitic variant which is elongated horizontally does not occur. Instead only the other two variants exist which are horizontally compressed.

Then a current is impressed to the two electrodes. The head parts heat up and thus transform to the austenitic phase. This way, the deformation is reversed which has been formerly applied to achieve the martensitic deformation. Hence the whole head part elongates in horizontal direction. The elongation ratio is precisely determined by the wells:
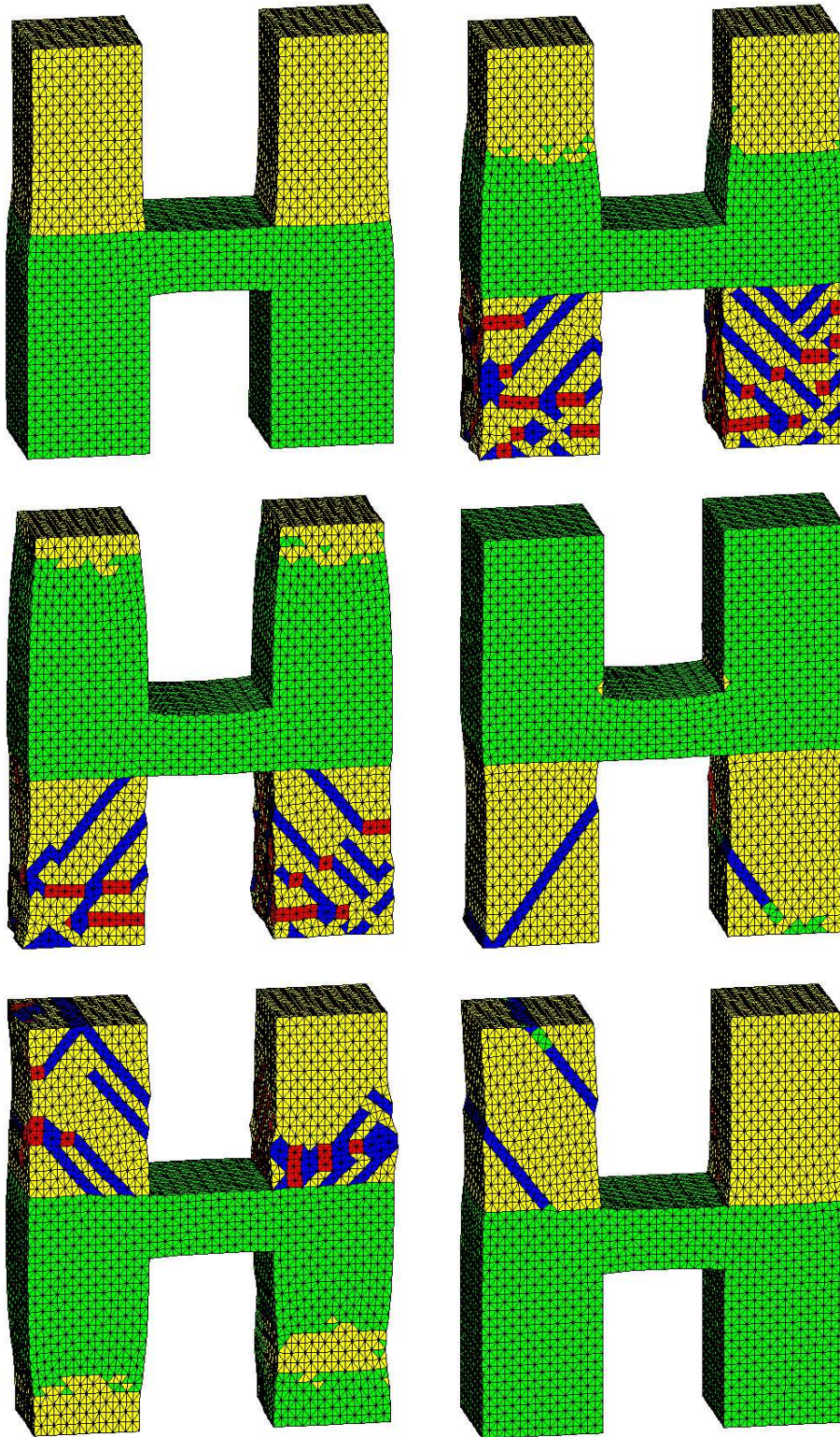
Figure 4.3: Snapshots of the continuum mechanical simulation of the two-way micro-actuator.
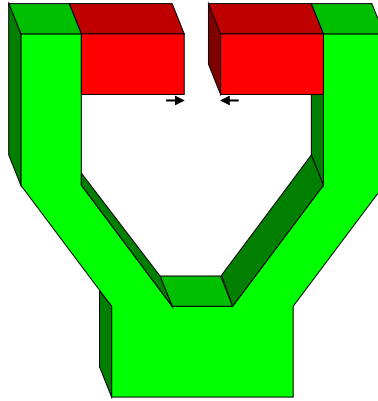
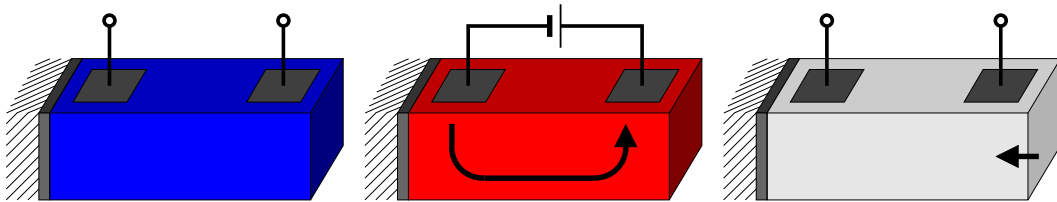*Figure 4.4:* Geometry of the one-way micro-actuator.

Figure 4.5: Operating principle of the one-way micro-actuator.

The initial martensitic compression by the factor 0.89522 is changed to the austenitic state with the factor 1, which results in an elongation ratio of $1/0.89522 \approx 1.11704$. Therefore the plier heads elongate by 11.704%.

Next the current is switched off again. The head parts cool down and transform back to the martensite. But since no force is applied like in the two-way micro-actuator, a mixture of all three martensitic variants occurs. Their macroscopic deformation averages out, such that the shape of the plier heads remains.

This process will now be simulated numerically. Apart from the different geometry, the implementation does not differ from that of the two-way micro-actuator described before.

The initial configuration is chosen in such a way that the plier heads only consist of the martensitic variant which is elongated in rear direction and compressed in horizontal and vertical direction. This variant is depicted in red, see the upper left part of Figure 4.6. Consequently, the distance between the two head parts is large and the pliers are ready to grab a workpiece between the plier heads. The workpiece itself is not simulated here, because this would require a completely different code which can handle contact problems with friction in addition to the elasticity.

Now the plier heads are electrically heated. The resulting transformation to the austenitic phase, depicted in green, is plotted in the next two parts of Figure 4.6. In the fourth snapshot (middle right), the phase transformation is completed. Note that the horizontal compression is now reversed, such that the plier heads have elongated in this direction. As a consequence, the pliers are closed and can now tightly hold a workpiece.

The distance of the plier heads have to be chosen correctly during construction by selecting appropriate dimensions of the plier heads. Here the requirement is that the

distance of the closed pliers must be minimally smaller than the diameter of the workpiece. Then the workpiece will be fixed due to the resulting small elastic force. If however the workpiece is considerably larger than the plier heads distance, then the enormous occurring forces would damage the workpiece or the pliers. Note that these plastic effects are not covered in our purely elastic model.

Finally, the electrical current is switched off again. The subsequent transformation to the martensitic phase during cooling proceeds in such a way that all three martensitic variants occur, see the last two snapshots in Figure 4.6. Consequently the macroscopic shape does not change. This can be clearly observed in figure as the two plier heads remain closed.

If however an outer force or some other loading would be applied now, the plier heads would transform to a specific martensitic variant, which entails a change of the shape.[11] In such a way, the configuration from the beginning can be recovered. Let us remark that this force can as well be induced by a workpiece in-between of the plier heads. Then the workpiece is released.

4.5   Approximation of the Higher Order Terms

After having extensively discussed the approximation of the principal part of the potential energy and its application for the numerical simulation of SMA micro-actuators, we now come to the remaining part of higher order contributions. As given by the decoupling (4.13), this part reads as

$$\Phi^H(d_1, d_2, \ldots, d_K) = \frac{1}{2} \sum_{k=2}^{K} \sum_{l=2}^{K} \Phi_{,d_k,d_l}^{(\mathrm{I}),\overline{x}}(d_1, 0, \ldots, 0) : d_k : d_l. \qquad (4.61)$$

According to Section 4.3.1, the minima of the potential energy are related to each other by frame indifference and by lattice symmetry. Hence, the potential behaves identically in the vicinity of each minimum, which is a consequence of Lemma 4.3. The locations of the minima are determined for the most part by the argument d_1, such that it makes sense to replace d_1 by any value which also describes a minimum. Here we choose W_1. In the vicinity of the minima where the approximation takes place, the higher order part (4.61) is then well approximated by

$$\Phi^H(d_1, d_2, \ldots, d_K) \approx \frac{1}{2} \sum_{k=2}^{K} \sum_{l=2}^{K} C_{kl} : d_k : d_l \qquad (4.62)$$

where

$$C_{kl} := \Phi_{,d_k,d_l}^{(\mathrm{I}),\overline{x}}(W_1, 0, \ldots, 0). \qquad (4.63)$$

As the argument d_k lives in the space $\mathbb{R}^{d^{k+1}}$, we have $C_{kl} \in \mathbb{R}^{d^{k+1} \cdot d^{l+1}} = \mathbb{R}^{d^{k+l+2}}$. This huge number of coefficients can be reduced as follows. In Lemma 4.3 we have shown that the atomic frame indifference and the atomic lattice symmetry are not only carried over to the principal part of the continuum potential, but also to the higher order contributions.

---

[11]Then this works similarly to the two-way micro-actuator, whose working principle relies on the tension of the whole actuator.
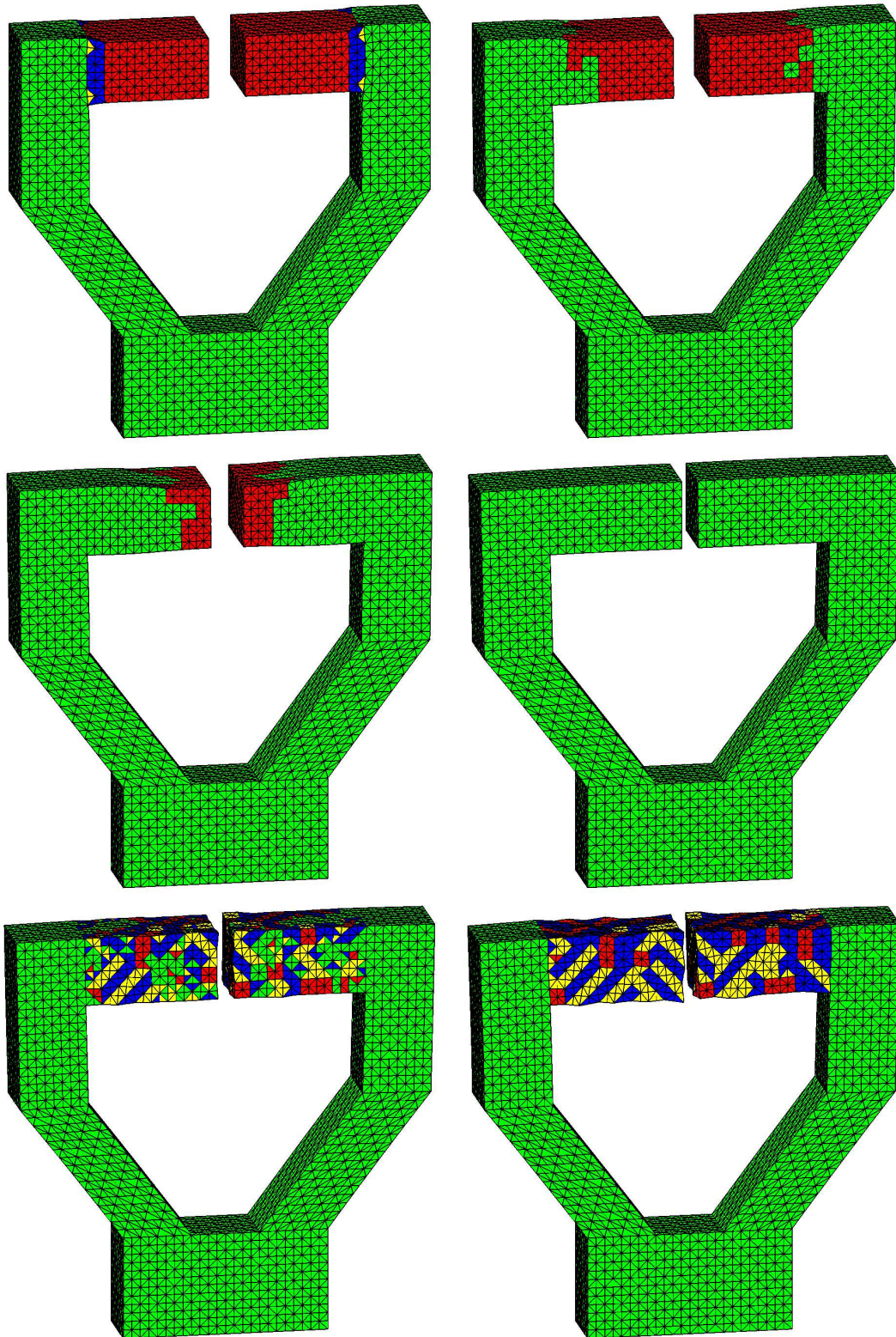
Figure 4.6: Snapshots of the continuum mechanical simulation of the one-way micro-actuator.

Similarly to Lemma 4.5, the potential therefore does not depend on $d_2, d_3, \ldots, d_K$ in an arbitrary manner, but can be written in terms of generalized Cauchy-Green strain tensors

$$\varepsilon_{m_1 \ldots m_k n_1 \ldots n_l}^{kl} := \frac{1}{2} \sum_{i=1}^{d} (d_k)_{m_1 \ldots m_k}^i (d_l)_{n_1 \ldots n_l}^i. \tag{4.64}$$

These tensors inhibit many symmetries, which then constrain the number of different entries in the tensors C_{kl} similar to (4.35). However, these calculations are long and tedious and will not be carried out here.

Furthermore, not all constants C_{kl} are equally relevant for the behavior of the model. Hence it makes sense to neglect some of these terms. Here the non-diagonal entries C_{kl} with $k \neq l$ are of lower importance than the diagonal entries C_{kk}, hence we further diagonalize the system by means of

$$\Phi^H(d_1, d_2, \ldots, d_K) \approx \frac{1}{2} \sum_{k=2}^{K} C_{kk} : d_k : d_k. \tag{4.65}$$

Let us note that terms like in (4.65) are often added phenomenologically to common continuum mechanical models and are then called capillarity terms, see [63] for an overview of such models. Sometimes similar effects can be achieved by other types of higher order contribution as well, see for example [7], where higher order contributions in terms of non-local fractional order derivatives have been employed. But contrary to this, the expression (4.65) is deduced from first principles here.

This general approximation technique will now be applied to the EAM potential. The EAM potential $\Phi^{(A)}$ as defined by (2.48), (2.49) and (2.47) is localized by splitting it up into every pair interaction Φ_{ab}^{pair} and every embedding term $\Phi_a^{\text{emb}}(\rho_a^{\text{host}})$. Here a and b stand for either nickel or aluminum. According to Section 3.1.3, the expansion points are chosen as $\overline{x} = \frac{1}{2}(x + \tilde{x})$ for the pair interaction of $y(x)$ and $y(\tilde{x})$ and as the center point $\overline{x} = x$ for the embedding term of the atom $y(x)$.

To shorten notation, we introduce the difference vector $z = \tilde{x} - x$. Then the Taylor series expansion for the inner expansion technique of $y(\tilde{x}) - y(x)$ up to order $K = 3$ reads as

$$T_z^{\text{p}} = \nabla y(\overline{x}) \cdot z + \frac{1}{24} \nabla^3 y(\overline{x}) : z^3 \tag{4.66}$$

for the pair interactions and

$$T_z^{\text{e}} = \nabla y(\overline{x}) \cdot z + \frac{1}{2} \nabla^2 y(\overline{x}) : z^2 + \frac{1}{6} \nabla^3 y(\overline{x}) : z^3 \tag{4.67}$$

for the embedding part. We have chosen the approximation order $K = 3$, because for $K = 2$ we would obtain higher order terms only from the embedding part, but not from the pair interaction, whereas for $K = 3$ both interaction types contribute. This choice also turned out to be the most useful one for the Stillinger-Weber potential in Section 3.5.1.

We are now ready to give an explicit expression of $\Phi^{(I),\overline{x}}$ which is needed in (4.63). To this end, we define the sublattices

$$\mathcal{L}_1 = a_0 \mathbb{Z}^3 \setminus \{0\}, \qquad \mathcal{L}_2 = a_0 \mathbb{Z}^3 + \frac{a_0}{2} \begin{pmatrix} 1 \\ 1 \\ 1 \end{pmatrix}. \tag{4.68}$$

The potential energy is then assembled according to the mixing rules of 64% nickel and 36% aluminum atoms as described in Section 4.3.1. This leads to

$$
\Phi^{(I),\overline{x}}\big(\nabla y(\overline{x}), \nabla^2 y(\overline{x}), \nabla^3 y(\overline{x})\big) = \frac{1}{a_0{}^3}\Bigg\{
$$

$$
\frac{1}{2}\Bigg[\sum_{z\in\mathcal{L}_1} \Phi^{\mathrm{pair}}_{\mathrm{NiNi}}(|T_z^{\mathrm{p}}|) + \sum_{z\in\mathcal{L}_2} (2\mu-1)\Phi^{\mathrm{pair}}_{\mathrm{NiNi}}(|T_z^{\mathrm{p}}|) + (2-2\mu)\Phi^{\mathrm{pair}}_{\mathrm{NiAl}}(|T_z^{\mathrm{p}}|) \Bigg]
$$

$$
+\frac{2\mu-1}{2}\Bigg[\sum_{z\in\mathcal{L}_1} (2\mu-1)\Phi^{\mathrm{pair}}_{\mathrm{NiNi}}(|T_z^{\mathrm{p}}|) + (2-2\mu)\Phi^{\mathrm{pair}}_{\mathrm{NiAl}}(|T_z^{\mathrm{p}}|) + \sum_{z\in\mathcal{L}_2} \Phi^{\mathrm{pair}}_{\mathrm{NiNi}}(|T_z^{\mathrm{p}}|) \Bigg]
$$

$$
+\frac{2-2\mu}{2}\Bigg[\sum_{z\in\mathcal{L}_1} (2\mu-1)\Phi^{\mathrm{pair}}_{\mathrm{NiAl}}(|T_z^{\mathrm{p}}|) + (2-2\mu)\Phi^{\mathrm{pair}}_{\mathrm{AlAl}}(|T_z^{\mathrm{p}}|) + \sum_{z\in\mathcal{L}_2} \Phi^{\mathrm{pair}}_{\mathrm{NiAl}}(|T_z^{\mathrm{p}}|) \Bigg]
$$

$$
+\Phi^{\mathrm{emb}}_{\mathrm{Ni}}\Bigg(\sum_{z\in\mathcal{L}_1} \rho^{\mathrm{atom}}_{\mathrm{Ni}}(|T_z^{\mathrm{e}}|) + \sum_{z\in\mathcal{L}_2} (2\mu-1)\rho^{\mathrm{atom}}_{\mathrm{Ni}}(|T_z^{\mathrm{e}}|) + (2-2\mu)\rho^{\mathrm{atom}}_{\mathrm{Al}}(|T_z^{\mathrm{e}}|) \Bigg)
$$

$$
+(2\mu-1)\Phi^{\mathrm{emb}}_{\mathrm{Ni}}\Bigg(\sum_{z\in\mathcal{L}_1} (2\mu-1)\rho^{\mathrm{atom}}_{\mathrm{Ni}}(|T_z^{\mathrm{e}}|) + (2-2\mu)\rho^{\mathrm{atom}}_{\mathrm{Al}}(|T_z^{\mathrm{e}}|) + \sum_{z\in\mathcal{L}_2} \rho^{\mathrm{atom}}_{\mathrm{Ni}}(|T_z^{\mathrm{e}}|) \Bigg)
$$

$$
+(2-2\mu)\Phi^{\mathrm{emb}}_{\mathrm{Al}}\Bigg(\sum_{z\in\mathcal{L}_1} (2\mu-1)\rho^{\mathrm{atom}}_{\mathrm{Ni}}(|T_z^{\mathrm{e}}|) + (2-2\mu)\rho^{\mathrm{atom}}_{\mathrm{Al}}(|T_z^{\mathrm{e}}|) + \sum_{z\in\mathcal{L}_2} \rho^{\mathrm{atom}}_{\mathrm{Ni}}(|T_z^{\mathrm{e}}|) \Bigg)\Bigg\}
$$

$$
\tag{4.69}
$$

where $\mu = 0.64$. This expression is now substituted into (4.65) which finally leads to the higher order part

$$
\Phi^H\big(\nabla y(\overline{x}), \nabla^2 y(\overline{x}), \nabla^3 y(\overline{x})\big)
$$

$$
= \frac{1}{2}C_{22} : \nabla^2 y(\overline{x}) : \nabla^2 y(\overline{x}) + \frac{1}{2}C_{33} : \nabla^3 y(\overline{x}) : \nabla^3 y(\overline{x})
$$

$$
= \frac{1}{2}\sum_{i,j,k=1}^{3}\sum_{m,n,p=1}^{3} \Phi^{(I),\overline{x}}_{,y^i_{,j,k},y^m_{,n,p}}(W_1,0,0)\, y^i_{,j,k}(\overline{x})\, y^m_{,n,p}(\overline{x})
$$

$$
+ \frac{1}{2}\sum_{i,j,k,l=1}^{3}\sum_{m,n,p,q=1}^{3} \Phi^{(I),\overline{x}}_{,y^i_{,j,k,l},y^m_{,n,p,q}}(W_1,0,0)\, y^i_{,j,k,l}(\overline{x})\, y^m_{,n,p,q}(\overline{x}). \tag{4.70}
$$

Together with the principal part Φ^P given by (4.59), we obtain the approximated potential energy density with higher order contributions

$$
\Phi^{(I),\overline{x}}\big(\nabla y(\overline{x}), \nabla^2 y(\overline{x}), \nabla^3 y(\overline{x}), \vartheta\big) = \Phi^P\big(\nabla y(\overline{x}), \vartheta\big) + \Phi^H\big(\nabla y(\overline{x}), \nabla^2 y(\overline{x}), \nabla^3 y(\overline{x})\big) \tag{4.71}
$$

on the continuum mechanical level. The corresponding evolution equations read as

$$
a_0{}^3\rho\frac{\partial^2 y^i}{\partial t^2} = \sum_{j=1}^{3}\frac{\partial}{\partial x_j}\Phi^P_{,y^i_{,j}}(\nabla y, \vartheta) - \sum_{j,k,m,n,p=1}^{3}\Phi^{(I),\overline{x}}_{,y^i_{,j,k},y^m_{,n,p}}(W_1,0,0)\, y^m_{,j,k,n,p}(\overline{x})
$$

$$
+ \sum_{j,k,l,m,n,p,q=1}^{3}\Phi^{(I),\overline{x}}_{,y^i_{,j,k,l},y^m_{,n,p,q}}(W_1,0,0)\, y^m_{,j,k,l,n,p,q}(\overline{x}) \tag{4.72}
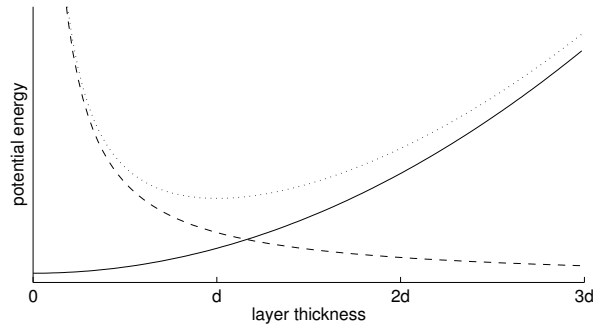$$

Figure 4.7: Scheme of competing principal part energy (solid line) and curvature energy (dashed line) in the higher order model. The sum (dotted line) attains its minimum at the fixed layer thickness $d > 0$ and therefore determines the length scale.

for $i = 1, 2, 3$. This continuum mechanical model now includes the microscopic effects of the EAM potential. It improves the model developed in Section 4.3 which consists of the principal part only.

In the numerical simulation of the micro-actuators in Section 4.4 we have seen that quite often a mixture of different martensitic variants occurs in addition to regions of a pure martensitic or austenitic variant. The mixture appears in form of stacked layers (see for example the upper right snapshot of Figure 4.3), since this arrangement is energetically most favorable [9, 10, 24]. This is a typical pattern found in shape memory alloys and is called a laminated microstructure.

The principal part of the model describes the occurrence and the geometric orientation of the microstructure very well. However, it does not specify the thickness of the layers, because the deformation gradient ∇y which the continuum model for $K = 1$ solely depends on is a dimensionless quantity and therefore cannot determine the length scale. Compatibility restrictions at the boundary enforce that the thickness of the layers tends to be infinitesimally small in the continuum model for energetically minimal configurations. Within the discretized model, the thickness is bounded from below by the mesh size only. Therefore, the layer thickness in the numerical simulations of the micro-actuators measures one tetrahedron, as can be clearly observed in Figures 4.3 and 4.6.

The improved model developed here now compensates for this non-intended but inevitable effect. The higher order terms energetically penalize the curvature at the interface between two layers and thus restrict the number of layer alterations. As a consequence, the layer thickness is bounded from below. The potential energies given by the principal part and by the higher order contributions now compete with each other, as the first prefers a large number of thin layers, whereas the latter favors few but thick layers. Together, they are energetically optimal for a fixed layer thickness $d > 0$. The competition is schematically depicted in Figure 4.7.

As a consequence, the higher order contributions regularize the model and fix its length scale. The layer thickness is now constricted to the thickness given from the atomic level. This thickness will then be resolved by the discretized model as well if the mesh is chosen fine enough. But contrary to the model used in Section 4.4, a further mesh refinement will no longer result in finer layers; instead the thickness remains fixed and thus gives a physically correct description of the microstructure.

Chapter 5

Numerical Techniques for the Evolution Equations

In the preceding chapters, we analyzed the behavior of the solutions of the evolution equations which have been derived by the inner expansion technique. The main interest there was to compare and rate the outcome of the upscaling scheme, but not how the solutions have been obtained. We now make up for the numerical techniques in this chapter. To this end, we develop and analyze methods to numerically solve the evolution equations.

The inner expansion technique leads to the system of partial differential equations (PDE)

$$\rho\frac{\partial^2 y}{\partial t^2} = \sum_{k=1}^{K}(-1)^{k+1}\operatorname{div}^k \Phi_{,k}^{(\mathrm{J}),x}(y,\nabla y,\nabla^2 y,\dots,\nabla^K y) \qquad \text{in } \Omega \times (0,T) \qquad (5.1)$$

for the evolution of the specimen within the time interval $(0,T)$, compare (3.18). Recall that the deformation function y maps the reference configuration $\Omega \subset \mathbb{R}^d$ to $\mathbb{R}^d$. Let us note that the scaling technique and the direct expansion technique lead to evolution equations which can be written in this form as well, hence the methods developed here apply for them, too.

The evolution equation is equipped with the initial values

$$y(x,0) = y_0(x) \quad \text{and} \quad \frac{\partial y}{\partial t}(x,0) = y_1(x) \qquad \forall x \in \Omega, \qquad (5.2)$$

compare (3.19), and the boundary conditions

$$\nabla_\nu^k y(x,t) = \nabla_\nu^k z(x) \qquad \forall x \in \partial\Omega,\ t > 0,\ k = 0,1,\dots,K-1 \qquad (5.3)$$

for some fixed function z, compare (3.20).

We are primarily, but not exclusively, interested in a quadratic potential energy function. In this case, the according PDE is linear. Thus (5.1) can be shortly written as

$$\rho\frac{\partial^2 y}{\partial t^2} = Ly \qquad \text{in } \Omega \times (0,T), \qquad (5.4)$$

where L denotes the linear differential operator in space from (5.1). Without loss of generality we assume $\rho = 1$.

For the numerical solution, a method with a high consistency order is necessary to resolve the spatial derivatives. A method which is only consistent up to order one or two would introduce higher order error terms which interfere with the higher order derivatives of the continuum model. The latter resemble the discreteness of the atomistic system and are decisive for the accurate description of the microscale. Since we are interested in the precise discreteness effects of the PDE and not in the consistency error of the discretization, methods of low order cannot be used here.

In the following, we develop a method of high order, which ensures that the spatial discretization errors of low order are eliminated and dispersion comes basically from the higher order terms of the PDE itself and not from the finite difference discretization. Furthermore, a mantissa size of 512 bits has been used for the numerical calculations to guarantee that roundoff errors do not destroy the high order of the respective scheme.

5.1   Time and Space Discretization

To solve (5.4) numerically, we need to discretize it first. For this purpose, we employ the finite difference method, both for time and space discretization. Over the finite element method it has the advantage that integration schemes are avoided which can get rather complex for higher orders of approximation.

First, we subdivide the time interval $[0, T]$ into $N + 1$ points

$$0, \ \delta t, \ 2\delta t, \ \ldots, \ (N-1)\delta t, \ N\delta t = T, \tag{5.5}$$

where $\delta t > 0$ denotes the time step size. Similarly, we place the grid $\delta x \, \mathbb{Z}^d$ over the spatial domain Ω. We will now try to approximate the function values of the exact solution function y at each such point in time and space. To this end, we introduce the set of variables $Y_m^n \in \mathbb{R}^d$ for all $n = 1, 2, \ldots, N$ and for all $m \in \mathbb{Z}^d$ such that $m \, \delta x \in \Omega$. Thus the variable Y_m^n should approximate the function value

$$y_m^n := y(m \, \delta x, n \, \delta t). \tag{5.6}$$

To incorporate the initial values, we also define the values

$$Y_m^0 = y_0(m \, \delta x) \qquad \text{and} \qquad Y_m^{-1} = Y_m^0 - \delta t \, y_1(m \, \delta x). \tag{5.7}$$

To shorten notation, we denote the vector of all variables Y_m^n and y_m^n by Y^n and y^n, respectively.

Second, the spatial derivatives in the PDE are approximated by finite difference stencils. The concrete construction of the difference stencils will be carried out in Section 5.3. Here it is sufficient to know that the continuous operator L is replaced by a linear difference operator $L_{\delta x}$ which acts on the vector Y^n. The difference stencils have to make use of the given boundary values, which are not included in the set of variables. These boundary values are transferred to the right-hand side in a standard manner. This introduces an additional constant $C_{\delta x}$ when applying the stencils. Thus $Ly(\cdot, n \, \delta t)$ is approximated by $L_{\delta x} Y^n + C_{\delta x}$.

The second time derivative in the PDE is handled similarly to the spatial derivatives. Here we choose the symmetric three-point difference stencil, which leads to the leap frog scheme

$$\frac{Y^{n+1} - 2Y^n + Y^{n-1}}{\delta t^2} = L_{\delta x} Y^n + C_{\delta x} \tag{5.8}$$

for $n = 0, 1, 2, \ldots, N - 1$. This is an explicit Euler scheme and can be solved by the time marching algorithm

$$\begin{aligned} &\texttt{for } n = 0, 1, 2, \ldots, N - 1 \texttt{ do} \\ &\quad Y^{n+1} \leftarrow 2Y^n - Y^{n-1} + \delta t^2 (L_{\delta x} Y^n + C_{\delta x}). \end{aligned} \tag{5.9}$$

5.2 Convergence Estimates

Now we have to show that Y converges to y in a suitable sense. As we will see in the proofs later, it is appropriate to measure the convergence pointwise in time and in the discrete L^2-norm in space. Hence we have to show that this norm of the error vector

$$e^n = y^n - Y^n \tag{5.10}$$

converges to zero for all time steps $n = 1, 2, 3, \ldots, N$. The discrete L_2-norm of e^n is defined by

$$\|e^n\| := \sqrt{\delta x^{-d} \sum_{m \in \mathbb{Z}^d : \, m\,\delta x \in \Omega} |e_m^n|^2} \tag{5.11}$$

and resembles a discrete version of the continuous L_2-norm.[1] Within this chapter, we denote both this norm and the corresponding operator norm for linear mappings by $\|\cdot\|$.

Beyond the mere convergence, the order of convergence is of interest.

Definition 5.1 *(Convergence) The difference method is said to be convergent with order $\alpha \in \mathbb{R}^+$ in time and order $\beta \in \mathbb{R}^+$ in space if there is a constant $C_1 \in \mathbb{R}$ which is independent of δt and δx, such that the error e^n fulfills*

$$\|e^n\| \leq C_1 (\delta t^\alpha + \delta x^\beta) \tag{5.12}$$

for all $n = 1, 2, \ldots, N$.

Note that the constant C_1 may depend on y.

The convergence will be shown by proving consistency of the difference stencil and stability of the scheme. First, we come to the consistency. Thereto we introduce the truncation error, which measures the deviation of the discrete differential operator from the continuous operator. It is obtained by applying the discrete difference stencil minus the continuous differential operator $\partial_t^2 - L$ to the continuous solution y. Since $(\partial_t^2 - L)y = 0$ due to (5.4), the definition of the truncation error reads as

$$\tau^n = \frac{y^{n+1} - 2y^n + y^{n-1}}{\delta t^2} - L_{\delta x} y^n - C_{\delta x}. \tag{5.13}$$

---

[1] The discrete L_2-norm is the Euclidean norm with the additional factor δx^{-d} to compensate for the varying number of entries in the vector. All subsequent proofs work without this factor as well, but the assumption of consistency (see Definition 5.2) is in general not fulfilled in this case. The discrete L_2-norm equals the root-mean-square (RMS) up to a factor which is independent of δx.

Definition 5.2 *(Consistency) The difference approximation is said to be consistent with order $\alpha \in \mathbb{R}^+$ in time and order $\beta \in \mathbb{R}^+$ in space if there is a constant $C_2 \in \mathbb{R}$ which is independent of δt and δx, such that the truncation error τ^n fulfills*

$$\|\tau^n\| \leq C_2(\delta t^\alpha + \delta x^\beta) \tag{5.14}$$

for all time steps $n = 0, 1, 2, \ldots, N$.

Just as the constant C_1 above, C_2 may depend on y as well. The concrete proof of consistency depends on the actual choice of the difference stencils and will therefore be done in Section 5.3 where the concrete stencils will be constructed.

We now come to stability.

Definition 5.3 *(Stability) The difference method is said to be stable if $L_{\delta x}$ is diagonalizable, if $L_{\delta x}$ has only real eigenvalues, and if for all $\delta x > 0$ the time step size δt is chosen so small that every eigenvalue λ of $L_{\delta x}$ satisfies the estimate*

$$-\frac{C_4}{\delta t^2} \leq \lambda \leq -C_3 \tag{5.15}$$

for some constants $C_3 > 0$ and $C_4 < 4$ which are independent of δx and δt.

This definition of stability looks unconventional. But we will see in the next lemma that this condition just implies stability in the common sense, namely that two solutions of the discrete scheme, whose initial values differ only slightly, differ only slightly within the whole time interval as well, see e.g. [76, Section 2.4].[2] The left inequality of (5.15) imposes a restriction on the time step size and is called the *CFL condition*. It has been introduced for the wave equation already in 1928 by Courant, Friedrichs and Lewy [23].

Lemma 5.1 *(Stability estimate) Let the difference method be stable in the sense of Definition 5.3, and let Y and $\tilde{Y}$ denote two solutions of the discrete scheme with different initial values. Then the difference $Z = Y - \tilde{Y}$ fulfills*

$$\|Z^n\| \leq \frac{2}{\delta t \sqrt{C_3(4 - C_4)}} \|P\| \|P^{-1}\| \big(\|Z^0\| + \|Z^{-1}\|\big) \tag{5.16}$$

for all $n = 1, 2, 3, \ldots, N$, where $P \in GL$ is a matrix such that $P^{-1} L_{\delta x} P$ is diagonal.

PROOF The iterates Y and $\tilde{Y}$ are constructed by the recurrence relations

$$
\begin{aligned}
Y^{n+1} &= 2Y^n - Y^{n-1} + \delta t^2 \big(L_{\delta x} Y^n + C_{\delta x}\big) \\
\tilde{Y}^{n+1} &= 2\tilde{Y}^n - \tilde{Y}^{n-1} + \delta t^2 \big(L_{\delta x} \tilde{Y}^n + C_{\delta x}\big)
\end{aligned}
\tag{5.17}
$$

for all $n = 0, 1, 2, \ldots, N-1$. Hence the difference $Z = Y - \tilde{Y}$ fulfills the recurrence relation

$$Z^{n+1} = 2Z^n - Z^{n-1} + \delta t^2 L_{\delta x} Z^n. \tag{5.18}$$

---

[2]Warning: In case of simple schemes for PDEs which are first order in time, this is in general already fulfilled if the eigenvalues λ of $L_{\delta x}$ are bounded from above. However, for the second order equations studied here, we have a more complex behavior, as can be seen from the following estimates.

To give an expression of Z^n in closed form, it is convenient to rewrite first the two-step recurrence relation as the one-step recurrence relation

$$\begin{pmatrix} Z^{n+1} \\ Z^n \end{pmatrix} = \underbrace{\begin{pmatrix} 2I + \delta t^2 L_{\delta_x} & -I \\ I & 0 \end{pmatrix}}_{=:A} \begin{pmatrix} Z^n \\ Z^{n-1} \end{pmatrix} \tag{5.19}$$

in vectorial form. Here the matrix A is a block matrix. Then we have

$$\begin{pmatrix} Z^n \\ Z^{n-1} \end{pmatrix} = A^n \begin{pmatrix} Z^0 \\ Z^{-1} \end{pmatrix}. \tag{5.20}$$

To further estimate this expression, we diagonalize the matrix A. To this end we employ the block structure of the matrix A. By assumption $\tilde{L}_{\delta_x} := P^{-1} L_{\delta_x} P$ is diagonal. Hence each block of

$$\tilde{A} := \begin{pmatrix} P & 0 \\ 0 & P \end{pmatrix}^{-1} \begin{pmatrix} 2I + \delta t^2 L_{\delta_x} & -I \\ I & 0 \end{pmatrix} \begin{pmatrix} P & 0 \\ 0 & P \end{pmatrix} = \begin{pmatrix} 2I + \delta t^2 \tilde{L}_{\delta_x} & -I \\ I & 0 \end{pmatrix} \tag{5.21}$$

is diagonal. Furthermore, let the diagonal matrices $\Lambda_{1,2}$ denote the roots of the blockwise characteristic polynomial of $\tilde{A}$:

$$\Lambda^2 - (2I + \delta t^2 \tilde{L}_{\delta x})\Lambda + I, \tag{5.22}$$

i.e. define

$$\Lambda_{1,2} = \frac{2I + \delta t^2 \tilde{L}_{\delta x}}{2} \pm \frac{i}{2}\sqrt{-4\delta t^2 \tilde{L}_{\delta x} - (\delta t^2 \tilde{L}_{\delta x})^2}. \tag{5.23}$$

The discriminant is diagonal and positive due to (5.15), such that the root is uniquely defined. The diagonal matrices Λ_1 and Λ_2 contain the eigenvalues of the matrix $\tilde{A}$, which coincide with those of A. Λ_1 and Λ_2 can be interpreted as block eigenvalues of the block matrix $\tilde{A}$.

The diagonal matrix $\Lambda_1 - \Lambda_2$ is regular, because the stability assumption (5.15) implies for the j-th diagonal entry

$$\begin{aligned} |(\Lambda_1 - \Lambda_2)_{jj}|^2 &= \left| 4\delta t^2 (\tilde{L}_{\delta x})_{jj} + (\delta t^2 (\tilde{L}_{\delta x})_{jj})^2 \right| \\ &= \left| \delta t^2 (\tilde{L}_{\delta x})_{jj} \right| \cdot \left| 4 + \delta t^2 (\tilde{L}_{\delta x})_{jj} \right| \\ &\geq \delta t^2 C_3 (4 - C_4) > 0. \end{aligned} \tag{5.24}$$

Define

$$Q = \begin{pmatrix} I & I \\ \Lambda_2 & \Lambda_1 \end{pmatrix}, \tag{5.25}$$

then we have

$$Q^{-1} = \begin{pmatrix} \Lambda_1 - \Lambda_2 & 0 \\ 0 & \Lambda_1 - \Lambda_2 \end{pmatrix}^{-1} \begin{pmatrix} \Lambda_1 & -I \\ -\Lambda_2 & I \end{pmatrix}. \tag{5.26}$$

With the help of (5.22) it is easy to verify that $\hat{A} := Q^{-1} \tilde{A} Q$ has the form

$$\hat{A} = Q^{-1} \tilde{A} Q = \begin{pmatrix} \Lambda_1 & 0 \\ 0 & \Lambda_2 \end{pmatrix}. \tag{5.27}$$

Thus we now have diagonalized the matrix $\tilde{A}$. The block columns of Q are the block eigenvectors of $\tilde{A}$. All in all the matrix A is diagonalized by

$$A = \begin{pmatrix} P & 0 \\ 0 & P \end{pmatrix} Q \hat{A} Q^{-1} \begin{pmatrix} P & 0 \\ 0 & P \end{pmatrix}^{-1}. \tag{5.28}$$

We insert this into the closed form (5.20) and yield

$$\begin{pmatrix} Z^n \\ Z^{n-1} \end{pmatrix} = \begin{pmatrix} P & 0 \\ 0 & P \end{pmatrix} Q \hat{A}^n Q^{-1} \begin{pmatrix} P & 0 \\ 0 & P \end{pmatrix}^{-1} \begin{pmatrix} Z^0 \\ Z^{-1} \end{pmatrix}. \tag{5.29}$$

Multiplication of the above terms leads to

$$Z^n = P(\Lambda_1 - \Lambda_2)^{-1} \left[(\Lambda_1^{n+1} - \Lambda_2^{n+1}) P^{-1} Z^0 - (\Lambda_1^n - \Lambda_2^n) P^{-1} Z^{-1} \right]. \tag{5.30}$$

This expression will now be estimated. It is easy to verify that each diagonal entry of $\Lambda_{1,2}$ as given by (5.23) has absolute value 1. Therefore we conclude

$$\|\Lambda_1^n\| = \|\Lambda_1^{n+1}\| = \|\Lambda_2^n\| = \|\Lambda_2^{n+1}\| = 1. \tag{5.31}$$

Furthermore, by (5.24) we have

$$\left\|(\Lambda_1 - \Lambda_2)^{-1}\right\| = \max_j \frac{1}{|(\Lambda_1 - \Lambda_2)_{jj}|} \leq \frac{1}{\delta t \sqrt{C_3(4 - C_4)}}. \tag{5.32}$$

We now use the submultiplicativity and the triangle inequality of the norms and apply the estimates (5.31) and (5.32) to obtain the desired stability estimate (5.16) from (5.30):

$$\begin{aligned} \|Z^n\| &\leq \|P\| \|(\Lambda_1 - \Lambda_2)^{-1}\| \left[\left(\|\Lambda_1^{n+1}\| + \|\Lambda_2^{n+1}\|\right) \|P^{-1}\| \|Z^0\| \right. \\ &\qquad\qquad\qquad \left. + \left(\|\Lambda_1^n\| + \|\Lambda_2^n\|\right) \|P^{-1}\| \|Z^{-1}\| \right] \\ &\leq \frac{2}{\delta t \sqrt{C_3(4 - C_4)}} \|P\| \|P^{-1}\| \left(\|Z^0\| + \|Z^{-1}\|\right). \end{aligned} \tag{5.33}$$

Thus the lemma is proved. $\square$

Now we are ready to state and prove the main convergence theorem. In the context of first order conservation laws, this is known as the Lax Theorem, see e.g. [54] and [76].

Lemma 5.2 *(First convergence estimate) Assume that the scheme is consistent with order α in time and order β in space and that it is stable. Then the error e^n fulfills*

$$\|e^n\| \leq \frac{2C_2 T}{\sqrt{C_3(4 - C_4)}} \|P\| \|P^{-1}\| (\delta t^\alpha + \delta x^\beta), \tag{5.34}$$

where C_3 and C_4 are the constants from Definition 5.3 and where P is a regular matrix such that $P^{-1} L_{\delta_x} P$ is diagonal.

PROOF   By subtracting (5.8) and (5.13) we see that the error e^n fulfills the recurrence relation

$$e^{n+1} = 2e^n - e^{n-1} + \delta t^2 L_{\delta x} e^n + \delta t^2 \tau^n. \tag{5.35}$$

Similar to the proof of Lemma 5.1, we rewrite the two-step recurrence relation as a one-step recurrence relation in vectorial form

$$\begin{pmatrix} e^{n+1} \\ e^n \end{pmatrix} = \underbrace{\begin{pmatrix} 2I + \delta t^2 L_{\delta x} & -I \\ I & 0 \end{pmatrix}}_{=:A} \begin{pmatrix} e^n \\ e^{n-1} \end{pmatrix} + \delta t^2 \begin{pmatrix} \tau^n \\ 0 \end{pmatrix} \tag{5.36}$$

for all $n = 0, 1, 2, \ldots, N-1$, where A again denotes the block matrix as in (5.19). Recall that $e^{-1} = e^0 = 0$ by definition of the initial values. Therefore we obtain the error description in closed form

$$\begin{pmatrix} e^{n+1} \\ e^n \end{pmatrix} = \delta t^2 \sum_{j=0}^{n} A^{n-j} \begin{pmatrix} \tau^j \\ 0 \end{pmatrix} \tag{5.37}$$

by simple induction. Each term of the sum has the form (5.20). Thus the argumentation in the proof of Lemma 5.1 can be carried out here as well, and we can estimate

$$\begin{aligned} \|e^n\| &\leq \sum_{j=0}^{n-1} \frac{2\delta t}{\sqrt{C_3(4-C_4)}} \|P\| \|P^{-1}\| \|\tau^j\| \\ &\leq n \frac{2\delta t}{\sqrt{C_3(4-C_4)}} \|P\| \|P^{-1}\| \max_j \|\tau^j\| \\ &\leq \frac{2T}{\sqrt{C_3(4-C_4)}} \|P\| \|P^{-1}\| \max_j \|\tau^j\|. \end{aligned} \tag{5.38}$$

The assumption of consistency (5.14) allows to estimate the truncation error $\max_j \|\tau^j\|$, such that the desired estimate (5.34) is finally obtained.   □

Note that Lemma 5.2 does not necessarily imply convergence, since the matrices P and P^{-1} depend on δx. However, if their norms are bounded uniformly for all δx, then the scheme is convergent with the order of consistency. This is quite often the case, as we will see in the following lemma.

Lemma 5.3 *(Second convergence estimate) Assume that the scheme is consistent with order α in time and order β in space and that it is stable. Additionally assume that the matrix $L_{\delta x}$ is symmetric. Then the scheme is convergent with this order, and the error e^n fulfills*

$$\|e^n\| \leq \frac{2C_2 T}{\sqrt{C_3(4-C_4)}} (\delta t^\alpha + \delta x^\beta), \tag{5.39}$$

where C_3 and C_4 are the constants from Definition 5.3.

PROOF   The additional assumption of symmetry implies that there is an orthogonal matrix P such that $P^{-1} L_{\delta x} P$ is diagonal. Since the norm $\|\cdot\|$ we have chosen is a multiple of the Euclidean norm, we conclude $\|P\| = \|P^{-1}\| = 1$. We substitute this into the estimate (5.34) from Lemma 5.2 and obtain the assertion (5.39).   □
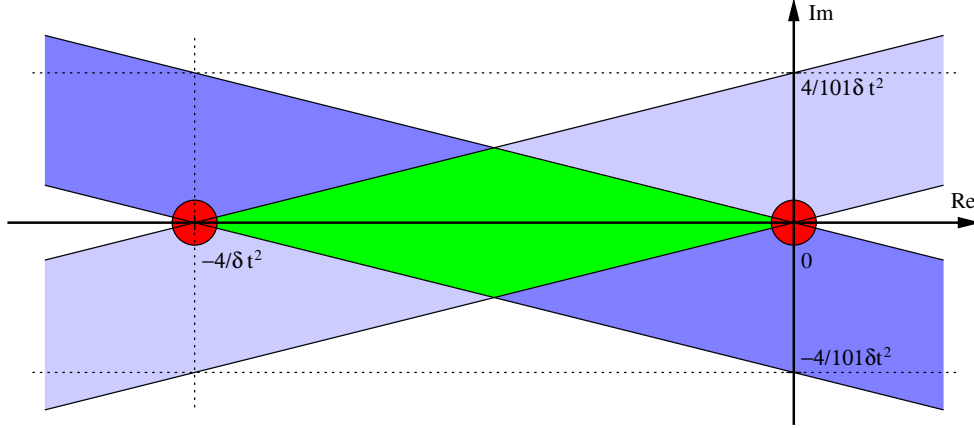
Figure 5.1: Eigenvalues of $L_{\delta x}$ for the stability estimate: Each eigenvalue λ must lie both in the dark blue stripe (5.40) and the mirrored light blue stripe. The intersection forms the green rhombus. The red circles with radius C_3 around 0 and with radius $\frac{4-C_4}{\delta t^2}$ around $\frac{-4}{\delta t^2}$ are forbidden for λ in order to achieve the lower estimate for $\Lambda_1 - \Lambda_2$ as in (5.24).

Let us remark that other norms can be used instead of the discrete L_2-norm $\| \cdot \|$, too. However, one has to ensure that the corresponding operator norms $\|P\|$, $\|P^{-1}\|$ and $\|\Lambda_{1,2}^n\|$ in the proofs are uniformly bounded to obtain convergence similar to Lemma 5.3. Whether this holds or not depends on the respective norm and on the respective operator $L_{\delta x}$.

Then, the prerequisites for the stability in Definition 5.3 can be relaxed. The requirement (5.15) ensures that the matrices Λ_1 and Λ_2 as defined by (5.23) fulfill the estimate $\|\Lambda_{1,2}\| = 1$. Actually, this does not only hold for the part of the real axis given by (5.15). It can be shown that $\|\Lambda_{1,2}\| = 1$ if and only if all eigenvalues λ of $L_{\delta x}$ lie in the stripe

$$\operatorname{Im} \lambda \leq -\frac{1}{101} \operatorname{Re} \lambda, \qquad \operatorname{Im} \lambda \geq -\frac{4}{101\,\delta t^2} - \frac{1}{101} \operatorname{Re} \lambda. \tag{5.40}$$

This region is depicted in dark blue in Figure 5.1. If λ is an eigenvalue of $L_{\delta x}$, then its conjugate $\overline{\lambda}$ is an eigenvalue as well, since the matrix $L_{\delta x}$ is real. Therefore we essentially have the requirement that λ also lies in the same stripe which is mirrored at the real axis, see the light blue region in the figure. The intersection of both stripes forms a rhombus, shown in green. Thus we have $\|\Lambda_{1,2}\| = 1$ if and only if all eigenvalues lie in this rhombus. Furthermore, it must be ensured that the lower estimate for $\Lambda_1 - \Lambda_2$ in (5.24) is not violated. This imposes the restrictions $|\lambda| \geq C_3$ and $|4 + \delta t^2 \lambda| \geq 4 - C_4$, see the red circles in the figure.

Moreover, the requirements for the eigenvalues λ can be relaxed even further. Instead of the equality $\|\Lambda_{1,2}\| = 1$, the estimate

$$\|\Lambda_{1,2}\| \leq 1 + C_5 \delta t \tag{5.41}$$

for some constant C_5 is sufficient in the proof of Lemma 5.2. This additionally allows the eigenvalues λ to lie in a neighborhood of the rhombus given above.[3] Then the terms $\Lambda_{1,2}^n$

---

[3]The thickness of the environment can be arbitrary large, but it must not depend on δt or δx.

are estimated by

$$\|\Lambda_{1,2}{}^n\| \leq \|\Lambda_{1,2}\|^n \leq (1 + C_5\delta t)^n \leq \left(e^{C_5\delta t}\right)^n = e^{C_5 n\delta t} = e^{C_5 T}. \tag{5.42}$$

This resembles a widely used exponential growth estimate.

5.3 Spatial Difference Stencils

After the theoretical convergence analysis, we now come to the actual construction of the spatial operator $L_{\delta x}$.

The most obvious way to discretize the evolution equation (5.1) is to first eliminate the divergence operators by differentiating the terms $\Phi_{,k}^{(J),x}(y, \ldots, \nabla^K y)$ and then to replace the differential operators in the resulting expressions in terms of $y, \nabla y, \ldots, \nabla^{2K}y$ by suitable difference stencils. However, this is a lengthy process since the chain rule and the product rule lead to very many terms with partial derivatives of $\Phi^{(J),x}$ up to order $K+1$ in general.

A better way is to exploit the divergence structure of the evolution equation (5.1) by a two-stage scheme. In the first step, the derivatives $y, \ldots, \nabla^K y$ are computed by applying a suitable difference stencil such that the terms $\Phi_{,k}^{(J),x}$ can be evaluated. In the second step, the divergence operators are applied, as well by means of difference stencils. This is computationally less costly, because the number of involved terms is much smaller. Furthermore, this method is easier to implement, since only $K+1$ terms of the form $\Phi_{,k}^{(J),x}$ have to be coded.

Here we can restrict ourselves to the univariate case $d = 1$, which is necessary for the model problems described in Examples 1, 2 and 3. The generalization for $d > 1$ as required for the simulations with the Stillinger-Weber potential in Section 3.5.2 is then achieved by a tensor product ansatz in a straightforward manner. The evolution equation (5.1) for $d = 1$ reads as

$$\rho\frac{\partial^2 y}{\partial t^2} = \sum_{k=0}^{K}(-1)^{k+1}\frac{\partial^k}{\partial x^k}\Phi_{,k}^{(J),x}\left(y, \frac{\partial}{\partial x}y, \frac{\partial^2}{\partial x^2}y, \ldots, \frac{\partial^K}{\partial x^K}y\right). \tag{5.43}$$

Thus we need difference stencils for the derivatives id, $\frac{\partial}{\partial x}, \frac{\partial^2}{\partial x^2}, \ldots, \frac{\partial^K}{\partial x^K}$ to implement the two-stage scheme.

Such difference stencils can be constructed in a well-known manner. The stencil

$$\begin{bmatrix} s_{W_L} & s_{W_L-1} & \cdots & s_{-1} & s_0 & s_1 & \cdots & s_{W_R-1} & s_{W_R} \end{bmatrix} \tag{5.44}$$

of width $W = W_L + 1 + W_R$ which has W_L points to the left and W_R points to the right must fulfill the conditions of consistency. To this end, we set up the system of linear

equations

$$
\begin{pmatrix}
1 & 1 & \cdots & 1 & 1 \\
-W_L & -W_L+1 & \cdots & W_R-1 & W_R \\
(-W_L)^2 & (-W_L+1)^2 & \cdots & (W_R-1)^2 & W_R{}^2 \\
(-W_L)^3 & (-W_L+1)^3 & \cdots & (W_R-1)^3 & W_R{}^3 \\
\vdots & \vdots & \ddots & \vdots & \vdots \\
(-W_L)^{W-1} & (-W_L+1)^{W-1} & \cdots & (W_R-1)^{W-1} & W_R{}^{W-1}
\end{pmatrix}
\cdot
\begin{pmatrix}
s_{W_L} \\
s_{W_L-1} \\
\vdots \\
s_{W_R-1} \\
s_{W_R}
\end{pmatrix}
=
\begin{pmatrix}
r_0 \\
r_1 \\
\vdots \\
r_{W-2} \\
r_{W-1}
\end{pmatrix}.
\tag{5.45}
$$

Here the right-hand side is given by $r_k = \delta x^k k!$ and $r_l = 0$ for $l \neq k$, where k denotes the respective derivative $\frac{\partial^k}{\partial x^k}$ to be discretized. The matrix of the system is regular, such that there is exactly one stencil which fulfills (5.45).

If this stencil is now applied to a smooth function y with center point $x \in \Omega$, it is easy to check that the result equals

$$
y^{(k)}(x) + c \delta x^{W-k} y^{(W)}(\xi)
\tag{5.46}
$$

for some point $\xi \in \Omega$ and a constant c independent of y. Thus the stencil is pointwise consistent with an order of $W - k$.

For each derivative $k = 0, \ldots, K$, the according stencil must be applied to each point of the vector y^n. This can be subsumed to the matrix

$$
L_{\delta x,k} :=
\begin{pmatrix}
s_0 & s_1 & \cdots & s_{W_R} & & & & & \\
s_{-1} & s_0 & s_1 & \cdots & s_{W_R} & & & & \\
\vdots & \ddots & \ddots & \ddots & & \ddots & & & \\
s_{W_L} & \cdots & s_{-1} & s_0 & s_1 & \cdots & s_{W_R} & & \\
& \ddots & & \ddots & \ddots & \ddots & & \ddots & \\
& & s_{W_L} & \cdots & s_{-1} & s_0 & s_1 & \cdots & s_{W_R} \\
& & & \ddots & & \ddots & \ddots & \ddots & \vdots \\
& & & & s_{W_L} & \cdots & s_{-1} & s_0 & s_1 \\
& & & & & s_{W_L} & \cdots & s_{-1} & s_0
\end{pmatrix}.
\tag{5.47}
$$

Thus the expression $L_{\delta x,k} y^n$ describes the vector of the discrete derivatives of y^n at all grid points. The missing stencil entries at the boundary correspond to accesses to the constant function z which prescribes the boundary values. They are merged to the constant $C_{\delta x}$ and thus do not appear in $L_{\delta x,k}$.

The matrices $L_{\delta x,k}$ are then used to assemble the full spatial operator $L_{\delta x}$.[4] For the arguments of $\Phi^{(J),x}$, the derivative $\frac{\partial^k}{\partial x^k}$ is replaced by $L_{\delta x,k}$. The divergence operators $\frac{\partial^k}{\partial x^k}$ could be discretized by $L_{\delta x,k}$ as well, but here we use $(-1)^k L_{\delta x,k}^T$ instead. Note that not only $L_{\delta x,k}$ is a difference approximation to $\frac{\partial^k}{\partial x^k}$, but that $(-1)^k L_{\delta x,k}^T$ is so as well. Altogether, $L_{\delta x}$ is defined by

$$
L_{\delta x} y^n := -\sum_{k=0}^K L_{\delta x,k}^T \Phi_{,k}^{(J),x} \left(L_{\delta x,0} y^n, \ldots, L_{\delta x,K} y^n \right),
\tag{5.48}
$$

---

[4]The operator $L_{\delta x}$ is of course not assembled explicitly within the numerical implementation. Instead the equivalent two-stage scheme is employed. The full operator $L_{\delta x}$ is only helpful for the convergence analysis.

compare to the right hand side of (5.43).

In the important case of a quadratic potential $\Phi^{(J),x}$ as in Examples 1 and 3, $\Phi^{(J),x}$ can be written as

$$\Phi^{(J),x}(d_0,\ldots,d_K) = \sum_{k,l=0}^{K} a_{kl}d_k d_l. \tag{5.49}$$

for some constants $a_{kl} \in \mathbb{R}$. Then $L_{\delta x}$ is linear, and we have

$$L_{\delta x} = -\sum_{k,l=0}^{K} (a_{kl} + a_{lk})L_{\delta x,k}^T L_{\delta x,l}. \tag{5.50}$$

Because

$$L_{\delta x}^T = -\sum_{k,l=0}^{K} (a_{kl} + a_{lk})\left(L_{\delta x,k}^T L_{\delta x,l}\right)^T = -\sum_{k,l=0}^{K} (a_{kl} + a_{lk})L_{\delta x,l}^T L_{\delta x,k} = L_{\delta x}, \tag{5.51}$$

the matrix $L_{\delta x}$ is symmetric. Note that the symmetry does not hold if the divergence operators would have been discretized by $L_{\delta x,k}$ instead of $(-1)^k L_{\delta x,k}^T$.

The difference stencil matrices $(-1)^k L_{\delta x,k}^T$ and $L_{\delta x,l}$ are by construction pointwise consistent of order $W - k$ and $W - l$, respectively. The product of these two matrices is then pointwise consistent of order $\min(W - k, W - l)$. Since the lowest consistency order which occurs in (5.50) is $W - K$, the overall spatial operator $L_{\delta x}$ is pointwise consistent of order $W - K$.

The pointwise consistency can then be used to assure that the consistency condition as given by Definition 5.2 is fulfilled. The truncation error as defined by (5.13) equals

$$\tau_m^n = \frac{\partial^2 y}{\partial t^2}(n\delta t, m\delta x) + \frac{1}{12}\delta t^2 \frac{\partial^4 y}{\partial t^4}(\xi_1) - Ly(n\delta t, m\delta x) - \delta x^{W-K}R, \tag{5.52}$$

where the remainder term R consists of the derivatives of y up to order $2W$. Since y is assumed to be smooth, R is uniformly bounded. As y is a solution of the evolution equation $\partial_t^2 y - Ly = 0$, we have

$$|\tau_m^n| \le c(\delta t^2 + \delta x^{W-K}). \tag{5.53}$$

This immediately implies that the discrete L_2-norm $\|\tau^n\|$ of the truncation error fulfills (5.14) with $\alpha = 2$ and $\beta = W - K$.

Together with the symmetry of $L_{\delta x}$ stated above, Lemma 5.3 is applicable if the time step size δt is chosen small enough. Therefore the scheme is convergent with order two in time and order $W - K$ in space.

The above construction works nicely in the interior, but cannot be carried out at the boundary. The generalized Dirichlet boundary conditions (5.3) up to order K are usually incorporated by a layer of K ghost points around the domain Ω. The values of these ghost points are kept fix to the prescribed deformation z at the boundary. The difference stencils then access these ghost points, such that the correct boundary values are achieved. But this method does not directly work here, because the difference stencils constructed above are too wide and would excess these ghost points.

A seemingly obvious way out is to use nonsymmetric stencils at the boundary. Such stencils can be constructed with an arbitrary order of consistency, but the lacking symmetry leads to an unstable scheme. This instability is not only of theoretical nature, but has been confirmed by numerical experiments. Hence this approach is not applicable.

Another approach is to set up a system of linear equations similar to (5.45), but which includes as unknowns the entries of all stencils instead of only one, including those at the boundary. In addition to the consistency conditions, the conditions for symmetry of the operator $L_{\delta x}$, which are also linear, are added to the matrix. A careful analysis of the resulting linear system however reveals that no difference stencils not even for the second derivative $\frac{\partial^2}{\partial x^2}$ with Dirichlet boundary conditions exist which lead to a symmetric operator and which are consistent of more than order two. The reason is that the consistency conditions for the fourth derivative and the symmetry conditions are linearly dependent and cannot be fulfilled all at the same time. We conclude that it is impossible to construct such a symmetric difference scheme with a convergence order of more than two.

This negative result unfortunately forces us to use a scheme with a low consistency order at the boundary. We proceed as follows. In addition to the ghost points mentioned above which are necessary for the boundary conditions, we place as many extra ghost points outside of Ω as needed by the wide stencils. Then the symmetric operator $L_{\delta x}$ can be applied everywhere including at the boundary. As a consequence, we obtain a stable scheme.

However, the extra ghost points impose additional boundary conditions. To be precise, more derivatives of the solution are prescribed on the boundary than given by (5.3). This works like an extrapolation of the solution function y by the function z beyond the boundary. Since the derivatives of y and z only coincide up to order $K-1$ due to (5.3), the extrapolation is in general non-smooth. As a consequence, the consistency estimates break down at the boundary. For example, for the second order PDE with common Dirichlet boundary conditions, this leads to a consistency order of only one.

But since we only consider sufficiently short time intervals in our applications such that the evolution of the initial perturbation does not reach the boundary, this low consistency order at the boundary is ineffective and does not destroy the high consistency order of the differential operator in the interior of the domain. Of course, if one is interested in calculating the long-term behavior of solutions which includes boundary interactions, this approach is inappropriate.

In our applications, we use stencils of width $W_L = 4$, $W_R = 3$ and $W = 8$. This is the smallest stencil size which basically eliminates all numerical dissipation. The concrete stencils are given in Table 5.1.

After the construction of the difference scheme, we now check whether the expected convergence rates really hold in practice or not. To this end, we choose the model problem in Example 1. For the polynomial degree of the initial perturbation, we set $\omega = 10$, compare (3.32). The discretized equations are numerically solved as described above for different spatial resolutions.

The convergence behavior of the spatial discretization is depicted in Table 5.2 and Table 5.3. The error was measured both in the discrete L_2-norm and in the maximum norm. Here, the numerical solution with a spatial resolution of 64,000 and 16,000 for (3.31a) and (3.31b), respectively, was used as reference. We used a time step of $\delta t = 0.01$ and $\delta t = 0.001$ for the solution of (3.31a) and (3.31b), respectively. From Table 5.2 we

k	stencil	consistency order
0	$\left[\quad 1 \quad\right]$	∞
1	$\dfrac{1}{\delta x}\left[\ \dfrac{1}{140}\quad \dfrac{-1}{15}\quad \dfrac{3}{10}\quad -1\quad \dfrac{1}{4}\quad \dfrac{3}{5}\quad \dfrac{-1}{10}\quad \dfrac{1}{105}\ \right]$	7
2	$\dfrac{1}{\delta x^2}\left[\ \dfrac{1}{90}\quad \dfrac{-3}{20}\quad \dfrac{3}{2}\quad \dfrac{-49}{18}\quad \dfrac{3}{2}\quad \dfrac{-3}{20}\quad \dfrac{1}{90}\ \right]$	6
3	$\dfrac{1}{\delta x^3}\left[\ \dfrac{-7}{120}\quad \dfrac{8}{15}\quad \dfrac{-89}{40}\quad \dfrac{11}{3}\quad \dfrac{-49}{24}\quad \dfrac{-2}{5}\quad \dfrac{71}{120}\quad \dfrac{-1}{15}\ \right]$	5
4	$\dfrac{1}{\delta x^4}\left[\ \dfrac{-1}{6}\quad 2\quad \dfrac{-13}{2}\quad \dfrac{28}{3}\quad \dfrac{-13}{2}\quad 2\quad \dfrac{-1}{6}\ \right]$	4

$\uparrow$

Table 5.1: Difference stencils with $W_L = 4$ and $W_R = 3$ for the spatial derivatives $\frac{\partial^k}{\partial x^k}$. The arrow $\uparrow$ indicates the center points.

spatial resol.	error in $\|\cdot\|$	ratio	$\log_2(\text{ratio})$	error in $\|\cdot\|_\infty$	ratio	$\log_2(\text{ratio})$
1000	5.067554e-03			4.167261e-02		
2000	5.885063e-04	8.610875	3.106160	5.864973e-03	7.105359	2.828903
4000	3.834007e-06	153.496408	7.262061	3.535252e-05	165.899726	7.374168
8000	1.613063e-08	237.684848	7.892906	1.489190e-07	237.394333	7.891142
16000	6.415617e-11	251.427593	7.973999	5.900347e-10	252.390197	7.979512
32000	2.507196e-13	255.888109	7.999369	2.302158e-12	256.296296	8.001769

Table 5.2: Spatial error and convergence rates for the solution of (3.31a) at $t = 400$ in the discrete L_2-norm and the maximum norm.

spatial resol.	error in $\|\cdot\|$	ratio	$\log_2(\text{ratio})$	error in $\|\cdot\|_\infty$	ratio	$\log_2(\text{ratio})$
500	1.170395e-02			8.962375e-02		
1000	1.334308e-03	8.771550	3.132832	1.081729e-02	8.285232	3.050542
2000	1.585524e-05	84.155672	6.394989	1.328105e-04	81.449043	6.347826
4000	8.626083e-07	18.380573	4.200110	8.599413e-06	15.444137	3.948987
8000	1.642719e-08	52.511005	5.714548	1.646067e-07	52.242194	5.707143

Table 5.3: Spatial error and convergence rates for the solution of (3.31b) at $t = 20$ in the discrete L_2-norm and the maximum norm.

read off that the convergence order is eight. The according stencil from Table 5.1 with $k = 1$ guarantees an order of at least seven, and the symmetry of the composed stencil in $L_{\delta x}$ increases the order by one here. Thus the expected convergence order is fully reached for model (3.31a). For model (3.31b) we roughly obtain the order six, which is again one more than the guaranteed order five. Note that the convergence rates are not only achieved for the discrete L_2-norm, but for the maximum norm as well.

Chapter 6

Conclusions

We proposed the inner expansion technique to derive quasi-continuum models from atomistic systems for crystalline solids. This approach is capable of capturing the material properties to a high extent. In contrast to the classical thermodynamic limit, the microscopic properties and the discreteness effects of the underlying atomistic model are correctly reproduced. We showed this numerically for the simple model problem of an atomic chain.

The analysis of the inner expansion technique revealed that important properties of the atomistic potential such as convexity, frame indifference and lattice symmetry are carried over to the continuum level. Therefore hyperbolicity and well-posedness of the resulting macroscopic evolution equations are guaranteed. We compared our upscaling technique to the scaling technique which employs the thermodynamic limit and the direct expansion technique which deduces higher order contributions as well.

We then applied our new technique to the model of a silicon crystal and showed that the higher approximation quality holds for more complex potentials as well. Nonlinear deformations such as bending are now very precisely reproduced by the potential energy, in contrast to the classical continuum limit. Furthermore, we performed a numerical simulation of the elastic response of a silicon crystal to show that the newly obtained model also works for dynamical problems.

The continuum mechanical potential obtained by the inner expansion technique provides a precise description of the material behavior on the atomic level, paying price of a rather complex expression in which the different terms are coupled in a highly nonlinear manner. Therefore we developed approximation techniques which simplify the potential but retain the important characteristics. First, a simplified principal part has been deduced from the full continuum potential which resembles the dependence on the most decisive argument ∇y. This way the positions of the wells and the martensitic elastic moduli are strictly derived from the atomistic model and thus need not to be taken from measurements, as it is done in most of the conventional models. The resulting potential has been employed to simulate the operation of SMA micro-actuators. In a second step, the higher order contributions have been further simplified and an improved continuum model for crystalline silicon has been formulated which correctly determines the length scale.

Classical continuum mechanics deals with systems in the order of 10^{23} atoms for which the continuum limit often is a good description. But the advances in nanotechnology in

the last years necessitate to consider systems with a substantially smaller number of atoms for which the full continuum description clearly fails. On the other hand, these systems are still not in reach of conventional molecular dynamics methods due to complexity reasons and the necessary involved small time step sizes. In this respect the quasi-continuum approach becomes more and more important for practical applications.

The main advantages of a quasi-continuum model compared to an atomistic model are as follows: its numerical solution is much less costly, because the resolution of the discretization can be freely controlled, whereas the atomistic model which is already discrete is restricted to the physically given discreteness. This allows to use quite coarse grids for the discretization of the macroscopic model without loosing its atomic discreteness properties. Furthermore, compared to atomistic models, much larger time step sizes can be used. Moreover, advanced numerical techniques like adaptivity can be employed if necessary and also analytical techniques for PDEs might be applied.

Let us mention that our method is capable of reproducing boundary effects, i.e. the possibly different behavior of the specimen in the vicinity of its boundary. Although not exploited here, this can be important for potentials for which these effects play a substantial role. Such effects are lost with the classical scaling method, since the limiting procedure treats every inner point of the specimen as being surrounded by infinite bulk material, independently of its physical distance to the boundary.

An open point is the incorporation of temperature from first principles. It would be desirable to strictly derive an energy density

$$\Phi^{(I),x}\big(y(x), \nabla y(x), \dots, \nabla^K y(x), \vartheta\big) \qquad (6.1)$$

from the atomistic model which decouples the temperature ϑ from the macroscopic deformation described by the derivatives of y. This would for example allow to directly measure the austenitic Young moduli and the Clausius-Clapeyron slope, whereas we have been forced to fall back to a phenomenological construction in the present work. Furthermore, nearly all physical processes involve a certain dissipation. For our example of martensitic phase transformations, a phenomenological dissipation mechanism has been developed in [67], [62] and [63] and numerically investigated in [7]. A strict treatment of temperature by upscaling would incorporate these dissipative effects automatically into the continuum mechanical model.

Closely connected to the incorporation of temperature is an upscaling in time. Thermal fluctuations take place on a much faster time scale than the macroscopic elastic behavior. Thus, it can be expected that a decoupling of the temperature from the deformation function can only be accomplished together with a suitable time upscaling. However, no related approaches are known to us.

Another interesting point would be to analyze other expansions instead of the Taylor series expansion of the deformation function y. This way, completely different types of continuum models can be deduced which comprise pseudodifferential operators or the like. For example, fractional order terms can be strictly deduced from the atomistic model which have been phenomenologically employed in [7]. Depending on the specific expansion, this might allow to reduce the required smoothness assumptions for the deformation function y. Furthermore, other estimates for the truncation error of the series will apply then, which result in different approximation properties of the resulting continuum model.

Appendix A

Parameters of the EAM Potential

The EAM potential as described in Section 2.3.1 makes use of the electron density ρ_x^{atom}, the embedding function Φ_x^{emb} and the effective charge Z_x. These functions constitute the behavior of the concrete material and are defined in the following sections.

A.1 Electron Density

The electron density is taken from quantum mechanical calculations, which are performed a priori and are taken fixed within the EAM potential. Here, the results of single-determinant Hartree-Fock calculations of Clementi and Roetti [21] are used.[1] In this paper, concrete wave functions are given for the chemical elements He–Xe in the ground state and in various excited states and for neutral and for ionized atoms.

The electron density ρ_x^{orbital} of each orbital is described by the ansatz[2]

$$\rho_x^{\text{orbital}}(r) = \frac{1}{4\pi} \left| \sum_k C_k \frac{(2\zeta_k)^{n_k+1/2}}{\sqrt{(2n_k)!}} r^{n_k-1} e^{-\zeta_k r} \right|^2. \tag{A.1}$$

The constants C_k, ζ_k and n_k have been determined by Clementi and Roetti and are given in Table A.1.[3] The electron density ρ_x^{atom} of the whole atom then is a linear combination of the densities ρ_x^{orbital} of the respective orbitals. Additionally, a cutoff function is applied. This leads to

$$\rho_x^{\text{atom}}(r) = \begin{cases} N_s \rho^{s-\text{orbital}}(r) + (N - N_s)\rho^{p/d-\text{orbital}}(r) - \rho_x^{\text{offset}} & \text{if } r \leq r_x^{\text{cutoff}} \\ 0 & \text{if } r > r_x^{\text{cutoff}}, \end{cases} \tag{A.2}$$

---

[1] These values are already quite old. Newer and more accurate values are given for example in [20]. Nevertheless, it is disadvantageous to use them for two reasons. First, even the old values are much more accurate than the empirically fitted values for the embedding function Φ_x^{emb} and the effective charge Z_x, such that the new values only increase the computational effort without improving accuracy. Second, the embedding function and the effective charge are fitted to the material properties on the basis of the old electron densities, such that the new values would falsify this fit.

[2] Each term of the sum usually contains the normalized spherical harmonics as an additional factor [21, Formula (5)]. Here they disappear, because the density is spherically averaged to obtain a radially symmetric density for the EAM [27, Table V].

[3] The values for ζ_k are originally given in Bohr radii a_B and have been converted to Å. Note that the values slightly differ from those in [27], because we used the more accurate conversion $a_B = 0.529177$ Å instead of $a_B = 0.529$ Å.

Nickel					
	k	n_k	ζ_k [a_B^{-1}]	ζ_k [Å^{-1}]	C_k [1]
4s	1	1	29.03620	54.87049	-0.00389
	2	1	20.35820	38.47144	-0.02991
	3	2	14.50890	27.41786	-0.03189
	4	2	11.04660	20.87506	0.15289
	5	3	5.79629	10.95341	-0.20048
	6	3	3.87206	7.31714	-0.05423
	7	4	2.07712	3.92519	0.49292
	8	4	1.13888	2.15217	0.61875
3d	1	3	6.70551	12.67158	0.42120
	2	3	2.87381	5.43072	0.70658

Aluminum					
	k	n_k	ζ_k [a_B^{-1}]	ζ_k [Å^{-1}]	C_k [1]
3s	1	1	14.22690	26.88496	-0.00452
	2	1	10.72610	20.26940	0.08395
	3	2	5.00360	9.45544	-0.11622
	4	2	3.63124	6.86205	-0.18811
	5	3	1.77396	3.35230	0.54265
	6	3	1.10766	2.09317	0.55020
3p	1	2	7.20781	13.62079	-0.04475
	2	2	3.65413	6.90531	-0.14977
	3	3	1.68275	3.17994	0.26788
	4	3	0.91381	1.72685	0.80384

Table A.1: Parameters for the double-ζ approximation of the electron density.

	N	N_s	r^cutoff [Å]
Nickel	10	0.85	4.64453
Aluminum	3	2	5.34469

Table A.2: Parameters for the linear combination of the electron densities of the respective orbitals.

where N denotes the total number of valence electrons and N_s the number of valence electrons of the s-orbital. The cutoff distance r_x^cutoff is chosen such that the electron density is cut off between the third and fourth shell in the ground state, see [56, p. 56]. The offset ρ_x^offset is determined such that ρ_x^atom is continuous. The parameters N, N_s and r_x^cutoff have been taken from [56] and [49] and are given in Table A.2.

Nickel							
$\rho[\rho_0]$	$\rho[\text{Å}^{-3}]$	$\Phi_x^{\text{emb}}[\text{J}]$	$\Phi_x^{\text{emb}''}$	$r[a_0]$	$r[\text{Å}]$	$Z_x[\text{C}]$	Z_x'
0.0	0.0	0	0.0	0.0	0.0	44.86132e-19	0.0
0.5	0.01412	-5.87470e-19		0.6	2.112	1.58200e-19	
1.0	0.02824	-8.63439e-19		0.71	2.4992	0.25571e-19	
2.0	0.05648	-5.78532e-19		0.85	2.992	0	0.0
2.3	0.06495	0	0.0				

Aluminum							
$\rho[\rho_0]$	$\rho[\text{Å}^{-3}]$	$\Phi_x^{\text{emb}}[\text{J}]$	$\Phi_x^{\text{emb}''}$	$r[a_0]$	$r[\text{Å}]$	$Z_x[\text{C}]$	Z_x'
0.0	0.0	0	0.0	0.0	0.0	20.82847e-19	0.0
0.25	0.007312	-3.77114050e-19		0.43	1.7415	3.61182e-19	
0.5	0.014625	-4.95479905e-19		0.65	2.6325	0.30746e-19	
1.5	0.043875	-6.47851420e-19		0.71	2.8755	0.13795e-19	
2.0	0.0585	-7.21094380e-19		0.85	3.4425	-0.12081e-19	
2.5	0.073125	-5.71774655e-19		1.1	4.4550	0	0.0
2.8	0.0819	0	0.0				

Table A.3: Knots and function values of the embedding function $\Phi_x^{\text{emb}}(\rho)$ and the effective charge $Z_x(r)$.

	Nickel	Aluminum
equilibrium electron density ρ_0 [Å^{-3}]	0.02824	0.02925
lattice constant a_0 [Å]	3.52	4.05
lattice structure	fcc	fcc
atomic mass [u]	58.6934	26.981538
atomic mass [kg]	9.74626639e-26	4.480388884e-26

Table A.4: Remaining parameters of nickel and aluminum.

A.2   Embedding Function and Effective Charge

The embedding function Φ_x^{emb} and the effective charge function Z_x are determined semi-empirically such that the potential resembles certain physical properties. Here we employ the functions which have been constructed by Meyer [56] and Kadau [49]. The functions Φ_x^{emb} and Z_x are represented by a cubic spline with manually chosen knots. A weighted least-square method has been used to fit the coefficients to the lattice constant, the binding energy, the elastic moduli, the vacancy formation energy and the phonon frequencies.

The knots and the according function values of $\Phi_x^{\text{emb}}(\rho)$ and $Z_x(r)$ are given in Table A.3. Outside the given interval, the function Φ_x^{emb} is continued by an affine linear function, indicated in the table by $\Phi_x^{\text{emb}''} = 0$, and the function Z_x is continued by a constant function, indicated by $Z_x' = 0$.

Bibliography

[1] G. C. Abell. Empirical chemical pseudopotential theory of molecular and metallic bonding. *Phys. Rev. B*, 31(10):6184–6196, 1985.

[2] M. P. Allen and D. J. Tildesley. *Computer Simulation of Liquids*. Oxford University Press, 1987.

[3] H. C. Andersen. Molecular dynamics simulations at constant pressure and/or temperature. *J. Chem. Phys.*, 72:2384–2393, 1980.

[4] M. Arndt. Upscaling technique for the atomistic-continuum simulation of shape memory alloys with the EAM potential. In Z. Yao, M. Yuan, and W. Zhong, editors, *Proceedings of the Sixth World Congress on Computational Mechanics (WCCM 6), Beijing*, volume 1, page 193. Tsinghua University Press and Springer, 2004.

[5] M. Arndt and M. Griebel. Higher order gradient continuum description of atomistic models for crystalline solids. In P. Neittaanmäki, T. Rossi, S. Korotov, E. Oñate, J. Périaux, and D. Knörzer, editors, *Proceedings of the Fourth European Congress on Computational Methods in Applied Sciences and Engineering (ECCOMAS 2004)*. University of Jyväskylä, Department of Mathematical Information Technology, 2004.

[6] M. Arndt and M. Griebel. Derivation of higher order gradient continuum models from atomistic models for crystalline solids. *Multiscale Model. Simul.*, 2005. Accepted.

[7] M. Arndt, M. Griebel, and T. Roubíček. Modelling and numerical simulation of martensitic transformation in shape memory alloys. *Contin. Mech. Thermodyn.*, 15(5):463–485, 2003.

[8] S. Aubry, M. Fago, and M. Ortiz. A constrained sequential-lamination algorithm for the simulation of sub-grid microstructure in martensitic materials. *Comput. Methods Appl. Mech. Eng.*, 192(26-27):2823–2843, 2003.

[9] J. M. Ball and R. D. James. Fine phase mixtures as minimizers of energy. *Arch. Ration. Mech. Anal.*, 100:13–52, 1987.

[10] J. M. Ball and R. D. James. Proposed experimental tests of a theory of fine microstructure and the two-well problem. *Philos. Trans. R. Soc. Lond. Ser. A*, 338:389–450, 1992.

[11] S. Bardenhagen and N. Triantafyllidis. Derivation of higher order gradient continuum theories in 2,3-D nonlinear elasticity from periodic lattice models. *J. Mech. Phys. Solids*, 42(1):111–139, 1994.

[12] M. I. Baskes. Application of the embedded-atom method to covalent materials: A semiempirical potential for silicon. *Phys. Rev. Lett.*, 59(23):2666–2669, 1987.

[13] M. I. Baskes. Modified embedded-atom potentials for cubic materials and impurities. *Phys. Rev. B*, 46(5):2727–2742, 1992.

[14] M. I. Baskes, J. S. Nelson, and A. F. Wright. Semiempirical modified embedded-atom potentials for silicon and germanium. *Phys. Rev. B*, 40(9):6085–6100, 1989.

[15] H. J. C. Berendsen, J. P. M. Postma, W. F. van Gunsteren, A. DiNola, and J. R. Haak. Molecular dynamics with coupling to an external bath. *J. Chem. Phys.*, 81(8):3684–3690, 1984.

[16] K. Bhattacharya. Theory of martensitic microstructure and the shape-memory effect, 2001. Draft monograph.

[17] X. Blanc, C. Le Bris, and P.-L. Lions. From molecular models to continuum mechanics. *Arch. Ration. Mech. Anal.*, 164(4):341–381, 2002.

[18] A. Braides and M. S. Gelli. From discrete to continuum: A variational approach. Lecture notes, SISSA, Trieste, 2000.

[19] D. W. Brenner. Empirical potential for hydrocarbons for use in simulating the chemical vapor deposition of diamond films. *Phys. Rev. B*, 42(15):9458–9471, 1990.

[20] C. F. Bunge, J. A. Barrientos, A. V. Bunge, and J. A. Cogordan. Hartree-Fock and Roothaan-Hartree-Fock energies for the ground states of He through Xe. *Phys. Rev. A*, 46(7):3691–3696, 1992.

[21] E. Clementi and C. Roetti. Roothaan–Hartree–Fock atomic wavefunctions. *Atomic Data and Nuclear Data Tables*, 14:177–478, 1974.

[22] M. A. Collins. A quasicontinuum approximation for solitons in an atomic chain. *Chem. Phys. Lett.*, 77(2):342–347, 1981.

[23] R. Courant, K. O. Friedrichs, and H. Lewy. Über die partiellen Differenzengleichungen der mathematischen Physik. *Math. Ann.*, 100:32–74, 1928.

[24] B. Dacorogna. *Direct Methods in the Calculus of Variations*, volume 78 of *Applied Mathematical Sciences*. Springer, Berlin, 1989.

[25] C. M. Dafermos. *Hyperbolic Conservation Laws in Continuum Physics*, volume 325 of *Grundlehren der mathematischen Wissenschaften*. Springer, Berlin, 2000.

[26] M. S. Daw and M. I. Baskes. Semiempirical, quantum mechanical calculation of hydrogen embrittlement in metals. *Phys. Rev. Lett.*, 50(17):1285–1288, 1983.

[27] M. S. Daw and M. I. Baskes. Embedded-atom method: Derivation and application to impurities, surfaces, and other defects in metals. *Phys. Rev. B*, 29(12):6443–6453, 1984.

[28] W. Dreyer and R. Guckel.   Micro-macro transitions by interpolation, smooth-
     ing/averaging and scaling of particle trajectories. Preprint No. 725, WIAS Berlin,
     2002.

[29] W. E and B. Engquist. The heterogeneous multi-scale methods. *Comm. Math. Sci.*,
     1(1):87–133, 2003.

[30] W. E, B. Engquist, and Z. Huang. Heterogeneous multiscale method: A general
     methodology for multiscale modeling. *Phys. Rev. B*, 67(9):092101, 2003.

[31] W. E and Z. Huang. A dynamic atomistic-continuum method for the simulation of
     crystalline materials. *J. Comput. Phys.*, 182(1):234–261, 2002.

[32] J. L. Ericksen. On the symmetry of deformable crystals. *Arch. Ration. Mech. Anal.*,
     72:1–13, 1979.

[33] J. L. Ericksen. The Cauchy and Born hypotheses for crystals. In M. E. Gurtin et al.,
     editors, *Phase Transformations and Material Instabilities in Solids*. Academic Press,
     New York, 1984.

[34] J. L. Ericksen. Constitutive theory for some constrained elastic crystals. *Int. J. Solids
     Struct.*, 22(9):951–964, 1986.

[35] J. L. Ericksen. Some constrained elastic crystals. In J. Ball, editor, *Material Insta-
     bilities in Continuum Mechanics and Related Mathematical Problems*, pages 119–137.
     Oxford University Press, 1987.

[36] E. Fermi, J. Pasta, and S. Ulam. Studies of nonlinear problems I. Report LA-1940,
     Los Alamos Scientific Laboratory, 1955. Reprinted in: Nonlinear Wave Motion, A.
     C. Newell (ed.), AMS Lect. Appl. Math. 15:143–156, 1974.

[37] D. Frenkel and B. Smit. *Understanding Molecular Simulation. From Algorithms to
     Applications*. Academic Press, San Diego, 2002.

[38] G. Friesecke and R. D. James. A scheme for the passage from atomic to continuum
     theory for thin films, nanotubes and nanorods. *J. Mech. Phys. Solids*, 48(6–7):1519–
     1540, 2000.

[39] G. Friesecke and K. Matthies. Geometric solitary waves in a 2D mass-spring lattice.
     Discrete Contin. Dyn. Syst., 3(1):105–114, 2003.

[40] G. Friesecke and R. L. Pego. Solitary waves on FPU lattices: I. Qualitative properties,
     renormalization and continuum limit. *Nonlinearity*, 12(6):1601–1627, 1999.

[41] G. Friesecke and F. Theil. Validity and failure of the Cauchy-Born hypothesis in a
     two-dimensional mass-spring lattice. *J. Nonlinear Sci.*, 12(5):445–478, 2002.

[42] M. Griebel, S. Knapek, G. Zumbusch, and A. Caglar. *Numerische Simulation in der
     Moleküldynamik*. Springer, Berlin, 2003.

[43] R. Haberlandt, S. Fritzsche, G. Peinel, and K. Heinzinger. *Molekulardynamik*. Vieweg,
     Braunschweig/Wiesbaden, 1995.

[44] P. R. Halmos. *Finite-Dimensional Vector Spaces*. D. Van Nostrand Company, Princeton, 2nd edition, 1958.

[45] R. W. Hockney and J. W. Eastwood. *Computer Simulation Using Particles*. Institute of Physics Publishing, Bristol and Philadelphia, 1988.

[46] P. Hohenberg and W. Kohn. Inhomogeneous electron gas. *Phys. Rev. B*, 136(3):864–871, 1964.

[47] W. G. Hoover. Canonical dynamics: Equilibrium phase-space distributions. *Phys. Rev. A*, 31(3):1695–1697, 1985.

[48] W. G. Hoover. Constant-pressure equations of motion. *Phys. Rev. A*, 34(3):2499–2500, 1986.

[49] K. Kadau. *Molekulardynamik-Simulationen von strukturellen Phasenumwandlungen in Festkörpern, Nanopartikeln und ultradünnen Filmen*. PhD thesis, Gerhard-Mercator-Universität Duisburg, 2001.

[50] O. Kastner. Molecular-dynamics of a 2D model of the shape memory effect. Part I: Model and simulations. *Contin. Mech. Thermodyn.*, 15(5):487–502, 2003.

[51] P. G. Kevrekidis, I. G. Kevrekidis, A. R. Bishop, and E. S. Titi. Continuum approach to discreteness. *Phys. Rev. E*, 65(4):046613, 2002.

[52] J. Knap and M. Ortiz. An analysis of the quasicontinuum method. *J. Mech. Phys. Solids*, 49(9):1899–1923, 2001.

[53] M. D. Kruskal and N. J. Zabusky. Stroboscopic perturbation procedure for treating a class of nonlinear wave equations. *J. Math. Phys.*, 5(2):231–244, 1964.

[54] R. J. LeVeque. *Numerical Methods for Conservation Laws*. Birkhäuser, Basel, 1990.

[55] W. K. Liu, E. G. Karpov, S. Zhang, and H. S. Park. An introduction to computational nanomechanics and materials. *Comput. Methods Appl. Mech. Eng.*, 193(17-20):1529–1578, 2004.

[56] R. Meyer. *Computersimulationen martensitischer Phasenübergänge in Eisen-Nickel- und Nickel-Aluminium-Legierungen*. PhD thesis, Gerhard-Mercator-Universität Duisburg, 1998.

[57] S. Nosé. A molecular dynamics method for simulation in the canonical ensemble. *Mol. Phys.*, 52:255–268, 1984.

[58] S. Nosé. A unified formulation of the constant temperature molecular dynamics methods. *J. Chem. Phys.*, 81(1):511–519, 1984.

[59] M. Parrinello and A. Rahman. Crystal structure and pair potentials: A molecular-dynamics study. *Phys. Rev. Lett.*, 45(14):1196–1199, 1980.

[60] M. Parrinello and A. Rahman. Polymorphic transitions in single crystals: A new molecular dynamics method. *J. Appl. Phys.*, 52(12):7182–7190, 1981.

[61] M. Pitteri and G. Zanzotto. *Continuum Models for Phase Transitions and Twinning in Crystals.* Chapman & Hall/CRC Press, Boca Raton, 2002.

[62] P. Plecháč and T. Roubíček. Visco-elasto-plastic model for martensitic phase transformation in shape-memory alloys. *Math. Methods Appl. Sci.*, 25(15):1281–1298, 2002.

[63] K. R. Rajagopal and T. Roubíček. On the effect of dissipation in shape-memory alloys. *Nonlinear Anal. Real World Appl.*, 4(4):581–597, 2003.

[64] P. Rosenau. Dynamics of nonlinear mass-spring chains near the continuum limit. *Phys. Lett. A*, 118(5):222–227, 1986.

[65] P. Rosenau. Dynamics of dense lattices. *Phys. Rev. B*, 36(11):5868–5876, 1987.

[66] P. Rosenau. Hamiltonian dynamics of dense chains and lattices: Or how to correct the continuum. *Phys. Lett. A*, 311(1):39–52, 2003.

[67] T. Roubíček. Dissipative evolution of microstructure in shape memory alloys. In H.-J. Bungartz, R. H. W. Hoppe, and C. Zenger, editors, *Lectures on Applied Mathematics*, pages 45–63. Springer, Berlin, 2000.

[68] J. Rowlinson. Translation of J. D. van der Waals' "The thermodynamic theory of capillarity under the hypothesis of a continuous variation of density". *J. Stat. Phys.*, 20(2):197–244, 1979. English translation of [79].

[69] S. Rubini and P. Ballone. Quasiharmonic and molecular-dynamics study of the martensitic transformation in Ni–Al alloys. *Phys. Rev. B*, 48(1):99–111, 1993.

[70] F. H. Stillinger and T. A. Weber. Computer simulation of local order in condensed phases of silicon. *Phys. Rev. B*, 31(8):5262–5271, 1985.

[71] F. H. Stillinger and T. A. Weber. Erratum: Computer simulation of local order in condensed phases of silicon. *Phys. Rev. B*, 33(2):1451, 1986.

[72] E. B. Tadmor, M. Ortiz, and R. Phillips. Quasicontinuum analysis of defects in solids. *Philos. Mag. A*, 73(6):1529–1563, 1996.

[73] E. B. Tadmor, R. Phillips, and M. Ortiz. Mixed atomistic and continuum models of deformation in solids. *Langmuir*, 12(19):4529–4534, 1996.

[74] J. Tersoff. New empirical model for the structural properties of silicon. *Phys. Rev. Lett.*, 56(6):632–635, 1986.

[75] B. J. Thijsse. Relationship between the modified embedded-atom method and Stillinger-Weber potentials in calculating the structure of silicon. *Phys. Rev. B*, 65(19):195207, 2002.

[76] J. W. Thomas. *Numerical Partial Differential Equations: Finite Difference Methods*, volume 22 of *Texts in Applied Mathematics*. Springer, New York, 1995.

[77] N. Triantafyllidis and S. Bardenhagen. On higher order gradient continuum theories in 1-D nonlinear elasticity. Derivation from and comparison to the corresponding discrete models. *J. Elasticity*, 33(3):259–293, 1993.

[78] N. Triantafyllidis and S. Bardenhagen. The influence of scale size on the stability of periodic solids and the role of associated higher order gradient continuum models. *J. Mech. Phys. Solids*, 44(11):1891–1928, 1996.

[79] J. D. van der Waals. The thermodynamic theory of capillarity under the hypothesis of a continuous variation of density (translation of Dutch title). *Verhandel. Konink. Akad. Weten. Amsterdam (sect. 1)*, 1(8):1–56, 1893.

[80] L. Verlet. Computer "experiments" on classical fluids. I. Thermodynamical properties of Lennard-Jones molecules. *Phys. Rev.*, 159(1):98–103, 1967.

[81] P. Šittner and V. Novák. Anisotropy of martensitic transformations in modeling of shape memory alloy polycrystals. *Int. J. Plast.*, 16(10-11):1243–1268, 2000.

[82] G. J. Wagner, E. G. Karpov, and W. K. Liu. Molecular dynamics boundary conditions for regular crystal lattices. *Comput. Methods Appl. Mech. Eng.*, 193(17-20):1579–1601, 2004.

[83] G. J. Wagner and W. K. Liu. Coupling of atomistic and continuum simulations using a bridging scale decomposition. *J. Comput. Phys.*, 190(1):249–274, 2003.

[84] J. A. D. Wattis. Approximations to solitary waves on lattices. II. Quasi-continuum methods for fast and slow waves. *J. Phys. A*, 26(5):1193–1209, 1993.

[85] N. J. Zabusky and M. D. Kruskal. Interaction of "solitons" in a collisionless plasma and the recurrence of initial states. *Phys. Rev. Lett.*, 15(6):240–243, 1965.